

**Constraints on Magma Ocean
Crystallization in the Early Earth:
Experiments, Thermodynamics and Ab
initio simulations**

DISSERTATION

zur Erlangung des akademischen Grades eines
Doktors der Naturwissenschaften (Dr. rer. nat.)
in der Bayreuther Graduiertenschule für Mathematik und Naturwissenschaften
(BayNAT)
der Universität Bayreuth

vorgelegt von

Jie Yao

aus *Jiangsu (China)*

Bayreuth, 2021

Die vorliegende Arbeit wurde in der Zeit von November 2016 bis September 2021 in Bayreuth am Bayerischen Geoinstitut unter Betreuung von Herrn Dr. Gerd Steinle-Neumann, Professor Dr. Dan Frost angefertigt.

Vollständiger Abdruck der von der Bayreuther Graduiertenschule für Mathematik und Naturwissenschaften (BayNAT) der Universität Bayreuth genehmigten Dissertation zur Erlangung des akademischen Grades eines Doktors der Naturwissenschaften (Dr. rer. nat.).

Dissertation eingereicht am: 14.10.2021

Zulassung durch das Leitungsgremium: 28.10.2021

Wissenschaftliches Kolloquium: 07.12.2021

Amtierender Direktor: Prof. Dr. Hans Keppler

Prüfungsausschuss:

PD. Dr. Gerd Steinle-Neumann	(Gutachter)
Prof. Dr. Daniel Frost	(Gutachter)
PD. Dr. Catherine McCammon	(Vorsitz)
Prof. Dr. Audrey Bouvier	

Summary

Giant impact events in the early Earth have led to large-scale melting, potentially up to the entire planet becoming liquid. Some highly fractionated residual melt may have persisted at the base of the mantle contributing to the existence of ultra-low velocity zones and large low shear velocity provinces. The crystallization of silicate melt from the magma ocean, or residual reservoirs, therefore provides an important constraint on chemical differentiation and possible initial stratification in the Earth.

Characterizing and modelling melting relations in the system MgO-SiO₂ at lower mantle pressures (P) relies on the location of the eutectic points for MgO-MgSiO₃ and MgSiO₃-SiO₂. While at an uppermost lower mantle pressure ($P \sim 25$ GPa) there is general consensus on the eutectic composition in the MgO-MgSiO₃ system, large discrepancies exist for MgSiO₃-SiO₂ from experiments in the diamond anvil cell and ab-initio simulations, as well as models built on them. In order to address this discrepancy, we have performed multi-anvil press experiments at 24 GPa for Mg_{0.4}Si_{0.6}O_{1.6} and Mg_{0.3}Si_{0.7}O_{1.7} at temperatures (T) of 2650 ± 100 K and 2750 ± 100 K. At 2750 ± 100 K, we observe the presence of partial melt, and the recovered sample from the experiment with Mg_{0.4}Si_{0.6}O_{1.6} starting composition shows SiO₂ stishovite as the liquidus phase, and electron microprobe analysis determines $X_{\text{SiO}_2} = 0.53 \pm 0.03$ as the eutectic composition. Based on the experimental results, we fit a thermodynamic model for the melting relations in the MgO-SiO₂ system and extrapolate to core-mantle boundary pressure. At 136 GPa, we predict that the eutectic points have moved further away from MgSiO₃, and solidus temperatures are similar for MgO-MgSiO₃ and MgSiO₃-SiO₂.

We have further extended the melting experiments in the multi-anvil press at 24 GPa to compositions along the MgSiO₃-FeSiO₃ join, with starting compositions Mg_{0.9}Fe_{0.1}SiO₃, Mg_{0.8}Fe_{0.2}SiO₃, Mg_{0.7}Fe_{0.3}SiO₃ and Mg_{0.5}Fe_{0.5}SiO₃, heated to 2650 ± 100 , 2615 ± 100 , 2580 ± 100 and 2510 ± 100 K, respectively. Scanning electron microscope images of the recovered samples show coexisting bridgmanite solid with melt. From their chemical analysis by electron microprobe, we determine $K_D = (\text{Fe}^{\text{solid}}/\text{Mg}^{\text{solid}})/(\text{Fe}^{\text{liquid}}/\text{Mg}^{\text{liquid}})$, the iron equilibrium constant. With increasing FeSiO₃ content of the starting composition, it decreases quasi-linearly from $K_D \sim 0.31 \pm 0.07$ to $\sim 0.22 \pm 0.02$. We construct a thermodynamic model for the FeO-MgO-SiO₂ system based on these partitioning data and the melting curve of the

endmembers, and binary melting phase diagrams along the MgO-SiO₂, MgSiO₃-FeSiO₃, MgO-FeO, FeO-SiO₂ systems are calculated at 24 and 136 GPa. At 24 GPa they compare favorably with available experimental phase relations that were not used as constraints. At core mantle boundary conditions, we find that iron partition strongly into the melt. The lower solidus T of FeO-rich melts provides a possible explanation for low velocity features in the lowermost mantle.

Melt density is a key parameter affecting the dynamic process of magma ocean crystallization. We have performed molecular dynamic simulation of liquid Mg₂₈Fe₄Si₁₆O₆₄ and Mg₃₂Si₁₆O₆₄ over a wide compression range (reaching 370 GPa) at 3000 K, based on density functional theory, using the generalized gradient approximation plus local Coulomb repulsion (GGA + U) approach. We find iron in Mg₂₈Fe₄Si₁₆O₆₄ in a high-spin state with an average magnetic moment of $4.0 \pm 0.1 \mu_B$ up to 35 GPa, followed by a quasi-linear decrease with P , reaching $0.5 \pm 0.4 \mu_B$ at 370 GPa. We explore melt structure and fit the isothermal P -volume results using the Tait equation of state. Partial molar volumes of FeO and MgO are virtually identical across the whole P range, which is also reflected in very similar radial distribution functions. Based on the molar weight difference alone, olivine melt with 25%mol of Fe₂SiO₄ shows higher density than seismic models for the Earth mantle above ~ 85 GPa, suggesting that a basal magma ocean in the early earth may have been gravitationally stable given the high iron equilibrium constant predicted from our thermodynamic model.

Experimental measurements of the structure and physical properties of silicate liquids are challenging due to their high melting point. Many experiments therefore rely on silicate glass, quenched from the melt. The extent to which they represent liquid structure, however, cannot be unambiguously evaluated. We have therefore performed molecular dynamics simulations based on density functional theory for Mg₂SiO₄ and MgSiO₃ melt at 2000 K and glass at 300 K, cooled from the melt with different rates: immediate quench and 0.1 K per femtosecond (slow cooling). Analyzing the resulting glass and melt structure by means of total and partial radial distribution functions and structure factors, we find that slowly cooled glass shows more structural features than the quench or melt. Differences in total X-ray and neutron structure factors are too small between them, and too large between different measurements, to understand whether the cooling effects are reflected in experiments.

Zusammenfassung

Riesige Impaktereignisse haben in der frühen Erde zu großflächigem Schmelzen geführt, die möglicherweise den gesamten Planeten verflüssigt haben. Einige stark fraktionierte Restschmelzen könnten bis heute an der Basis des Erdmantels verblieben sein und zur Existenz von Zonen mit extrem niedrigen Geschwindigkeiten und großen Regionen mit niedrigen Schergeschwindigkeiten beitragen. Die Kristallisation von Silikatschmelze aus dem Magmaozean oder aus den Restschmelzen ist daher ein wichtiger Schritt in der chemischen Differenzierung der Erde, und einer möglichen Schichtung früh in ihrer Geschichte.

Die Charakterisierung und Modellierung der Phasenbeziehungen im Gleichgewicht mit der Schmelze im binären System MgO-SiO₂ bei Drücken des tiefen Erdmantels wird von der Lage der eutektischen Punkte für MgO-MgSiO₃ und MgSiO₃-SiO₂ bestimmt. Während für die eutektische Zusammensetzung für MgO-MgSiO₃ bei Drücken des oberen tiefen Erdmantels (~25 GPa) allgemeiner Konsens besteht, gibt es für MgSiO₃-SiO₂ große Unterschiede zwischen Experimenten in der Diamantstempelzelle und ab-initio Simulationen sowie darauf aufbauenden Modellen. Um diese Diskrepanz zu beheben, haben wir Experimente in der Vielstempelpresse für Mg_{0.4}Si_{0.6}O_{1.6} und Mg_{0.3}Si_{0.7}O_{1.7} bei 24 GPa und Temperaturen von 2650 ± 100 K und 2750 ± 100 K durchgeführt. Bei 2750 ± 100 K beobachten wir das Auftreten partieller Schmelze und die Probe mit Mg_{0.4}Si_{0.6}O_{1.6} als Ausgangszusammensetzung weist SiO₂-Stishovit als Phase am Liquidus auf. Eine Analyse der abgeschreckten Schmelze mit Hilfe der Elektronenmikrosonde ergibt $X_{\text{SiO}_2} = 0.53 \pm 0.03$ als eutektische Zusammensetzung. Aufbauend auf die experimentellen Ergebnisse entwickeln wir ein thermodynamisches Modell für die Schmelzbeziehungen im binären für MgO-SiO₂ System, und extrapolieren zum Druck an der Kern-Mantel-Grenze. Dieses Modell sagt voraus, dass sich die eutektischen Punkte bei 136 GPa weiter von MgSiO₃ entfernt haben, und die Temperaturen am Solidus für MgO-MgSiO₃ und MgSiO₃-SiO₂ ähnlich sind.

Wir haben die Schmelzexperimente in der Vielstempelpresse bei 24 GPa auf das System MgSiO₃-FeSiO₃ ausgedehnt, mit den Ausgangszusammensetzungen Mg_{0.9}Fe_{0.1}SiO₃, Mg_{0.8}Fe_{0.2}SiO₃, Mg_{0.7}Fe_{0.3}SiO₃ und Mg_{0.5}Fe_{0.5}SiO₃, bei Temperaturen von 2650 ± 100, 2615 ± 100, 2580 ± 100 bzw. 2510 ± 100 K. Aufnahmen der entnommenen Proben mit dem Rasterelektronenmikroskop zeigen die Koexistenz von Bridgmanit und Schmelze. Aus der chemischen Analyse mittels Elektronenmikrosonde kann die Gleichgewichtskonstante $K_D =$

$(\text{Fe}^{\text{solid}}/\text{Mg}^{\text{solid}})/(\text{Fe}^{\text{liquid}}/\text{Mg}^{\text{liquid}})$ für Eisen bestimmt werden: Mit zunehmendem FeSiO_3 -Gehalt sinkt K_D quasi-linear von $\sim 0.31 \pm 0.07$ auf $\sim 0.22 \pm 0.02$. Auf Grundlage dieser Verteilungsdaten und der Schmelzkurve der Oxide wird ein thermodynamisches Modell für das System FeO-MgO-SiO_2 konstruiert, und binäre Schmelzphasendiagramme für die Systeme MgO-SiO_2 , $\text{MgSiO}_3\text{-FeSiO}_3$, MgO-FeO und FeO-SiO_2 werden bei 24 und 136 GPa berechnet. Bei 24 GPa zeigen diese eine gute Übereinstimmung mit verfügbaren experimentellen Phasenbeziehungen auf, die nicht in die Modellbildung eingeflossen sind. Bei Bedingungen der Kern-Mantel-Grenze zeigt sich, dass Eisen stark in die Schmelze partitioniert, was, zusammengenommen mit der niedrigeren Temperatur des Solidus für FeO-reichen Schmelzen, eine mögliche Erklärung für die Niedrig-Geschwindigkeitszonen im untersten Erdmantel bietet.

Die Schmelzedichte ist ein Schlüsselparameter, der die Kristallisation des Magmaozeans beeinflusst. Wir haben Molekulardynamiksimulationen für flüssiges $\text{Mg}_{28}\text{Fe}_4\text{Si}_{16}\text{O}_{64}$ und $\text{Mg}_{32}\text{Si}_{16}\text{O}_{64}$ über einen weiten Kompressionsbereich (bis 370 GPa) bei 3000 K durchgeführt, unter Verwendung der generalisierten Gradienten Approximation plus lokaler Coulomb-Abstoßung (GGA + U) innerhalb der Dichtefunktionaltheorie. Wir finden Eisen in $\text{Mg}_{28}\text{Fe}_4\text{Si}_{16}\text{O}_{64}$ bis ca. 35 GPa in einem Zustand von hohem Spin, mit einem durchschnittlichen magnetischen Moment von $4.0 \pm 0.1 \mu_B$. Das magnetische Moment nimmt bei höherem Druck quasi-linear ab, und erreicht $0.5 \pm 0.4 \mu_B$ bei 370 GPa. Wir untersuchen die Schmelzstruktur und passen eine Tait-Zustandsgleichung an die isothermen Druck-Volumen Ergebnisse an. Die partiellen molaren Volumina von FeO und MgO sind über den gesamten Druckbereich praktisch identisch, was sich auch in sehr ähnlichen radialen Verteilungsfunktionen widerspiegelt. Allein aufgrund des Unterschieds im molaren Gewicht weist Olivinschmelze mit 25%mol Fe_2SiO_4 oberhalb von ~ 85 GPa eine höhere Dichte auf als der Erdmantel, was darauf hindeutet, dass ein basaler Magmaozean in der frühen Erde gravitativ stabil gewesen sein könnte, wenn man eine hohen K_D -Wert annimmt, wie er von unserem thermodynamischen Modell vorhergesagt wird.

Experimentelle Messungen der Struktur und der physikalischen Eigenschaften von Silikatflüssigkeiten sind aufgrund ihres hohen Schmelzpunkts schwierig. Viele Experimente stützen sich daher auf Silikatglase, die aus der Schmelze abgeschreckt wurden. Die Frage, ob solche Glase die Struktur der Flüssigkeit repräsentieren, kann jedoch nicht eindeutig

beantwortet werden. Wir haben daher Molekulardynamiksimulationen auf der Grundlage der Dichtefunktionaltheorie für Mg_2SiO_4 - und MgSiO_3 -Schmelzen bei 2000 K und Glas bei 300 K durchgeführt, die mit unterschiedlichen Raten aus der Schmelze abgekühlt wurden: sofortiges Abschrecken und 0.1 K pro Femtosekunde (langames Abkühlen). Bei der Analyse der resultierenden Glas- und Schmelzstruktur mittels radialer Verteilungsfunktionen und Strukturfaktoren zeigt sich, dass langsam abgekühltes Glas mehr strukturelle Merkmale aufweist als das abgeschreckte Glas und die Flüssigkeit. Die Unterschiede in den berechneten Strukturfaktoren für Röntgen- und Neutronenstrahlung sind jedoch zu gering und zwischen verschiedenen Experimenten zu groß, um zu verstehen, ob sich die Abkühlungseffekte in den Messungen widerspiegeln.

Table of contents

1 Introduction	1
1.1 Origin of the early Earth	1
1.2 Magma ocean hypothesis	1
1.3 Structure of Earth's mantle	3
1.4 Phase relations in the lower mantle	4
1.5 Aims of this Study	7
2 Melting relations in the lower mantle	9
2.1 MgO-SiO ₂ system	9
2.2 FeO-MgO-SiO ₂ system	10
2.3 Melting at core mantle boundary	12
3 Methods	15
3.1 Experimental methods	15
3.1.1 Multi anvil technique	15
3.1.2 Cell assembly	16
3.1.3 Starting material	19
3.1.4 Experimental Setup	19
3.1.5 Analytical procedure	20
3.1.5.1 Scanning Electron Microscope	21
3.1.5.2 Electron Probe Micro Analysis	23
3.2 Atomistic simulation	25
3.2.1 Density functional theory and molecular dynamics	25
3.2.2 Ab initio simulations using the Vienna Ab initio Simulation Package	26
3.2.3 Simulation setup	27
3.2.4 Radial distribution functions	28
3.2.5 X-ray and Neutron structure factors	29

4 Thermodynamics for lower mantle melting	31
4.1 Thermodynamic description of solids	31
4.2 Thermodynamic description of liquids	32
4.3 Thermodynamics of mixing	33
4.4 Prior thermodynamic description of the MgO-MgSiO ₃ system at 24GPa	34
4.5 Thermodynamic description in the MgO-SiO ₂ system	34
4.6 Thermodynamic description in the FeO-MgO-SiO ₂ system.....	35
4.7 Simple work flow of thermodynamic modelling	37
4.8 BurnMan package in python	37
5 Melting phase relations in the MgO-SiO₂ system under lower mantle pressure	39
5.1 Experimental results	39
5.2 Determination of thermodynamic parameters	42
5.3 MgO-SiO ₂ melting relations at experimental pressure at 24 GPa	45
5.4 MgO-SiO ₂ melting relations at lower mantle pressure	46
5.5 Melting near the core mantle boundary	51
5.6 Summary	52
6 Iron partitioning and melting phase relations in FeO-MgO-SiO₂ system under lower mantle conditions	55
6.1 Experimental results	55
6.2 Thermodynamic parameters in the FeO-MgO-SiO ₂ system	59
6.3 FeO melting curve under high pressure	60
6.4 Iron partitioning and FeO-MgO-SiO ₂ melting phase relations at 24 GPa	62
6.5 Iron partitioning and FeO-MgO-SiO ₂ melting phase relations at CMB	68
6.6 Summary and implications	70
7 Density of Fe-bearing silicate melts at mantle conditions	73
7.1 <i>P-V-T</i> equation of state and magnetic moment	74
7.2 Melt structure under high pressure	76
7.3 Density of melts under high pressure	78
7.4 Discussion and conclusion	79

8 Liquid and glass structure of Mg₂SiO₄ and MgSiO₃ from ab-initio simulations	81
8.1 Radial distribution functions	82
8.2 Structure factors	85
8.3 Oxygen-oxygen contributions to S_q	88
8.4 Glass under compression	90
8.5 Summary	91
9 Conclusions	93
9.1 Multi-anvil experiments	93
9.2 Thermodynamic modelling	94
9.3 Ab initio simulations	95
References	97
Acknowledgments	124

1. Introduction

1.1 Origin of the early Earth

According to the nebular hypothesis, the starting point of planetary formation is the protoplanetary disk which consists of a mixture of gases and dust in space, orbiting the Sun (e.g., Lissauer, 1993). Gravitational collapse within the disk leads to the formation of planetesimals (Simon et al., 2016). Interactions and collisions among these planetesimals produce lunar to Mars-size planetary embryos (Figure 1.1). Finally, the collision among planetary embryos as well as continuous accretion and differentiation processes set the initial thermal and chemical states of early Earth (Wetherill, 1990; Elkins-Tanton, 2012).

1.2 Magma ocean hypothesis

During planetary impact events, the transfer of kinetic and gravitational energy leads to a significant temperature increase for the planet's surface and interior, and induces large-scale melting and vaporization (Carter et al., 2020). A special impact event for Earth is the Moon-forming giant impact near 4.5 billion years ago (Asphaug, 2014), for which simulations indicate that the early Earth's mantle was largely or entirely molten (Nakajima and Stevenson, 2015), creating a magma ocean.

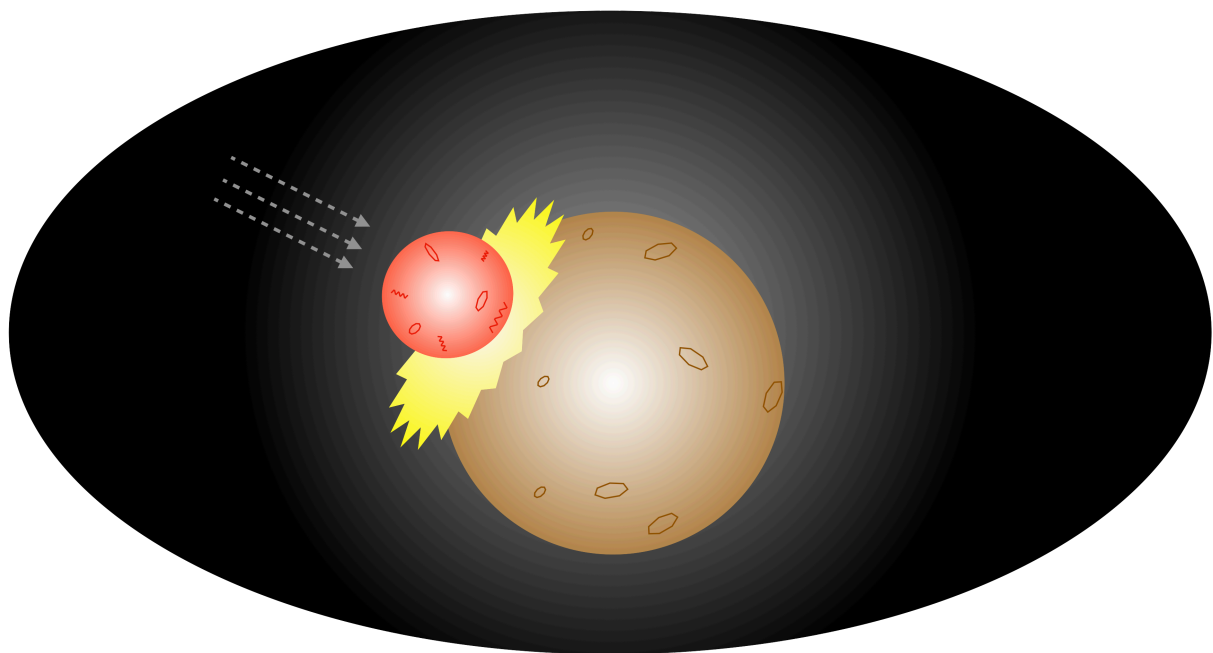


Figure 1.1: Schematic picture of a giant impact event where a smaller planetary embryo collides with a larger planetary embryo.

Within the magma ocean, the liquid metal separates from the molten silicates quickly due to its higher density and accumulates at the bottom of magma ocean as ponds or a global layer (Figure 1.2). Due to its density contrast with the underlying silicate mantle, the ponded iron continue sinks towards the center of the planet (Rubie et al., 2007). With the associated further release of gravitational energy (Wood et al., 2006), the planet heats up and sets the initial internal structure of the Earth. The subsequent cooling process leads to the magma ocean solidification while the core remains largely liquid. Two fundamental questions in the context of magma ocean crystallization are:

- (i) What is its timescale? Geodynamic simulations show that equilibrium crystallization, in which the liquid and crystals are mixed during cooling, leads to a short freezing period at the order of thousands of years (Maurice et al., 2017). A longer freezing period in the range of millions of years involve fractional crystallization, in which crystal and melt are separated to form different layers (Ballmer et al., 2017).
- (ii) Does magma ocean crystallization start from bottom up or in the middle of the mantle? If the magma ocean adiabat approaches the silicate liquidus at the bottom of the mantle first, crystallization progresses from the bottom up. As FeO generally fractionates into the liquid in such a crystallization process (Liebske et al., 2005), the

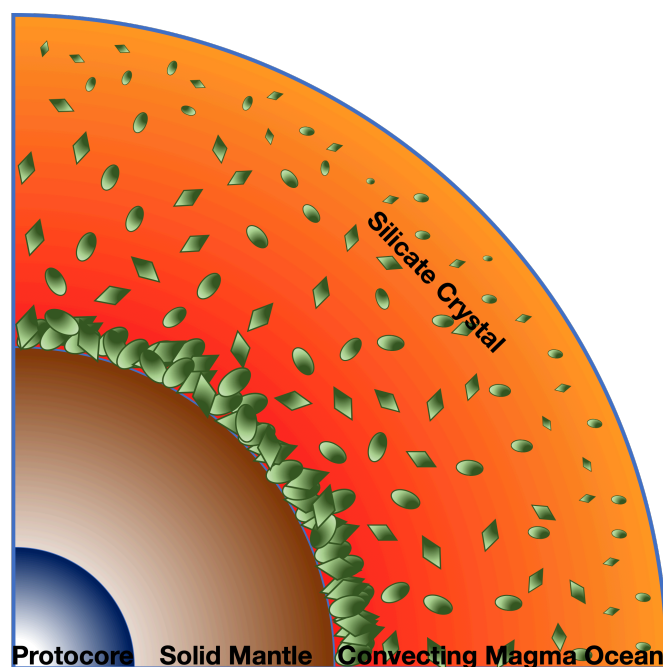


Figure 1.2: Schematic picture of early planetary differentiation and magma ocean solidification. The early planet is shown segregated into three parts: protocore, solid mantle and convecting magma ocean. Below the liquidus, silicate crystals are formed and sink through the magma ocean. (Modified from Maas and Ulrich, 2015).

silicate melt becomes successively denser, possibly leading to an unstable density stratification of the crystallizing mantle (Elkins-Tanton, 2008). An intersection of the magma ocean adiabat with silicate liquidus at intermediate depth in the mantle, by contrast, could lead to a scenario in which a basal magma ocean forms that is isolated from the progressing crystallization at shallower depth and may be thermally and chemically stable in the deepest mantle (Labrosse et al., 2007).

1.3 Structure of Earth's mantle

The Earth's interior is structured into an upper mantle, transition zone, lower mantle, the D'' layer on top of the core mantle boundary (CMB), the outer and inner core (Figure 1.3), a notion based on seismological models, such as the preliminary reference Earth model, PREM (Dziewonski and Anderson, 1981). On top of such an isotropic and homogeneous one-dimensional model of Earth's interior, lateral heterogeneity exists as shown by seismic imaging. At shallow depth, seismic tomography maps the subduction of oceanic plates into the mantle (Zheng et al., 2009; Martin-Short et al., 2018), a process that transports chemically differentiated material into the mantle, and the combined thermal and chemical effects lead to different seismic characteristics (Pozgay et al., 2006; Abers et al., 2006). Further prominent heterogeneous features are mapped in the vicinity of the transition zone (Tauzin et al., 2010) and above the CMB (McNamara, 2019).

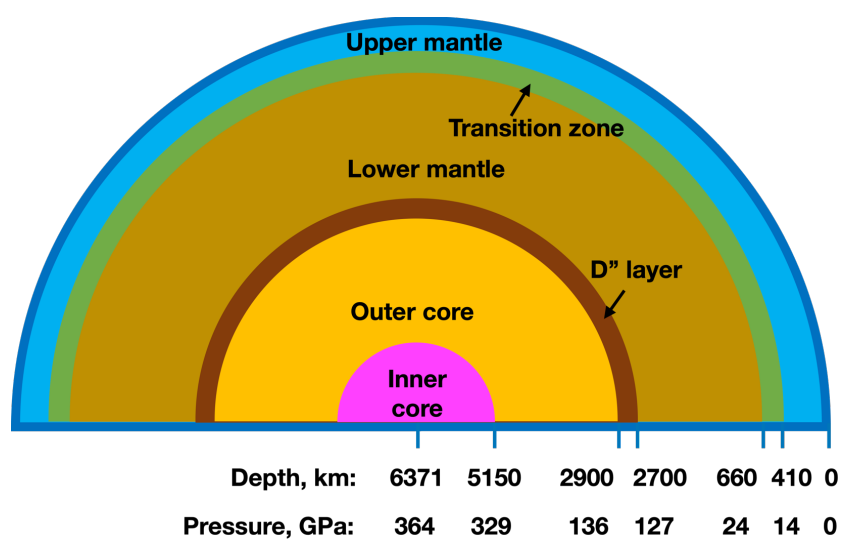


Figure 1.3: Internal structure of the Earth. At the boundaries of the major regions the corresponding depth and pressure values are indicated. (Modified from Kaminsky, 2017).

On top of the 410 km seismic discontinuity, a 30-100 km thick low-velocity layer is observed globally (Tauzin et al., 2010). Below the 660 km depth, seismic imaging underneath the regions of North America estimate a 2.6% surface wave velocity decrease. Both of these features have been interpreted by the difference in water solubility between the transition zone minerals and those of the upper and lower mantle (Schmandt et al., 2014), an idea first proposed as the transition-zone water filter by Bercovici and Karato (2003).

In the lowermost mantle, seismic tomography shows two distinct features, Ultra-Low Velocity Zones (ULVZs) and Large Low Shear Velocity Provinces (LLSVPs) (McNamara 2019). ULVZs are 5-40 km thick and 50-100 km wide, with no lateral continuities and show reduced P and S wave velocities by 10-30%, corresponding to a density increase by ~10% compared to the surrounding mantle (McNamara et al., 2010). Two LLSVPs beneath the Africa and the Pacific are hundreds of km in height and thousands of km in width, which makes them one order of magnitude larger than the ULVZ (McNamara, 2019). The origin and stability of these two types of lower mantle features are still under debate, with crustal material accumulation through subduction on top of the CMB (Dobson and Brodholt 2005), remnants of basal magma ocean (Labrosse et al., 2019) or core-mantle interactions (Song and Ahrens, 1994) being discussed. Such complexity comes on top of the fact that the D'' layer at the bottom of the lower mantle represents a thermal boundary layer where the temperature along the geotherm increases rapidly from the mantle adiabat with ~2600 K at 2700 km (Katsura et al., 2010) to ~4000 K at the CMB to match the core temperature (Anzellini et al., 2013).

1.4 Phase relations in the lower mantle

High-pressure petrology and mineral physics provide the key in understanding both the one- and three-dimensional structure as they investigate mineral phase assemblages and physical properties of representative mantle compositions and minerals in experiments and computations.

The bulk composition is the primary parameter controlling the mantle phase relations as a function of pressure (P) and temperature (T). A representative upper mantle composition, pyrolite, has been estimated from partial melting experiments that generate basaltic magma and peridotitic residues (Ringwood, 1991), mimicking the process of mid-ocean ridge basalt

Table 1.1: Chemical composition of pyrolite and mid ocean ridge basalt (MORB) in wt% of oxides. The two pyrolite models are from Sun (1982) and Green et al. (1979), MORB from Gale et al. (2013).

	Pyrolite	Pyrolite	MORB
SiO ₂	44.49	45.0	50.47
TiO ₂	0.22	0.17	1.68
Al ₂ O ₃	4.30	4.4	14.70
Cr ₂ O ₃	0.44	0.45	-
CaO	3.50	3.4	11.39
MgO	37.97	38.8	7.58
FeO	8.36	7.6	10.43
NiO	0.25	0.26	-
MnO	0.14	0.11	0.184
Na ₂ O	0.39	0.4	2.79

(MORB) extraction in the Earth. The pyrolite composition (Table 1.1) is dominated by MgO and SiO₂ (> 80 wt%); adding FeO accounts for > 90 wt%. In the context of subduction and the associated introduction of chemical heterogeneity into the mantle, hydrous MORB plays an important role for transporting water into the transition zone that then helps to operate the water filter discussed above (Maruyama and Okamoto, 2007; Ohtani et al., 2004); also, as a dry composition it may facilitate partial melting at the CMB when accumulated there (Andraut et al., 2014; Pradhan et al., 2015). Compared to pyrolite, MORB is enriched in SiO₂, Al₂O₃, CaO and depleted in MgO (Table 1.1).

In the pyrolite composition, the upper mantle (~35-410 km depth) is dominated by three mineral phases (Figure 1.4): olivine, garnet and pyroxene, with the pyroxene successively dissolving in the garnet (e.g., Fumagalli and Klemme, 2015), becoming more majoritic in compositions, i.e., dominated by MgSiO₃. At ~14 GPa and ~1673 K olivine transforms to wadsleyite (α - to β -Mg₂SiO₄) (e.g., Akaogi et al., 1989) which coincides with the 410 km seismic discontinuity. The wadsleyite to ringwoodite transition (β - to γ -Mg₂SiO₄) is observed at ~19 GPa and ~1700 K (e.g., Akaogi et al., 1989), and associated with a small discontinuity at 520 km depth, in the middle of transition zone (Deuss and Woodhouse, 2001). At ~24 GPa and ~1900 K, Mg₂SiO₄ ringwoodite decomposes into MgSiO₃ bridgmanite and MgO periclase, which defines the 660 km discontinuity (Ito and Takahashi 1989). The MgSiO₃ majorite to bridgmanite phase transition occur at around 23 GPa and ~2073 K (Ishii et al., 2011). CaSiO₃ perovskite forms from the exsolution of majorite garnet

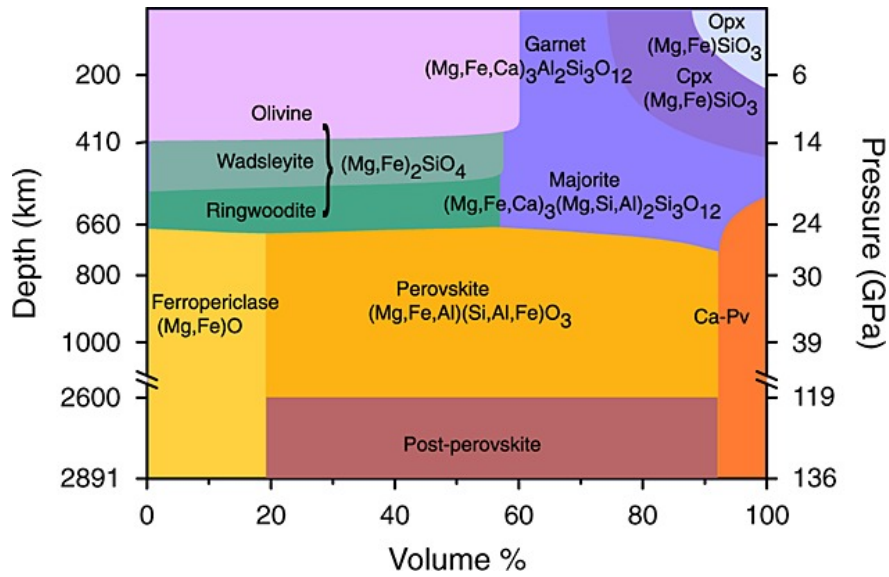


Figure 1.4: Phase assemblage for a pyrolite composition of the Earth's mantle as a function of pressure and depth. Abbreviations: Ca-Pv for CaSiO₃-perovskite, Cpx for clinopyroxene and Opx for orthopyroxene (from Lin et al., 2013).

range from 20 to 24 GPa at ~1900 K (Saikia et al., 2008). In the lower mantle, bridgmanite dominates the phase assemblage with ~75 vol%, ferropiclasite and CaSiO₃-perovskite are present with ~18 vol% and ~7 vol%, respectively (Irifune et al., 2010, Lin et al., 2013). At conditions just above the CMB, MgSiO₃ bridgmanite transforms to the MgSiO₃ post-perovskite phase (Murakami et al., 2004) which further complicates the picture of the D'' layer.

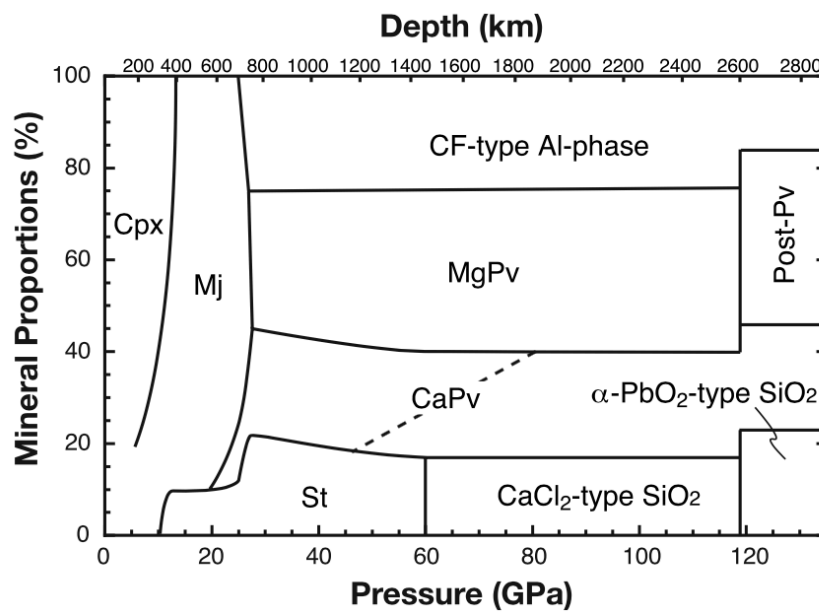


Figure 1.5: Phase assemblages and mineral proportions in wt% for MORB bulk composition in Earth's mantle as a function of pressure and depth. (from Hirose, 2006).

For MORB, due to its higher Al_2O_3 and SiO_2 content (Table 1.1), at lower mantle conditions a separate aluminous phase, e.g., calcium ferrite type MgAl_2O_4 (Funamori et al., 2000) (~20 vol%) and stishovite (~20 vol%) appear instead of ferropericlase (Figure 1.5); the bridgmanite abundance in the phase assemblage decreases to ~40% and that of CaSiO_3 -perovskite increase to ~20 vol%, reflecting its higher chemical abundance (Dorfman, 2016).

1.5 Aims of this Study

Measuring and reliably modelling the melting phase relations in the MgO-SiO_2 and FeO-MgO-SiO_2 systems at conditions of the Earth lower mantle is of great importance in this context for two reasons:

- (i) It will advance our understanding of magma ocean solidification in terms of T (liquidus and solidus) and crystallizing phases.
 - (ii) Differences in melt relations and solidus T for peridotite and MORB compositions will help to address the potential origin of heterogeneities in the Earth's deep mantle.
- Here, we perform multi anvil (MA) press experiments at 24 GPa to explore the melting phase relations in the MgO-SiO_2 and the FeO-MgO-SiO_2 systems, fit to a thermodynamic model and extrapolate it to CMB pressure.

Similarly, melt density is important in understanding early and modern mantle evolution. It controls the stability of melt that may form in the deep mantle (buoyancy), and the dynamics during magma ocean crystallization:

- (i) Partitioning of FeO measured in the MA experiments will put constraints on the density difference between melt and crystallizing solids.
- (ii) Ab initio molecular dynamics simulations on FeO-bearing and FeO-free silicate liquids will help to establish a molar volume of FeO in silicate liquids that can then be compared to the MgO molar volume to see whether density differences are purely caused by differences in the molar weight. In this context, the spin transition in Fe in the silicate melt is an important consideration which may in turn influence FeO partitioning (Nomura et al., 2011) and FeO molar volume (Andrault et al., 2012).
- (iii) The structure of melt is fundamental in understanding its density and density changes under high pressure, but in situ measurements are difficult to perform (Sanloup et al., 2013). Instead, quenched glass is often used as an analogue for melt structure

(Nomura et al., 2011). In a series of molecular dynamics simulations, we explore structure difference between melt and glass by cooling the melt to a glass.

2. Melting relations in the lower mantle

2.1 MgO-SiO₂ system

As outlined in Section 1.4, the two-component MgO-SiO₂ system is important both for mantle and basalt compositions, and understanding phase relations in it is therefore of fundamental importance for lower mantle melting. However, melt relations in this system have not yet been fully characterized in experiments.

At 24 GPa, along the MgO-SiO₂ join, the liquid coexists with solid MgO periclase (pc), MgSiO₃ bridgmanite (brg) and SiO₂ stishovite (sti) (Figure 2.1). The whole join contains two eutectic locations in the MgO-MgSiO₃ and MgSiO₃-SiO₂ subsystems, where the liquid coexists with two solid phases. Given a molar ratio MgO/SiO₂~1.22 or $X_{\text{SiO}_2} = 0.45$ (with $X_{\text{SiO}_2} = \frac{\text{SiO}_2}{\text{SiO}_2 + \text{MgO}}$) for the bulk silicate Earth (Palme and O'Neill, 2003) and $X_{\text{SiO}_2} = 0.39$ for pyrolite (Table 1.1), many experiments on melt relations in MgO-SiO₂ have focused on MgO-MgSiO₃ (Liesbke and Frost, 2012; Ohnishi et al., 2017). However, basalt reservoirs with a higher SiO₂ content (Table 1.1) ($X_{\text{SiO}_2} = 0.53$) have been considered as potential sources for partial melting near the CMB (Section 1.3).

Experiments on melt relations in the MgO-SiO₂ system at lower mantle P have been performed in the MA press by Liesbke and Frost (2012) and in the diamond anvil cell (DAC)

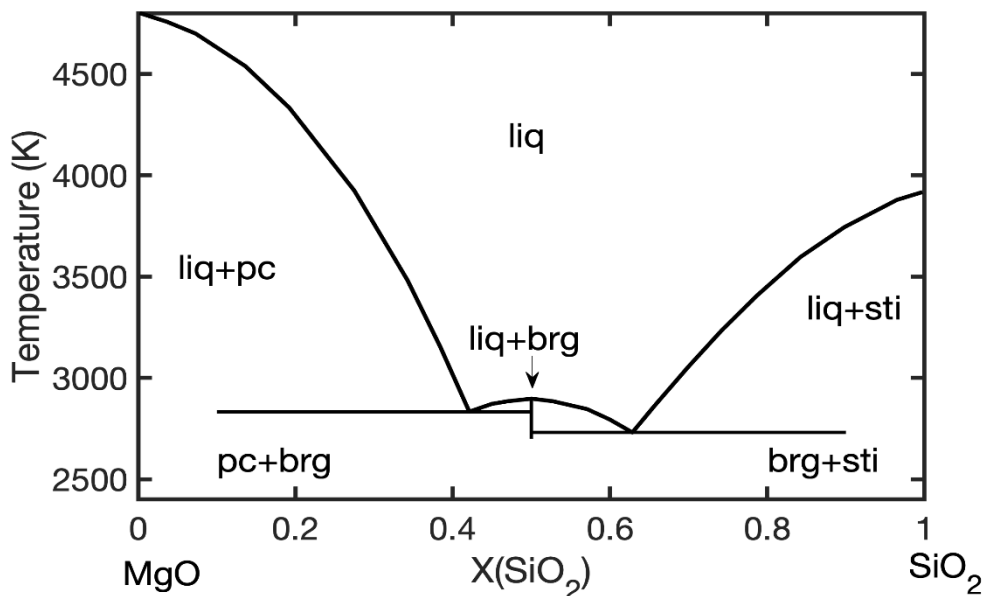


Figure 2.1: Melting phase relations in the MgO-SiO₂ system at 24 GPa from de Koker et al. (2013). Abbreviations: liq for liquid, pc for periclase, brg for bridgmanite and sti for stishovite.

by Baron et al. (2017), Ohnishi et al. (2017) and Ozawa et al. (2018), modeled based on ab initio simulations by de Koker et al. (2013), and thermodynamically described by Boukaré et al. (2015), Miyazaki and Korenaga (2019) and Belmonte et al. (2017). Bridgmanite is the phase on the liquidus in the vicinity of MgSiO_3 , with two eutectics points bracketing its stability; this stability field has been found to expand with P .

At $P = 24 - 25$ GPa, the eutectic composition on the MgO-MgSiO_3 join is consistently determined as $X_{\text{SiO}_2} = 0.43 \pm 0.01$ (Liebske and Frost, 2012; de Koker et al., 2013; Boukaré et al., 2015; Ohnishi et al., 2017; Ozawa et al., 2018; Belmonte 2017) with some uncertainty in T , ranging from ~ 2700 K (Liebske and Frost, 2012) to ~ 2900 K (Boukaré et al., 2015). For the $\text{MgSiO}_3\text{-SiO}_2$ system, however, the eutectic location differs significantly between various studies with $X_{\text{SiO}_2} = 0.51 - 0.63$ (de Koker et al., 2013; Belmonte et al., 2017; Ozawa et al. 2018). Melting relations in the $\text{MgSiO}_3\text{-SiO}_2$ system have not been studied in the MA press, although it provides better control of thermal gradients and allows for a more rigorous textural analysis of the larger sample compared to DAC experiments. In the current thesis, we perform MA melting experiments at $P = 24$ GPa with $\text{Mg}_{0.4}\text{Si}_{0.6}\text{O}_{1.6}$ and $\text{Mg}_{0.3}\text{Si}_{0.7}\text{O}_{1.7}$ starting compositions, complementing the work by Liebske and Frost (2012).

2.2 FeO-MgO-SiO₂ system

The presence of FeO in mantle composition leads to a decrease in both the liquidus and solidus T relative to the MgO-SiO_2 system (Liebske and Frost, 2012; Andrault et al., 2011) which brings the solidus of mantle compositions significantly closer to the geotherm in the D'' region; variations in composition – such as between pyrolite and MORB (Table 1.1) – may then suffice to create partial melts, explaining the presence of the ULVZ there (Fiquet et al., 2010; Andrault et al., 2014). Also, as the heaviest major element in the silicate mantle, FeO partitioning between melt and minerals has direct consequences on the composition of a crystallizing layer and its stability during the magma ocean cooling process (Ballmer et al., 2017).

Measurements of iron partitioning between solid and liquid silicates at lower mantle pressures provide a heterogeneous picture (Figure 2.2): Multi anvil experiments at 24 GPa give an equilibrium constant $K_D = (\text{Fe}^{\text{solid}}/\text{Mg}^{\text{solid}})/(\text{Fe}^{\text{liquid}}/\text{Mg}^{\text{liquid}})$ with values in the range

and opposing trends in K_D for lower mantle pressures (Figure 2.2) for liquid compositions in equilibrium with bridgmanite.

A robust quantitative thermodynamic model in the FeO-MgO-SiO₂ system is important for understanding these discrepancies, and requires more experimental and modelling efforts. Here, we perform a series of multi anvil melting experiments at 24 GPa for starting compositions in the (Mg_{1-x}Fe_x)SiO₃ system with $x = 0.1, 0.2, 0.3$ and 0.5 to provide strong constraints on such a model. Coexisting liquid and solid portions of recovered samples are analyzed in terms of chemical compositions and used to determine parameters in a new thermodynamic model in the FeO-MgO-SiO₂ system applicable to lower mantle conditions.

2.3 Melting at core mantle boundary

Partial melting above the CMB can – in principle – be identified by comparing the solidus of mantle rocks with the geotherm. While through much of the lower mantle partial melting is unlikely as the solidus temperature of peridotite and basalt remains above a wide range of geotherm models (Fiquet et al., 2010; Andrault et al., 2014), it may occur in the D'' layer, where temperature increases rapidly to match that of the core (Anzellini et al., 2013) (Figure 2.3).

For the peridotite system, two DAC studies measure similar solidus T with 4150 ± 150 K at CMB pressure (Andrault et al., 2011; Fiquet et al., 2010), ~ 200 K higher than the mantle geotherm (Anzellini et al., 2013). By contrast, for the basalt system, two DAC studies find solidus T at 3800 ± 150 K (Andrault et al., 2014) and 3900 ± 150 K (Pradhan et al., 2015), respectively, slightly below the geotherm temperature. This indicates that the basalt can potentially partially melt near the CMB, while peridotite does not. It is not clear in this context whether the differences in the phase assemblage (Figures 1.4 and 1.5) or in the chemical composition of the phases involved play the key role in lowering the solidus temperature. Diamond anvil cell (Tateno et al., 2014; 2018) and multi anvil experiments (Kuwahara et al., 2018) provide some insight: For basalt both studies report bridgmanite as the phase on the solidus at lower mantle pressure, while CaSiO₃-perovskite – present in both assemblages – crystallizes at lower T for peridotite. This suggests that changes in composition for bridgmanite in basalt versus peridotite leads to a significantly lower melting temperature. The lack of a mineral phase in the basalt assemblage (Figure 1.5) that takes up any significant FeO and a higher FeO content of partial melts from basalt composition at

lower mantle conditions (Pradhan et al., 2015; Kuwahara et al., 2018, Tateno et al., 2018) supports this hypothesis.

In this scenario, eutectic melting in the two-component MgO-MgSiO₃ (containing the MgO/SiO₂ ratio representative of a peridotite) and the MgSiO₃-SiO₂ systems (with a MgO/SiO₂ ratio representative of a basalt) provides fix points to constrain the melting in the complex natural systems. The eutectic in the MgO-MgSiO₃ system has been considered extensively from DAC experiments and thermodynamic modelling, unfortunately resulting in differences in T of ~ 800 K at CMB pressure; the MgSiO₃-SiO₂ system has not been explored to the same extent, and we therefore perform MA experiments on melting relations in the MgSiO₃-SiO₂ system at uppermost lower mantle pressures to tightly constrain eutectic compositions and temperatures.

Adding iron into the MgO-SiO₂ system, solidus T_m of (Mg_{0.9}Fe_{0.1})₂SiO₄ is reported ~ 270 K lower than the pure Mg₂SiO₄ at 8.5 GPa (Ohtani et al., 1998). For the same bulk composition, at 24 GPa, the depression of solidus temperature is estimated at ~ 400 K based on the experimental results (Liebske and Frost, 2012) and 180 K from the scaling arguments (de Koker et al., 2013). Temperature effects of FeO on the MgO-SiO₂ melting remain not very well constrained. And large solidus temperature differences exist among various studies (Liebske and Frost, 2012; Trønnes and Frost 2002; Ohtani et al., 1998). A more systematic study of melting in the FeO-MgO-SiO₂ system is still necessary and important for the uppermost part of Earth lower mantle.

When increasing P to the lower mantle depth, solidus T of peridotite was measured at ~ 4150 near CMB by two DAC studies (Fiquet et al., 2010; Andrault et al., 2011). At the same pressure, in the basalt system, DAC research reported similar solidus T at ~ 3964 K by Andrault et al. (2014) and ~ 3710 K by Pradhan et al. (2015), which are close to the mantle geotherm near CMB. Iron oxide is considered as the primary factor causing the solidus temperature decrease compared to the MgO-MgSiO₃ and MgSiO₃-SiO₂ system at the same pressure (Liebske and Frost, 2012). Due to the large variations of solidus T in iron free system, quantitatively determining the FeO effects on solidus melting temperature in the MgO-SiO₂ join under high pressure remain challenge.

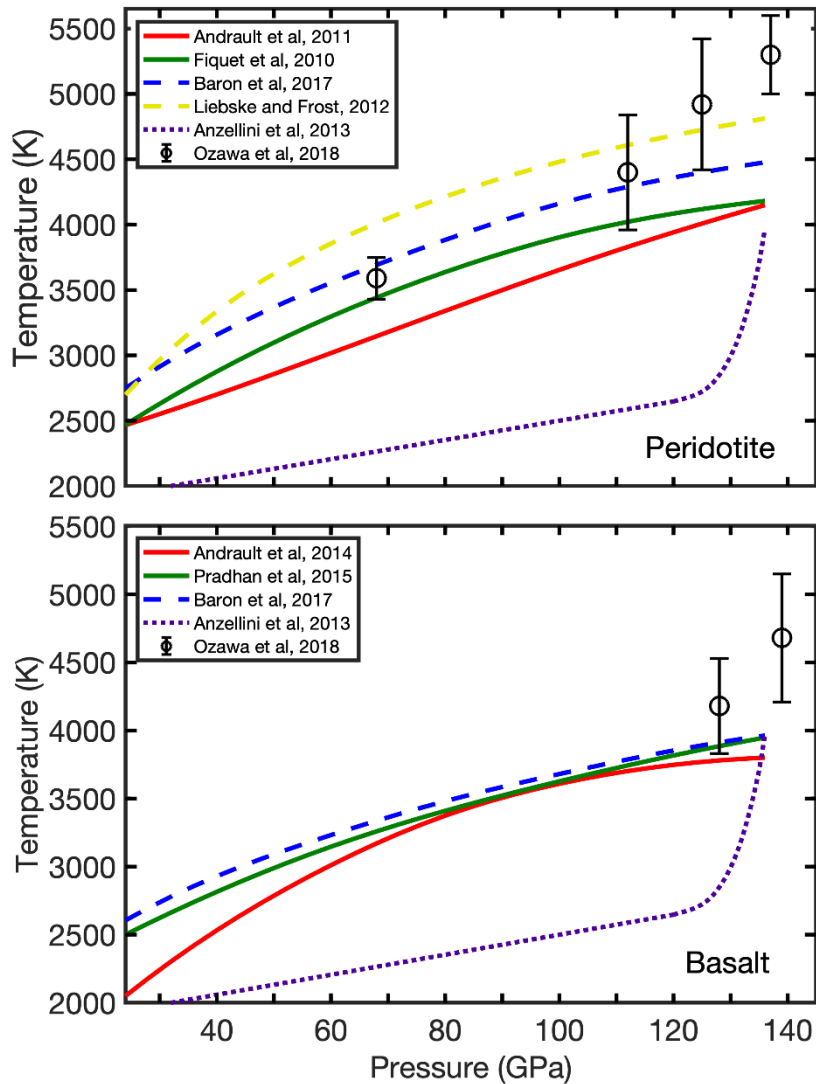


Figure 2.3: Comparison of solidus curves for rocks at lower mantle pressures with a model mantle geotherm (Anzellini et al., 2013; dotted purple) in the peridotite (top) and basalt system (top). Solidus curves for natural (or natural model) samples are from Fiquet et al. (2010) and Pradhan et al. (2015) in green solid lines for KLB-1 peridotite and a natural basalt, respectively, and from Andraut et al. (2011; 2014) for a chondritic mantle composition and a natural basalt in red solid curves. For comparison, the modeled solidus curve (eutectic T) in the MgO-MgSiO_3 system by Liebske and Frost (2012) is shown in yellow dashed (top), and in both the MgO-MgSiO_3 and $\text{MgSiO}_3\text{-SiO}_2$ systems by Baron et al. (2017) in blue dashed. Temperatures of both eutectics in the MgO-SiO_2 system determined by Ozawa et al. (2018) in diamond anvil cell experiments are included as black open symbols.

3 Methods

3.1 Experimental methods

The developments of high-pressure techniques in the laboratory provide access to conditions of Earth's interior (e.g., Ringwood and Major, 1970), with the multi anvil apparatus (Kawai and Endo, 1970; Keppler and Frost, 2005; Xie et al., 2020) and the diamond anvil cell (Mao and Bell, 1972; Ohta et al., 2020) being the two most popular devices. The multi anvil assembly permits sample size up to a few millimeters, much larger than the DAC (few μm) which allows a more detailed analysis of recovered samples (Leinenweber et al., 2012) and provides better control of experimental conditions. Diamond anvil cells, by contrast, can generate much higher P and T , routinely achieving conditions of the lowermost mantle (Ozawa et al., 2018; Tateno et al., 2014). They allow in-situ X-ray diffraction and spectroscopic measurements of materials, which is currently very challenge in MA (Sanloup et al., 2013; Cerantola et al., 2017; Fedotenko et al., 2019; Xie et al., 2020). However, melting (Andrault et al., 2011; Nomura et al., 2014) and partitioning studies (Nomura et al., 2011; Andrault et al., 2012) in the DAC show large uncertainty at lower mantle conditions (e.g., Figure 2.2) and lead to substantial debates on geochemical (Baron et al., 2017; Ozawa et al., 2018) and geophysical properties (Lin et al., 2013; Bardo, 2014) of mantle materials. Therefore, we employ the MA press to explore the melting phase relations in the MgO-SiO₂ and FeO-MgO-SiO₂ systems at 24 GPa in a well-controlled experimental environment, constrain thermodynamic models and then extrapolate the model to higher pressure and temperature conditions in order to predict melting relations at CMB conditions.

3.1.1 Multi anvil technique

Multi anvil experimental setups can be divided into three types, based on the geometry of the pressure media containing the sample capsule, with four, six and eight compressing anvils, representing a tetrahedral (Hall, 1958), cubic and octahedral (Kawai and Endo, 1970) assembly. A press generates hydraulic force – and therefore pressure – onto the small sample volume within the cell assembly through two stages of anvils.

All experiments in this study are performed in the 1200-ton octahedral Kawai-type Sumitomo press at Bayerisches Geoinstitut (BGI). The hydraulic system drives the lower ram to compress the split sphere (primary anvils) cavity, which accommodates an assemblage of

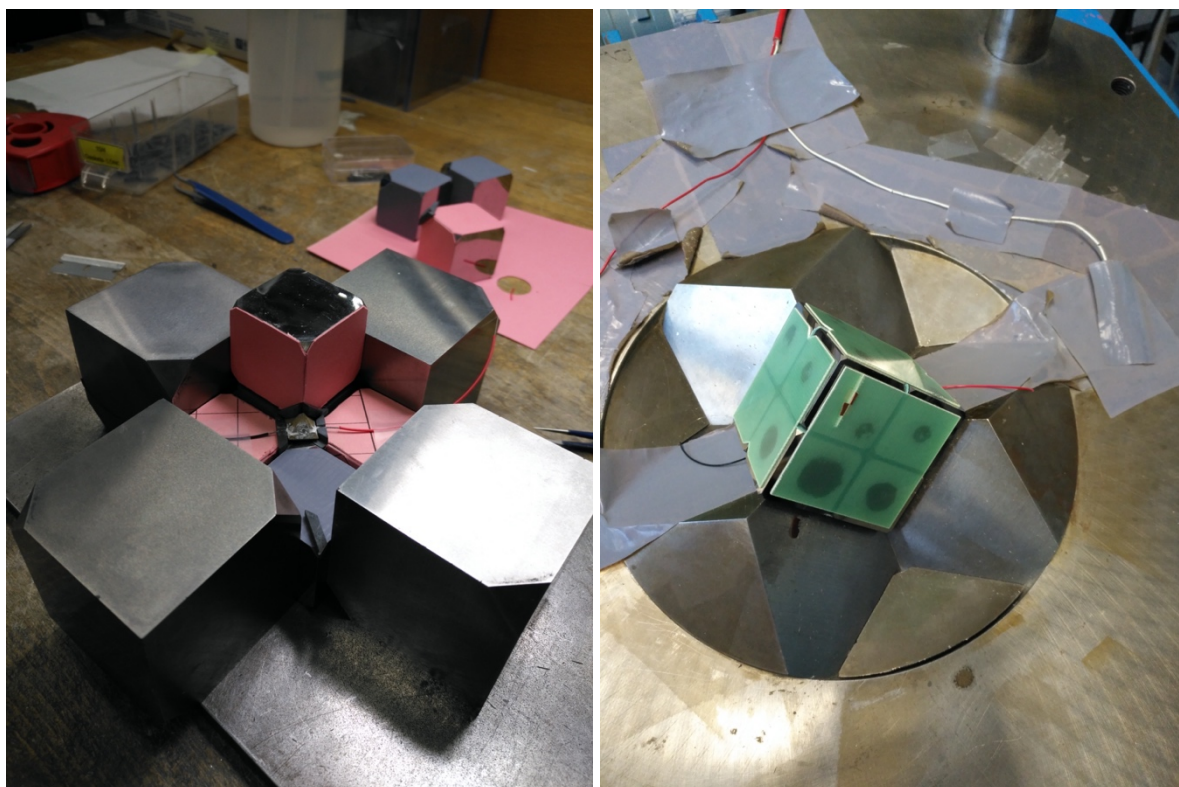


Figure 3.1: *On the left, the Cr₂O₃-doped MgO octahedron is placed at the center of eight tungsten carbide (WC) secondary anvils. Thermocouple is inserted within the cell assembly, in touch with the capsule inside. Small grey pyrophyllite gaskets are set between the anvils and octahedra. On the right, the first-stage anvils are well packed within plastic plates; two small pieces of copper foil on the faces of the WC cubes (gold color) are used for the transmission of electricity.*

eight tungsten carbide (WC) secondary anvils (Figure 3.1) that form an octahedral cavity through truncations. The size of the truncation is selected depending on the target pressure, defined as the force applied onto per unit area, with a smaller truncation achieving higher P . A pressure of 24 GPa in our work, corresponding to the uppermost part of Earth's lower mantle, requires a 7 mm octahedral edge size and 3 mm WC anvil truncations (7/3 assembly). Pressure calibration in this study follows those routinely used in BGI, which are established from phase transitions such as coesite to stishovite and majorite to bridgmanite (Keppeler and Frost, 2005; Frost et al., 2004). The temperatures are estimated based on one experiment from this study and previous power temperature relationships (Figure 3.2), with corrections concerning pressure effects on T following the equation 4 in Nishihara et al. (2020).

3.1.2 Cell assembly

The cell assembly is usually composed of five parts: pressure medium, furnace, MgO sleeves, sample capsule and sample powder (Figure 3.2). The pressure medium, an MgO octahedra doped with 5 wt% Cr₂O₃, transmits P between anvils and the sample volume. Its edge length

is usually larger than the truncation size so that contact between anvils is avoided during the compression. The furnace connects two opposite anvils through conductive materials and sends an electric current (I) through the sample capsule that provides heat to the system, with

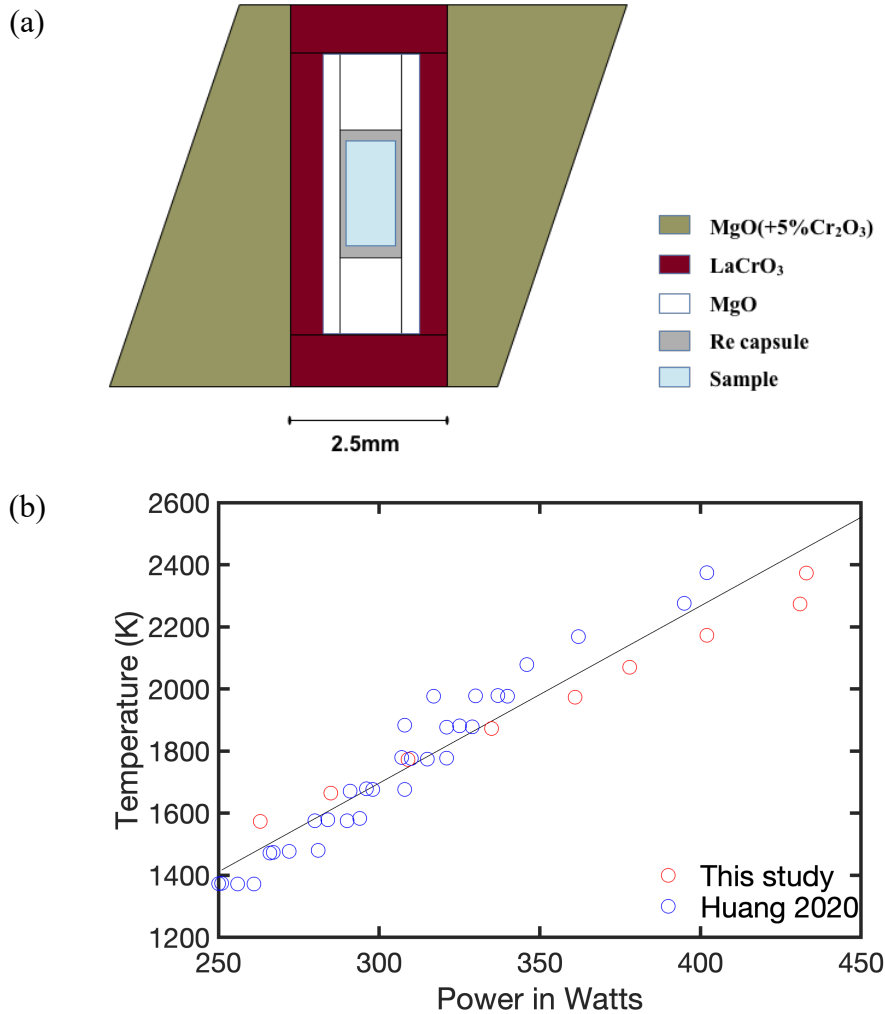


Figure 3.2: Schematic representation of a 7/3 multi-anvil assembly (a) with a single chamber capsule. The LaCrO₃ heater and Re capsule, containing the sample powder, are separated by MgO as a pressure medium and included in a Cr₂O₃-doped MgO octahedron. (b) Power temperature relationship for 7/3 assembly using 1200 t Sumitomo press in BGI. Red are data in this study, blue are from Huang 2020, black is fitted curve from all data.

the power of heating (P) is proportional to the resistance (R) and square of the current, $P = I^2 \cdot R$. Commonly used furnace materials are graphite, rhenium and lanthanum chromite (LaCrO₃). We use a LaCrO₃ furnace that provides stable energy supply up to high T of ~ 3000 K which are the target of our experiments.

The sample capsule is used for containing the sample powder, and is usually made of graphite, rhenium, gold or platinum, each appropriate for different types of experimental purposes. Gold, for example, does not form intermetallic alloys with iron, platinum absorbs iron, but has a much higher melting temperature than gold, and both of them can seal water in the system. We use a rhenium capsule, taking advantage of its high melting T (~ 3750 K at 24 GPa) (Yang et al., 2012) and negligible iron absorption (McCammon, 1997). MgO sleeves are placed between the furnace and capsule, serve as an electric insulator. A thermocouple can be inserted into the assembly, touching the capsule without direct contact to the furnace. Here we use W-Re ($W_{97\%}Re_{3\%}$ - $W_{75\%}Re_{25\%}$) wires with a diameter of 0.05 mm.

Soft pyrophyllite gaskets are usually glued near the truncation edges of the anvils and positioned between the pressure media and anvils to balance the applied forces. They aid in evenly distributing the applied pressure on the sample and are usually fixed by the pasted cardboards in the back (Figure 3.1).

3.1.3 Starting material

For the experiments in the MgO-SiO₂ system, the synthesis of compositions along the MgSiO₃-SiO₂ join (Mg_{0.4}Si_{0.6}O_{1.6} and Mg_{0.3}Si_{0.7}O_{1.7}) requires MgSiO₃ glass, for which analytical-grade MgO and SiO₂ powders (1:1 molar ratio) are mixed in ethanol, dried under infrared light, and ground to a fine powder. The mixture is melted in a Pt crucible for 30 minutes at 1650 °C and quenched by dropping the crucible into water. The MgSiO₃ glass is repeatedly ground to a fine powder in ethanol and then dried. Mg_{0.4}Si_{0.6}O_{1.6} and Mg_{0.3}Si_{0.7}O_{1.7} powders are prepared by mixing the ground enstatite glass with SiO₂ powder; they are stored under vacuum to prevent hydration.

In the FeO-MgO-SiO₂ system, we first prepare the starting material with pyroxene stoichiometry by carefully weighting the dried oxides MgO, Fe₂O₃ and SiO₂ with a molar ratio 1/18, 1/8, 3/14 and 1/2 for Fe₂O₃:MgO (Table 3.2). The sample powder is mixed in ethanol, ground to fine powder and dried under infrared light. To keep the composition homogeneous, the starting mixture is put in a iron-doped Pt crucible (to prevent iron absorption by the crucible) and melted for 2 hours at 1600°C in the oven. We quench the melt into glass by dropping the crucible into water. The glass is ground to a fine power, compressed into a pellet and reduced in the gas mixing furnace at $\log f(O_2) = -10$ and 1200°C for two days. Finally, we grind the pellet into fine power, and store it in vacuum to avoid hydration.

3.1.4 Experimental Setup

For the melting experiments in the 1200 t Sumitomo MA press, the sample powder is put in a Re capsule (~2 mm in length and ~1 mm in diameter), closed with a Re foil disk on top and bottom, and inserted in a Cr₂O₃-doped MgO octahedron (7 mm edge length) (Figure 3.2). Cell assembly parts are stored in an oven at 1000 °C for 12 h to dehydrate prior to use. The octahedron is compressed by tungsten carbide anvils with 3 mm corner truncations. The assembly is compressed to $P = 24$ GPa, heated to the target T and kept there for 1-2 minutes. The run product is quenched by shutting off the power and slowly decompressed to ambient conditions over 16 hours. For the MgO-SiO₂ system, we perform experiments without thermocouples and use a heating power-temperature relation determined in an independent experiment at $P = 24$ GPa with the same setup to a power of 433 W ($T = 2375$ K), and extrapolate to 450-470 W applied here (Table 3.1). To account for the P dependence of

Table 3.1: Experimental run conditions for the multi anvil press experiments performed in the MgSiO₃-SiO₂ system at 24 GPa. Abbreviations for the phases are: *sti* for stishovite, *brg* for bridgmanite and *liq* for the liquid.

Experiment	Initial composition	Power (W)	Temperature (K)	Phases	Liquid composition (mol%)	
					SiO ₂	MgO
S7110	Mg _{0.4} Si _{0.6} O _{1.6}	450	2650 ± 100	sti, brg	-	-
S7152	Mg _{0.3} Si _{0.7} O _{1.7}	450	2650 ± 100	sti, brg	-	-
S7172	Mg _{0.3} Si _{0.7} O _{1.7}	469	2750 ± 100	sti, brg, (liq)	-	-
S7238	Mg _{0.4} Si _{0.6} O _{1.6}	470	2750 ± 100	liq, st	53±3	47±2

thermocouple electromotive force, we follow Nishihara et al. (2020) and add a correction to estimate the T of the experiments, with an uncertainty of ± 100 K. Thermocouples tend to fail at the conditions explored (e.g., Liebske and Frost, 2012), and using power instead makes T conditions in the experiments far more reproducible.

The cell assemblages for the iron bearing starting compositions are the same as for the iron-free experiments. We perform four melting experiments at 24 GPa with temperature ranging from 2510±100 to 2650±100 K established by thermocouple reading, also corrected as discussed above (Table 3.2).

3.1.5 Analytical procedure

The recovered products are mounted within the epoxy with the long axis of the capsule positioned parallel to the horizontal line. Samples are slowly polished until the middle of the capsule and then coated by a ~12 nm thickness carbon layer. Images of the run products are acquired from the LEO1530 scanning electron microprobe (SEM) with acceleration voltage 20 kV and beam current 10 nA (Figure 3.3). Liquid structure and solid phases are identified by texture and quenched grains sizes. With energy-dispersive X-ray spectroscopy (EDS), we semi-quantitatively determined the chemical composition of the target area for phase analysis.

Table 3.2: Experimental run conditions for the multi anvil press experiments performed in the (Mg_{1-x}Fe_x)SiO₃ system at 24 GPa. Abbreviations for the phases are: *brg* for bridgmanite, *mw* for magnesiowüstite, *st* for stishovite, and *liq* for the liquid.

Experiment	Initial composition	Power (W)	Temperature (K)	Phases
S6953	(Mg _{0.9} Fe _{0.1})SiO ₃ , 1 wt% Ni Cr V	449	2650 ± 100	liq, brg
S6992	(Mg _{0.8} Fe _{0.2})SiO ₃ , 1 wt% Ni Cr V	443	2615 ± 100	liq, brg
S7024	(Mg _{0.7} Fe _{0.3})SiO ₃ , 1 wt% Ni Cr V	435	2580 ± 100	liq, brg,
S7052	(Mg _{0.5} Fe _{0.5})SiO ₃ , 1 wt% Ni Cr V	420	2510 ± 100	liq, brg, mw, sti

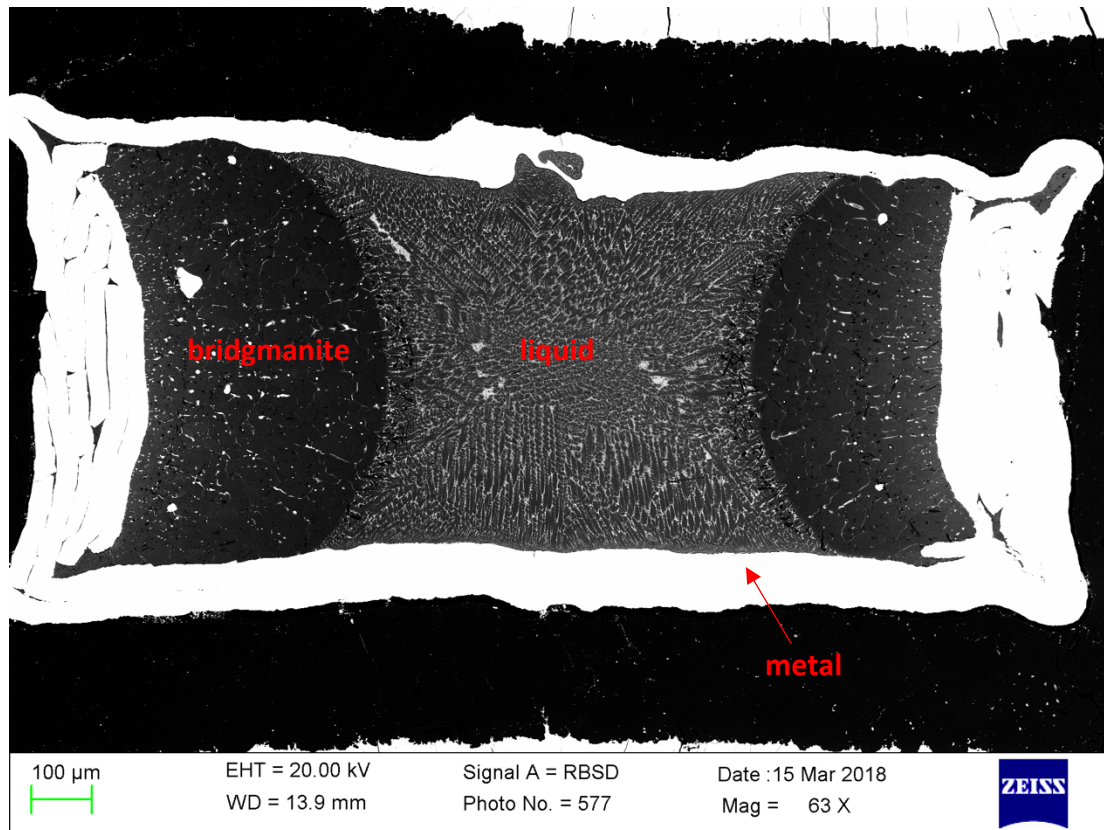


Figure 3.3: Backscattered image showing quenched silicate liquid texture coexisting with solid bridgmanite at 24 GPa and ~2580 K for the starting composition $(\text{Mg}_{0.80}\text{Fe}_{0.20})\text{SiO}_3$. Brighter sample area represent quenched liquid enriched in FeO relative to the darker coexisting. The rhenium of the capsule shows as the bright rim surrounding the sample.

Quantitative measurements of chemical compositions are conducted with the Jeol JXA 8200 electron microprobe at acceleration voltage 15-20 kV, with 1 μm diameter focused beam for measuring the mineral phases and 30 μm beam diameter used for the quenched liquid along the phase boundary. For each element, the counting times are 20 s on the peak and 10 s on the background. The standards used for calibrating elements are forsterite for Mg, enstatite for Si, and the metals for Fe, Ni, Cr, V, Re.

3.1.5.1 Scanning Electron Microscope

Scanning electron microscopy (SEM) is employed in this study for the purpose of imaging the surface of the polished sample and semi-quantitatively determine the chemical compositions of the target area. A focused beam of electrons is generated from the thermionic gun and interacts with atoms within the sample at different depth. This process produces various signals collected by detectors which provide information of sample

topography and chemistry (Figure 3.4): Secondary electrons (SE), backscattered electrons (BSE) and characteristic X-rays.

Secondary electrons are excited only within a few nanometers below the sample surface (~ 5 nm) due to their low energy (< 50 eV) and collected by an Everhart-Thornley detector (Everhart and Thornley 1960), with a larger number of SE leading to a brighter signal. The number of SE is controlled by the incident angle between the primary beam and the sample surface. When the angle increases, more secondary electrons are emitted due to the increase of the interaction volume. Therefore, a steeper sample surface appears brighter than a flat area, providing information on surface topography.

Backscattered electrons contain higher energy (> 50 eV) and originate from the elastic scattering of electrons in the primary beam with sample atoms over a larger portion of the sample volume (~100 nm below its surface). As heavy elements backscatter more electrons than lighter ones, a BSE image maps chemical composition, with Fe-bearing portions of the sample brighter than lower iron content phases, the pure metal shows the highest brightness (Figure 3.3). Unlike SE, backscattered electrons are detected from different angles above the sample with the BSE Centaurus detector in BGI.

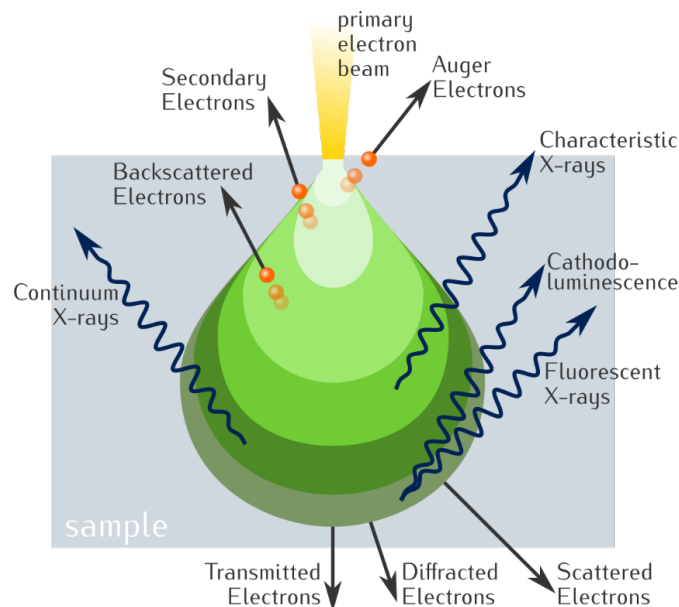


Figure 3.4: Interaction of the electron beam with matter in a scanning electron microscope. Depending on their energy, the electrons interact with atoms in the sample to generate secondary electrons, backscattered electrons, Auger electrons, cathodo-luminescence and various X-rays. Other electrons are either transmitted, diffracted or scattered. Image adopted from Wikipedia 21/06/2021.

When electrons in the inner shells of atoms in the sample are excited, electrons in the outer shells will fill this hole, leading to an X-ray emission (Figure 3.5) that is characteristic for an atom type. Therefore, chemical composition can be determined in a semi-quantitative way from the collected energy-dispersive X-ray spectrum (EDS) (Figure 3.6). However, more precise composition measurements are performed in the electron microprobe.

3.1.5.2 Electron Probe Micro Analysis

With electron probe microanalysis (EPMA) we obtain the chemical compositions of phases in the sample. An electron beam is generated from the tungsten filament (or lanthanum hexaboride crystal) and fired towards the sample surface. Similar to the SEM, where the electron beam interacts with electrons in the innermost shell of atoms in the sample, some of the electrons in the beam scatter with electrons in the deep atomic shells and create an electron hole. To restore the ground state of the atom, the hole must be filled by an electron either from a higher-energy shell or low-energy unbound electrons. The transfer of electron from one shell to another is accompanied by energy difference and produces a photon. Since different atoms have unique electronic structure, the emitted X-rays carry the energy and wavelength information of certain elements from the sample.

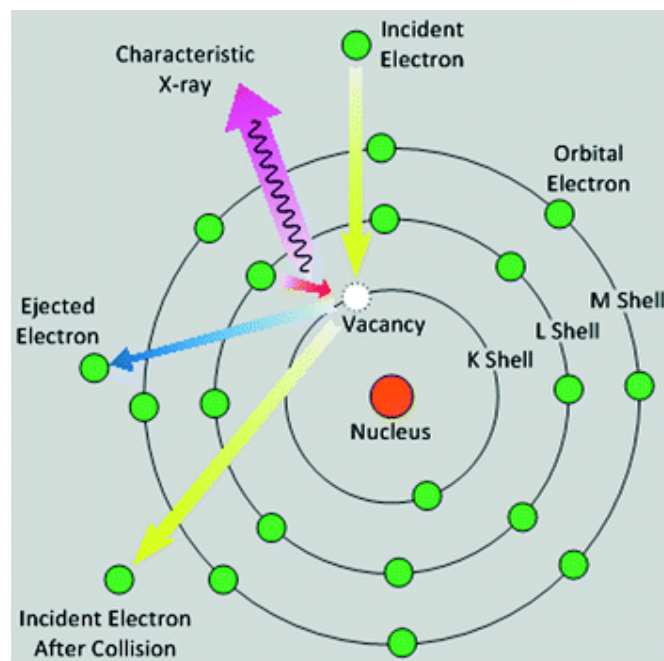


Figure 3.5: A schematic diagram showing an electron from the primary beam expelling a low-lying electron from an inner shell (K Shell) of an atom, creating a hole. The electron in the L shell fills this hole, and in the process, characteristic X-rays are emitted. (adopted from Sakamae, 2018)

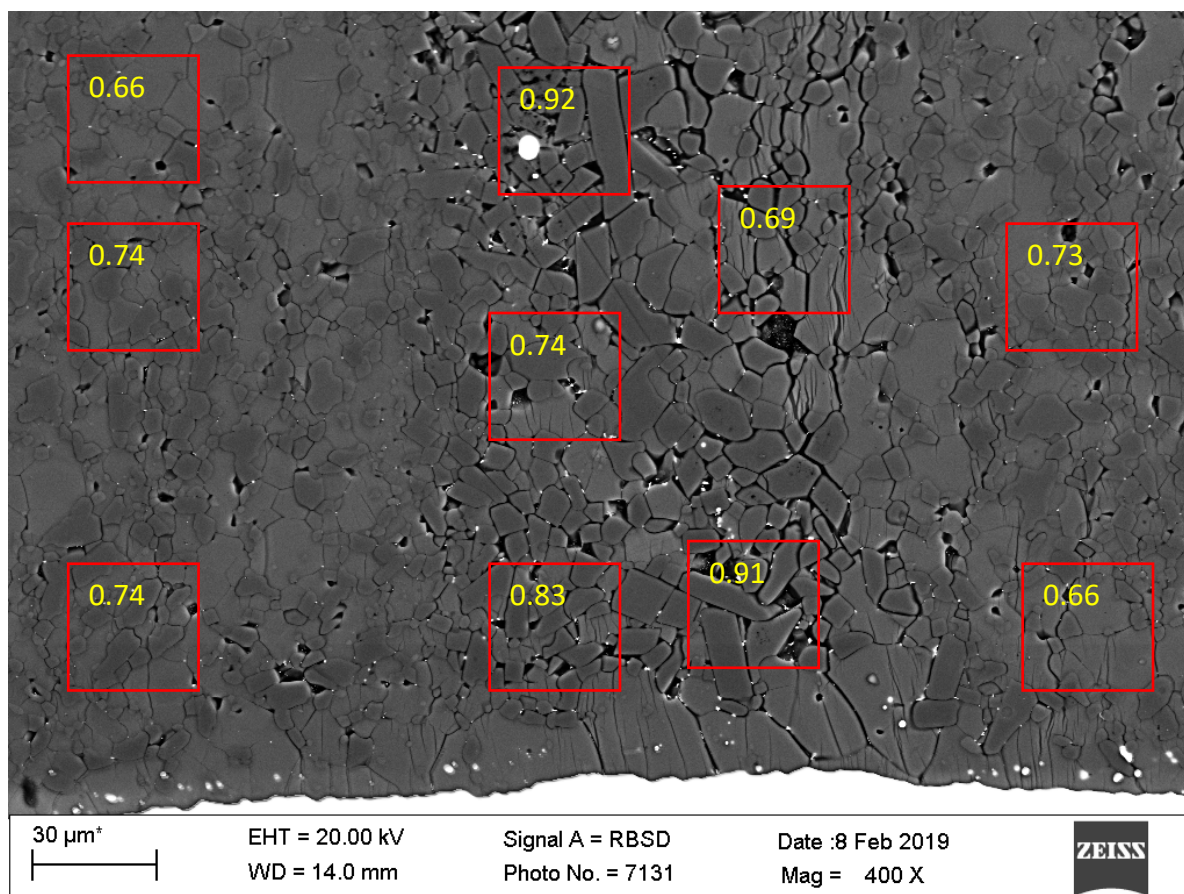


Figure 3.6: Backscattered image for an experiment with starting composition $Mg_{0.3}Si_{10.7}O_{1.7}$ recovered from 24 GPa and ~ 2650 K. The areas inside the red squares are analyzed in terms of the silica molar fraction $X(SiO_2)/(X(SiO_2)+X(MgO))$ using energy dispersive X-ray spectra.

The produced X-rays from the electron sample interactions are selected or counted by either wavelength-dispersive (WDS) or energy-dispersive X-ray spectroscopy (EDS). We use WDS, for which $n\lambda = 2d\sin\theta$ (Bragg's law) holds; n is the diffraction order, λ is the diffracted X-ray wavelength, d is the spacing between atomic planes, and θ represents the angle between diffracted X-rays and the atomic planes. As a result, the emitted X-ray beams with different wavelength (corresponding to different elements) are measured by the detectors. Quantitative information of each element is acquired by comparing the intensity of characteristic X-ray lines with the standard material of similar composition. The limitation for EPMA is that it is difficult to detect light elements such as hydrogen, due to their low atomic number which is difficult to produce characteristic X-rays.

3.2 Atomistic simulation

3.2.1 Density functional theory and molecular dynamics

Condensed matter (solids or liquids) consists of nuclei and electrons. Its macroscopic and microscopic properties arise from interactions between them. In quantum mechanics, the de Broglie hypothesis states that matter not only has classical particle property but also wave character. This leads to the formulation of a wave function $\Psi(t)$ of the system considered, with its evolution governed by the Schrödinger equation: $i\hbar \frac{d}{dt} |\Psi(t)\rangle = \hat{H} |\Psi(t)\rangle$, in which \hbar is the reduced Planck constant and \hat{H} is the Hamilton operator. Its time-independent form is $\hat{H} |\Psi\rangle = E |\Psi\rangle$, where E is the energy of the system.

Due to the Born Oppenheimer approximation, the calculation of the electronic Hamiltonian can be performed under the condition of fixed nuclei positions (Born and Oppenheimer, 1927): It allows for the separation of ionic (E_{ion}) and electronic energy terms (E_{el}) of the system, $E_{tot} = E_{ion} + E_{el}$. The task of searching for the ground state energy for E_{el} is computationally feasible through Hohenberg-Kohn density functional theory (DFT) (Hohenberg and Kohn, 1964) that separates

$$E_{el}[n] = E_{HK}[n] + \int V_{ext}(r)n(r)dr, \quad (3.1)$$

where $E_{HK}[n]$ is the Hohenberg-Kohn energy in the systems which is a functional of electron density n , and $V_{ext}(r)$ represents the external potential, caused by the arrangements of the ions in the system. The second theorem of Hohenberg and Kohn (Hohenberg and Kohn, 1964) establishes the equivalency of the ground state electron density n_0 and the lowest energy in the system.

Following the Hohenberg-Kohn definition of energy, the electronic exchange and correlation (xc) contribution to $E_{HK}[n]$ – representing many-body interactions – can be approximated mathematically by employing the chemical potential of the uniform electron gas and be used in treating the inhomogeneous system for electron i with wavefunction $\psi_i(r)$ and single particle eigenvalue (energy) ϵ_i (Kohn and Sham, 1965):

$$\left\{ -\frac{1}{2} \nabla^2 + [\varphi(r) + \mu_{xc}[n(r)]] \right\} \psi_i(r) = \epsilon_i \psi_i(r). \quad (3.2)$$

The first term on the left-hand side of the Kohn-Sham (KS) equation is the kinetic energy, the second term represents the sum of electrostatic interaction between electron with nuclei and electron with electron, and the third term is the exchange correlation energy. The complete

system is described by a set of N KS equations, and ground state electron density corresponds to the minimum of the total energy ($E_{el} = \sum_{i=1}^N f_i \epsilon_i$), where f_i represents an occupation number of states i .

In Newtonian mechanics the particle (mass m) path (position with time) $x(t)$ is determined by $F(x, t) = m \cdot a$, where a represents the acceleration, and the force F acting on a particle is the negative derivative of potential energy with respect to position. The Hellmann-Feynman forces computed within quantum mechanics provide a link between this classical definition of the force on an ion $-\vec{F}_I$ and the average of the derivative of Hamiltonian with respect to the same nuclear positions $\nabla_I H(\vec{R})$ (Feynman 1939):

$$-\vec{F}_I = \nabla_I \langle \Psi_0(\vec{R}) | H(\vec{R}) | \Psi_0(\vec{R}) \rangle = \langle \Psi_0(\vec{R}) | \nabla_I H(\vec{R}) | \Psi_0(\vec{R}) \rangle, \quad (3.3)$$

where $\Psi_0(\vec{R})$ is the many-body wave function which depends on the nuclear positions \vec{R} . In molecular dynamics (MD), the movement of atoms within a structure is calculated by solving the equations of motion once the Hellmann-Feynman force from the electrons acting on the atoms is determined. Computer simulation of atomic system can ideally be used to predict physical properties and provide insight when interpreting macroscopic phenomena (Allen and Tildesley, 1987).

Investigating the time evolution of a system, molecular dynamics offers the connection between atomic scale phenomena and physical properties via statistical mechanics. The ergodic hypothesis states that the time average approximates the ensemble average (Palmer, 1982) which – in turn – provides the definition of a physical property within the thermodynamic concepts of Adam Gibbs (Allen and Tildesley, 1987). Different choices of ensemble (e.g., N - V - E , N - V - T , in which N represents the number of particles in the system, V is the total volume and E is the internal energy of the system) lead to different statistical averages in the MD simulations (Allen and Tildesley, 1987).

3.2.2 Ab initio simulations using the Vienna Ab initio Simulation Package

From Bloch's theorem for periodic systems (Kittel et al., 1996), the solution of Schrödinger's equation can be separated into two parts,

$$\psi(r) = e^{ik \cdot r} u(r), \quad (3.4)$$

where ψ is the wavefunction, k is the wave vector, $e^{ik \cdot r}$ a plane wave, and $u(r)$ a periodic function. This naturally leads to a planewave representation of the electronic wavefunctions. Periodic boundary conditions are usually used in combination with plane waves in ab initio calculations, which make use of periodicity to create an infinite system from the unit cell in a crystal or supercells in aperiodic systems (Makov and Payne, 1995). In this study, we use the supercell approach to investigate liquids and glasses system in atomic scale modeling.

The projector augmented wave (PAW) method (Blöchl 1994) solves for the all-electron wavefunction by combining advantages from the pseudopotential and linear augmented plane wave methods. It separates the wavefunction into two parts: (i) within the augmentation region, the all electron wavefunction can be transformed from the pseudo-wavefunction, and the transformation is specified by three quantities: all-electron partial wavefunction, pseudo partial wavefunction and a projector function; (ii) outside the augmentation region, the pseudo-wavefunction equals the all-electron wavefunction.

Employing a planewave basis set and the PAW method (Kresse and Joubert, 1999), the Vienna Ab initio Simulation Package (VASP) (Kresse and Furthmüller 1996) offers an efficient iterative scheme in which the KS equations (equation 3.2) are solved iteratively to find the electronic ground state charge density n_0 .

3.2.3 Simulation setup

In order to explore the structure of Mg_2SiO_4 and MgSiO_3 liquids and glasses we perform DFT-MD simulations in the canonical $N-V-T$ ensemble using VASP. Cubic simulation cells contain 210 atoms (i.e., 30 formula units of Mg_2SiO_4 and 42 formula units of MgSiO_3), atomic coordinates are updated using a time step of 1 fs, and T is controlled by a Nosé thermostat (Nosé, 1984). At each time step, the electron density is computed with the projector augmented wave method (Blöchl, 1994) using Mg, Si and O potentials with s2p6, s2p2 and s2p4 electronic valence configurations, respectively. Electronic exchange and correlation are approximated by the generalized gradient (GGA) functional of Perdew, Burke and Ernzerhof (Perdew et al., 2008), and we expand plane waves to an energy cutoff of 600 eV. The Brillouin zone is sampled at the zone center.

For the DFT-MD simulations on Fe-bearing forsterite liquids we also use the $N-V-T$ canonical ensemble within the VASP package, but account for spin polarization in the electronic self-consistency cycle to compute the charge density. For Fe we use a PAW potential file with 3pd7s1 valence configuration. Following Ramo and Stixrude (2014) and Karki et al. (2018) we apply the on-site corrected GGA + U approach in its simplified rotationally invariant formulation (Dudarev et al., 1998) to describe electronic with an effective value of $U=3.0$ eV. The plane wave cutoff is set at 1000 eV to account for the large charge gradients due to the localized electronic states, and the Brillouin zone is sampled at the Γ point. The cubic simulation cell contains a total 112 atoms, $14 \text{ Mg}_2\text{SiO}_4 + 2 \text{ Fe}_2\text{SiO}_4$, and we compare the same size of a pure forsterite cell to explore the difference in molar volume between FeO and MgO in an olivine liquid over a wide compression range at 3000 K.

3.2.4 Radial distribution functions

The partial radial distribution function (RDF) $g_{\alpha\beta}(r)$ describes the atomic structure of liquids and glasses (Figure 3.7). It is defined such that, when considering an atom of species α , the probability of finding an atom of species β in a spherical shell around it ($r, r+dr$) is $4\pi r^2 n_\beta g_{\alpha\beta}(r) dr$, where $n_\beta = X_\beta/V_{at}$ is the number density of species β with atomic fraction X_β , and V_{at} the volume per atom.

Here we evaluate $g_{\alpha\beta}(r)$ using the R.I.N.G.S. software package (Le Roux and Jund, 2010) and sum over the partial radial distribution functions to obtain the total RDF $g_{tot}(r)$,

$$g_{tot}(r) = \sum_{\alpha=1}^n \sum_{\beta=1}^n b_\alpha b_\beta c_\alpha c_\beta g_{\alpha\beta}(r), \quad (3.5)$$

where $c_\nu = N_\nu/N$ relates the number of atoms of type ν to the total number of atoms N in the simulation box, and the sum is taken over the n species in the system. $g_{\alpha\beta}(r)$ are weighted with b_ν , which represent the neutron or X-ray scattering lengths of species ν for comparison with experiments.

Based on the RDF, the coordination number of species β around α can be defined as:

$$C_{\alpha\beta} = 4\pi\rho_\beta \int_0^{r_{min}} r^2 g_{\alpha\beta}(r) dr, \quad (3.6)$$

where r_{min} is the first minimum peak location and ρ_β is the number density of species β .

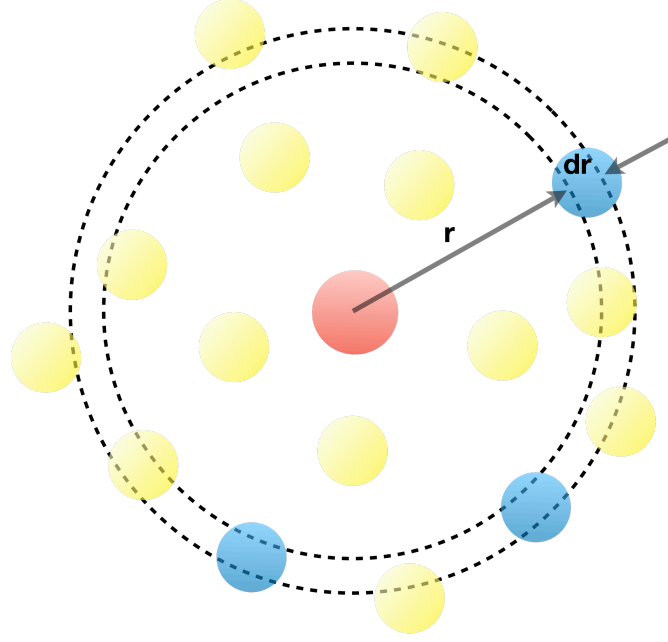


Figure 3.7: Illustration of the partial radial distribution function $g_{\alpha\beta}(r)$. The reference atom of type α is shown in red, atoms of type β in a spherical shell within a radius r and $r+dr$ are shown in blue. Yellow atoms are of different type (possibly including more α), and β outside the spherical shell, and do not contribute to $g_{\alpha\beta}(r)$. To obtain $g_{\alpha\beta}(r)$ for the structure, this procedure is repeated for all atoms of type α in the cell.

3.2.5 X-ray and Neutron structure factors

Experiments on liquids and glass do not have access to the real-space distribution of atoms, represented by the RDF, but rely on the total structure factor $S_{tot}(q)$ in reciprocal space. $S_{tot}(q)$ can be computed from structures along the MD trajectory via the partial structure factors $S_{\alpha\beta}(q)$ which are related to $g_{\alpha\beta}(r)$. Different formulations to compute $S_{\alpha\beta}(q)$ exist (Dove et al., 2002), and we use the formalism by Ashcroft and Langreth (1967) that involves the Fourier transformation of $g_{\alpha\beta}(r)$,

$$S_{\alpha\beta}^{AL}(q) = \delta_{\alpha\beta} + 4\pi\rho(c_{\alpha}c_{\beta})^{1/2} \int_0^{\infty} dr r^2 \frac{\sin(qr)}{qr} (g_{\alpha\beta}(r) - 1). \quad (3.7)$$

Here, $\delta_{\alpha\beta}$ is the Kronecker delta. The total X-ray structure factor is then calculated (Gazzillo et al., 1999) as,

$$S_{tot}^{XRD}(q) = \frac{\sum_{\alpha=1}^p \sum_{\beta=1}^p f_{\alpha}(q) f_{\beta}(q) \sqrt{c_{\alpha}c_{\beta}} [S_{\alpha\beta}^{AL}(q) + 1]}{\sum_{\alpha=1}^p c_{\alpha} f_{\alpha}^2(q)}, \quad (3.8)$$

where $f_{\alpha}(q)$ is the q -dependent X-ray scattering form factor of species α (Brown et al., 2006); to obtain total neutron structure factor, the X-ray form factors are replaced by the coherent (q -independent) neutron scattering lengths (Sears, 1992).

4. Thermodynamics for lower mantle melting

Multi-anvil experiments can establish melting temperatures and phase relations at a certain pressure, but thermodynamic modeling is required to extrapolate them beyond the specific conditions of the experiment, both in compositions and pressure. The complete thermodynamic description of a multi-component system requires the determination of Gibbs energy for well-chosen solid and liquid endmembers and a formulation of their mixing behavior.

4.1 Thermodynamic description of solids

The description of Gibbs energy of pure solid phase G requires the information at reference condition, G_0 , and the caloric (isobaric heating) and elastic (isothermal compression) contributions. Many different model formulations are developed to approximate the caloric or elastic part of energy: Caloric – Murnaghan, Birch-Murnaghan – Mie-Grüneisen and Caloric – Modified-Tait (Fabrichnaya et al., 2004; Stixrude and Lithgow-Bertelloni, 2005; Holland et al., 2013).

Here, the energetics of the solid phases, MgO periclase, FeO wüstite, MgSiO₃ bridgmanite, FeSiO₃ bridgmanite and SiO₂ stishovite are formulated by the Birch-Murnaghan –Mie-Grüneisen model (e.g., Chust et al., 2017; de Koker and Stixrude 2009; Stixrude and Lithgow-Bertelloni, 2005). Helmholtz energy is separated into a term $F_0(V_0, T_0)$ at reference V_0 and T_0 , an isothermal compression (elastic) term $F_{\text{elast}}(V, T_0)$ and a thermal contribution $F_{\text{th}}(V, T)$,

$$F(V, T) = F_0(V_0, T_0) + F_{\text{elast}}(V, T_0) + F_{\text{th}}(V, T) \quad (4.1)$$

F_{elast} is described by a Eulerian finite strain f expansion of third order and presented in terms of physical parameters

$$F_{\text{elast}}(V, T_0) = -\frac{9}{2}K_0V_0[f^2 + (K'_0 - 4)f^3], \quad (4.2)$$

where K_0 is the bulk modulus at V_0 (zero P) and K'_0 its P derivative, also taken at V_0 , and

$$f = \frac{1}{2} \left[\left(\frac{V_0}{V} \right)^{\frac{2}{3}} - 1 \right]. \quad (4.3)$$

The thermal contribution is modeled in the Mie-Grüneisen approximation, with a parameterization of the Grüneisen parameter γ as

$$\gamma = \gamma_0 \left(\frac{V}{V_0} \right)^{q_0}, \quad (4.4)$$

with γ_0 and q_0 material constants. Using the parameterization of equation 4.4, $F_{\text{th}}(V, T)$ becomes

$$F_{\text{th}}(V, T) = -S_0(T - T_0) - \left[T \ln \frac{T}{T_0} - (T - T_0) \right] - \frac{C_{V0}\gamma_0^{q_0}}{q_0} (T - T_0)(V^{q_0} - V_0^{q_0}). \quad (4.5)$$

Entropy at the reference condition S_0 and heat capacity C_{V0} are also assumed constant. We use the BurnMan toolkit (Cottaar et al., 2014) (Section 4.9) to compute the thermodynamic properties for the solids.

4.2 Thermodynamic description of liquids

Similar to the solid, the Gibbs energy of a liquid can be expressed by the sum of a T -dependent ($G_{1 \text{ bar}, T}$) and P -dependent contribution ($\int_{1 \text{ bar}}^P V_T dP$). Komabayashi (2014) describes the first term using polynomial function while Belmonte et al. (2017) define this term by giving the enthalpy of formation at 298.15 K (H_{f298}^0), standard state entropy (S_{298}^0) and isobaric heat capacity C_P . The former study expresses the $V - P$ integral using the Vinet equation of state, the latter one employs the 3rd order Birch-Murnaghan isothermal equation of state; other choices include the Tait equation of state (Chorażewski et al., 2017). Different from these more traditional ad-hoc approaches, de Koker and Stixrude (2009) construct a full thermodynamic potential in a self-consistent way. They describe the Helmholtz energy by an ideal gas and excess part, from which all other thermodynamic information can be obtained in an analytical form.

For the thermodynamic description of endmember liquids MgO, FeO and SiO₂ we follow the model of de Koker and Stixrude (2009) that separates contributions to Helmholtz energy $F(V, T)$ into an ideal gas F_{ig} and excess term F_{xs} :

$$F(V, T) = F_{\text{ig}}(V, T) + F_{\text{xs}}(V, T). \quad (4.6)$$

The former is computed analytically (de Koker and Stixrude, 2009; 2010),

$$F_{\text{ig}} = \sum_M N_M F_{\text{ig}M} + k_B N_A T \sum_M N_M \ln X_M, \quad (4.7)$$

where the $F_{\text{ig}M}$ term is the ideal gas energy, N_M represents number of atoms of type M, k_B is the Boltzmann constant, N_A is Avogadro's number and X_M is the molar fraction of atom type M. F_{xs} is expanded in a series of Eulerian finite strain f (equation 4.3) and a reduced temperature θ ,

$$\theta = \left[\left(\frac{T}{T_0} \right)^m - 1 \right], \quad (4.8)$$

as

$$F_{\text{xs}}(V, T) = \sum_{i=0}^{\mathcal{O}_f} \sum_{j=0}^{\mathcal{O}_\theta} \frac{a_{ij}}{i!j!} f^i \theta^j. \quad (4.9)$$

V_0 is the equilibrium volume and T_0 a reference temperature, with the exponent in equation 4.7 (m) taken as a fit parameter. \mathcal{O}_f and \mathcal{O}_θ are the expansion orders in terms of V and T , respectively, with the additional condition that $i + j < \mathcal{O}_f + \mathcal{O}_\theta$. By taking derivatives of equation 4.9 with respect to V and T , expansion coefficients a_{ij} can be related to the excess contributions of combinations of thermodynamic properties (de Koker et al., 2009), e.g.,

$$a_{10} = 3 V_0 P_{\text{xs}0} \quad \text{or} \quad a_{01} = -\frac{1}{m} T_0 S_{\text{xs}0}.$$

For the consideration of an isothermal compression curve computed by molecular dynamics we apply the Tait equation of state (Hayward, 1967),

$$P = \frac{1}{b} \left(\left[\frac{(V_P/V_0)^{a-1}}{a} \right]^{-1/c} - 1 \right), \quad (4.10)$$

where V_0 is the reference volume, and parameters a , b and c are defined by the bulk modulus and its derivative. More details can be found in Angel et al. (2014) which also describes the EosFit7c program used for fitting.

4.3 Thermodynamics of mixing

Along a compositional join with solid solution behavior, the Gibbs energy of mixing (G_{mix}) is the sum of ideal part (G_{ideal}) and excess part (G_{excess}),

$$G_{\text{mix}} = G_{\text{ideal}} + G_{\text{excess}}. \quad (4.11)$$

Based on the elementary theory, the ideal part is described as,

$$G_{\text{ideal}} = RT \sum_{i=1}^n X_i \ln X_i, \quad (4.12)$$

where X_i is the mole fraction of liquid component i , R is the ideal gas constant, and T is the temperature. The excess Gibbs energy term is described using the Margules regular solution model (Ghiorso et al., 1983),

$$G_{\text{excess}} = \frac{1}{2} \sum_{i=1}^n \sum_{j=1}^n W_{ij} X_i X_j, \quad (4.13)$$

where W_{ij} is the interaction parameter; if $W_{ij} = W_{ji}$, the model is symmetric.

With the concept of activity coefficient γ_i for component i , the partial molar excess Gibbs energy is

$$RT \ln \gamma_i = \sum_{j=1}^n W_{ij} X_j - \frac{1}{2} \sum_{j=1}^n \sum_{k=1}^n W_{jk} X_j X_k. \quad (4.14)$$

The Margules parameter can be formulated as a function of temperature and pressure, in this study since our experiments are performed at single pressure, therefore only the temperature dependent is considered.

4.4 Prior thermodynamic description of the MgO-MgSiO₃ system at 24GPa

Liebske and Frost (2012) built a thermodynamic model in the MgO-MgSiO₃ system at 24 GPa, with MgO periclase and MgSiO₃ bridgmanite as endmember. The eutectic position in this system is constrained by two equations,

$$\mu_{\text{MgSiO}_3}^{\text{solid}} = \mu_{\text{MgSiO}_3}^{\text{liquid}}, \quad (4.15)$$

$$\mu_{\text{MgO}}^{\text{solid}} = \mu_{\text{MgO}}^{\text{liquid}}, \quad (4.16)$$

where the chemical potential of the solid (μ^{solid}) equals that of the liquid (μ^{liquid}). As pure phases, μ^{solid} equal the standard state partial molar Gibbs energy. The chemical potential in the liquid is the sum of standard state and an activity part,

$$\mu_{\text{MgO}}^{\text{liquid}} = \mu_{\text{MgO}}^{0,\text{liquid}} + R \cdot T \cdot \ln(a_{\text{MgO}}), \quad (4.17)$$

$$\mu_{\text{MgSiO}_3}^{\text{liquid}} = \mu_{\text{MgSiO}_3}^{0,\text{liquid}} + R \cdot T \cdot \ln(a_{\text{MgSiO}_3}), \quad (4.18)$$

The activity a of the liquid component is the product of its activity coefficient and mole fraction, e.g.,

$$a_{\text{MgSiO}_3} = X_{\text{MgSiO}_3} \cdot \gamma_{\text{MgSiO}_3}, \quad (4.19)$$

and the activity coefficient γ is described by the Margules model,

$$R \cdot T \cdot \ln(\gamma_{\text{MgO}}) = W_{\text{MgO-MgSiO}_3} (1 - X_{\text{MgO}})^2, \quad (4.20)$$

$$R \cdot T \cdot \ln(\gamma_{\text{MgSiO}_3}) = W_{\text{MgO-MgSiO}_3} (1 - X_{\text{MgSiO}_3})^2. \quad (4.21)$$

4.5 Thermodynamic description in the MgO-SiO₂ system

We extend the thermodynamic model for melting phase relations just described to the MgO-SiO₂ system by using the location of the two eutectic points (Figure 2.1) as constraints. For a closed formulation with a minimum number of parameters, we represent all liquids through the oxide components MgO and SiO₂, and use MgO periclase, MgSiO₃ bridgmanite and SiO₂ stishovite as solid phases. At both eutectics,

$$\mu_{\text{MgSiO}_3}^{\text{solid}} = \mu_{\text{MgO}}^{\text{liquid}} + \mu_{\text{SiO}_2}^{\text{liquid}}, \quad (4.22)$$

and equation 4.16 or

$$\mu_{\text{SiO}_2}^{\text{solid}} = \mu_{\text{SiO}_2}^{\text{liquid}}, \quad (4.23)$$

respectively. The chemical potentials of the liquids can be expanded into a standard state potential $\mu_{\text{MgO}}^{0,\text{liquid}}$ for MgO ($\mu_{\text{SiO}_2}^{0,\text{liquid}}$ for SiO₂), and an activity term as in equations 4.17 and 4.18 (the former for MgO continues to hold):

$$\mu_{\text{SiO}_2}^{\text{liquid}} = \mu_{\text{SiO}_2}^{0,\text{liquid}} + R \cdot T \cdot \ln(X_{\text{SiO}_2} \gamma_{\text{SiO}_2}), \quad (4.24)$$

$$\mu_{\text{MgSiO}_3}^{\text{liquid}} = \mu_{\text{MgO}}^{0,\text{liquid}} + R \cdot T \cdot \ln(X_{\text{MgO}} \gamma_{\text{MgO}}) + \mu_{\text{SiO}_2}^{0,\text{liquid}} + R \cdot T \cdot \ln(X_{\text{SiO}_2} \gamma_{\text{SiO}_2}). \quad (4.25)$$

Equations 4.20 and 4.21 are replaced by

$$R \cdot T \cdot \ln(\gamma_{\text{MgO}}) = W_{\text{MgO-SiO}_2} (1 - X_{\text{MgO}})^2 \quad (4.26)$$

and

$$R \cdot T \cdot \ln(\gamma_{\text{SiO}_2}) = W_{\text{MgO-SiO}_2} (1 - X_{\text{SiO}_2})^2, \quad (4.27)$$

with the Margules interaction parameter $W_{\text{MgO-SiO}_2}$. In our work, we formulate a T -dependence of $W_{\text{MgO-SiO}_2} = W_H - W_S T$, but with experiments performed only at 24 GPa, a P dependent model cannot be fit. More complex solution models are not sufficiently constrained by the number of data collected.

The standard state chemical potentials for the liquid components ($\mu_{\text{MgO}}^{0,\text{liquid}}$ and $\mu_{\text{SiO}_2}^{0,\text{liquid}}$) are evaluated based on the thermodynamic model by de Koker et al. (2013); $\mu_{\text{MgO}}^{\text{solid}}$, $\mu_{\text{MgSiO}_3}^{\text{solid}}$ and $\mu_{\text{SiO}_2}^{\text{solid}}$ are based on the Birch-Murnaghan – Mie-Grüneisen model (e.g., Chust et al., 2017) for MgO periclase, SiO₂ stishovite and MgSiO₃ bridgmanite used in de Koker et al. (2013).

4.6 Thermodynamic description in the FeO-MgO-SiO₂ system

When adding FeO chemical component, the five endmember thermodynamic parameters in the MgO-SiO₂ system are kept the same for the FeO-MgO-SiO₂ systems. Another three new endmembers are: FeSiO₃ (bridgmanite), FeO (wüstite) and FeO (liquid). The thermodynamic parameters for FeSiO₃ bridgmanite are taken from Stixrude and Lithgow-Bertelloni (2011). The wüstite equation of state parameters are adopted from Fischer et al. (2011), which performs volume measurements of FeO solid up to 156 GPa and 3100 K (more details are listed in Section 6.2).

The liquid FeO thermodynamic parameters can be constrained from the experimental melting curves which are subject to ongoing debate (Frost et al., 2010; Komabayashi 2014; Boukaré et al., 2015). We fit the melting curve through Lindsley, (1966) and Fu et al. (2018) using the liquid model described in Section 4.2, as it covers the P -range 0–120 GPa and is consistent with a wide range of experimental datasets. Further details are in Section 6.3.

In the FeO-MgO-SiO₂ system, the coexistence of solid and liquid phases is described by a set of five equilibria (equations 4.16, 4.22 and 4.23) and

$$\mu_{\text{FeO}}^{\text{solid}} = \mu_{\text{FeO}}^{\text{liquid}}, \quad (4.28)$$

$$\mu_{\text{FeSiO}_3}^{\text{solid}} = \mu_{\text{FeO}}^{\text{liquid}} + \mu_{\text{SiO}_2}^{\text{liquid}}. \quad (4.29)$$

The fact that MgO and FeO form solid solutions in the oxide (Mg,Fe)O and (Mg,Fe)SiO₃ silicate complicates the formulation of the thermodynamics, and we consider ideal mixing in our formulation, consistent with prior work by Boukaré et al. (2015), Fu et al. (2018) and Miyazaki and Korenaga (2019) which leads to the representation for μ^{solid} as

$$\mu_{\text{MgO}}^{\text{solid}} = \mu_{\text{MgO}}^{0,\text{solid}} + R \cdot T \cdot \ln (X_{\text{MgO}}^{\text{solid}}), \quad (4.30)$$

$$\mu_{\text{FeO}}^{\text{solid}} = \mu_{\text{FeO}}^{0,\text{solid}} + R \cdot T \cdot \ln (X_{\text{FeO}}^{\text{solid}}), \quad (4.31)$$

$$\mu_{\text{MgSiO}_3}^{\text{solid}} = \mu_{\text{MgSiO}_3}^{0,\text{solid}} + R \cdot T \cdot \ln (X_{\text{MgSiO}_3}^{\text{solid}}), \quad (4.32)$$

$$\mu_{\text{FeSiO}_3}^{\text{solid}} = \mu_{\text{FeSiO}_3}^{0,\text{solid}} + R \cdot T \cdot \ln (X_{\text{FeSiO}_3}^{\text{solid}}), \quad (4.33)$$

where X_i^{solid} are the molar fractions of MgO and FeO in ferropericlase and bridgmanite. The chemical potential of stishovite is the same as its standard state (equation 4.23).

The chemical potentials of the liquid components remain the same for MgO and SiO₂ (equations 4.17 and 4.24); for FeO,

$$\mu_{\text{FeO}}^{\text{liquid}} = \mu_{\text{FeO}}^{0,\text{liquid}} + R \cdot T \cdot \ln (X_{\text{FeO}}^{\text{liquid}} \gamma_{\text{FeO}}). \quad (4.34)$$

The expressions for the activity coefficients are (Ghiorso et al., 1983):

$$R \cdot T \cdot \ln(\gamma_{\text{MgO}}) = (W_{\text{MgO-SiO}_2} \cdot (1 - X_{\text{MgO}}^{\text{liquid}}) - W_{\text{FeO-SiO}_2} \cdot X_{\text{FeO}}^{\text{liquid}}) \cdot X_{\text{SiO}_2}^{\text{liquid}}, \quad (4.35)$$

$$R \cdot T \cdot \ln(\gamma_{\text{FeO}}) = (W_{\text{FeO-SiO}_2} \cdot (1 - X_{\text{FeO}}^{\text{liquid}}) - W_{\text{MgO-SiO}_2} \cdot X_{\text{MgO}}^{\text{liquid}}) \cdot X_{\text{SiO}_2}^{\text{liquid}}, \quad (4.36)$$

$$R \cdot T \cdot \ln(\gamma_{\text{SiO}_2}) = (W_{\text{MgO-SiO}_2} \cdot X_{\text{MgO}}^{\text{liquid}} + W_{\text{FeO-SiO}_2} \cdot X_{\text{FeO}}^{\text{liquid}}) \cdot (X_{\text{MgO}}^{\text{liquid}} + X_{\text{FeO}}^{\text{liquid}}), \quad (4.37)$$

and $W_{\text{MgO-SiO}_2}$ and $W_{\text{FeO-SiO}_2}$ are T -dependent Margules interaction parameters:

$$W_{\text{MgO-SiO}_2} = W_{\text{MgO-SiO}_2}^0 - W_{\text{MgO-SiO}_2}^S \cdot T, \quad (4.38)$$

$$W_{\text{FeO-SiO}_2} = W_{\text{FeO-SiO}_2}^0 - W_{\text{FeO-SiO}_2}^S \cdot T, \quad (4.39)$$

as for the MgO-SiO₂ system.

4.7 Simple work flow of thermodynamic modelling

The general workflow of thermodynamic modelling in this study is summarized in Figure 4.1. The Margules mixing parameters, liquid FeO and SiO₂ endmember parameters are constrained from our experiments and literature data by solving the thermodynamic equations simultaneously with a Least Square Monte Carlo method (LSMC) or data fitting tools in python. The solid and liquid MgO data are based on database or previous literature work (De Koker and Stixrude, 2009; Cottaar et al., 2014). The forward modelling computes a wide range of chemical and physical properties from the updated thermodynamic parameters.

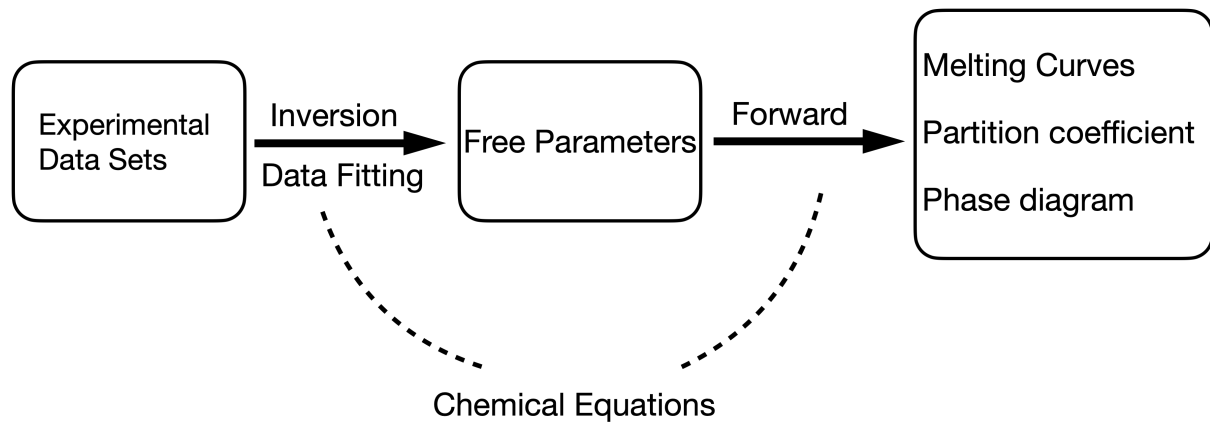


Figure 4.1: Simplified workflow of thermodynamic modelling in this study. The experimental data sets are the multi anvil melting experiments in the MgO-MgSiO₃ system by Liebske and Frost, (2012), the MgSiO₃-SiO₂ and FeO-MgO-SiO₂ system in our work, FeO melting curve by Frost et al., (2010). The free parameters are liquid SiO₂, FeO thermodynamic parameters as well as the mixing parameters. The computed melting curves include endmembers MgO, SiO₂, FeO, MgSiO₃ and FeSiO₃. Iron partitioning and melting phase relations in the FeO-MgO-SiO₂ system are also computed by solving the relevant chemical equations.

4.8 BurnMan package in python

The liquid parameters for the expansion of F_{xs} by de Koker et al. (2013) for silicate liquids at high P are tabulated in a database for the BurnMan thermoelastic toolkit (Cottaar et al., 2014), maintained at the Computational Infrastructure for Geodynamics (<https://geodynamics.org/cig/software/burnman/>) as class `dks_liquid`. The solid endmember parameters in the MgO-SiO₂ system are archived as class `dks_solid`. In our Monte Carlo inversion for the location of the eutectic in the MgSiO₃-SiO₂ subsystem and the melting curve

of SiO_2 , we optimize new values for the expansion parameters. The liquid FeO parameters are also fitted from melting curves within BurnMan.

BurnMan is an open source package written in Python. In which the SciPy library provides a number of powerful tools in scientific computing and becomes very popular in recent years (Virtanen et al., 2020). The algorithms in SciPy such as least square, fsolve are frequently employed in combination with the equation of states to solve for the free parameters in the thermodynamic model. Monte Carlo method (random sampling) is also included for computing the uncertainty of parameters.

The liquid SiO_2 free parameters are constrained with the `scipy.optimize.least_squares` algorithm, for example, which allows to search the optimized values within given initial upper and lower bounds. The least square routine runs 1000 times using Monte Carlo sampling of input experimental uncertainties.

5. Melting phase relations in the MgO-SiO₂ system under lower mantle pressure

Characterizing and modelling melting relations in the system MgO-SiO₂ at lower mantle pressures relies on the location of the eutectic points for MgO-MgSiO₃ and MgSiO₃-SiO₂ (Figure 2.1). While at an uppermost lower mantle pressure there is general consensus on the eutectic composition in the MgO-MgSiO₃ system, large discrepancies exist for MgSiO₃-SiO₂ from experiments in the diamond anvil cell, ab initio simulations and models built on them. In order to address this discrepancy, we perform multi-anvil press experiments at 24 GPa for Mg_{0.4}Si_{0.6}O_{1.6} and Mg_{0.3}Si_{0.7}O_{1.7} at temperatures of 2650 ± 100 K and 2750 ± 100 K (Table 3.1).

5.1 Experimental results

In the experiments for both compositions heated with 450 W ($T = 2650 \pm 100$ K) we find a crystalline matrix with well-developed triple junctions (similar to the right side of the sample in Figure 5.1a), showing that they are performed at sub-solidus conditions, consistent with the prediction by de Koker et al. (2013).

In the higher- T experiments ($T = 2750 \pm 100$ K) for Mg_{0.3}Si_{0.7}O_{1.7}, we observe a quench texture in the recovered sample coexisting with the solid (Figure 5.1a). Within the quench texture we observe small bridgmanite and stishovite grains (both a few μm in size), with a small amount of liquid between them, suggesting that we have just reached super-solidus T , tightly constraining the eutectic temperature (T_e), with our value in excellent agreement with the prediction by de Koker et al. (2013). In addition, some of the stishovite grains appear to have grown at the expense of the liquid during quench, as indicated by the lighter-colored rims. The amount of melt preserved in the sample is too small for it to be analyzed by EPMA.

For the Mg_{0.4}Si_{0.6}O_{1.6} sample heated with 470 W ($T = 2750 \pm 100$ K), by contrast, we observe a liquid quench texture, coexisting with acicular stishovite crystals, some of which reach lengths of 50 μm and widths of 30 μm , indicating a liquidus assemblage (Figure 5.1b). The identification of stishovite as the liquidus phase for $X_{\text{SiO}_2} = 0.6$ starting composition suggests that the liquid evolves towards a MgSiO₃-rich composition. Microprobe analysis of 32 spots in the quenched melt shows values in the range of $X_{\text{SiO}_2} = 0.49 - 0.60$, reflecting its

small-scale heterogeneity (Figure 5.1b), with an average of $X_{\text{SiO}_2} = 0.53 \pm 0.03$ (Figure 5.2) that accurately represents the bulk melt. As the melting experiment for $\text{Mg}_{0.3}\text{Si}_{0.7}\text{O}_{1.7}$ with virtually the same heating power suggests that we are very close to T_e , the liquid composition in the $\text{Mg}_{0.4}\text{Si}_{0.6}\text{O}_{1.6}$ experiment constrains the eutectic composition in the $\text{MgSiO}_3\text{-SiO}_2$ system. This is a significantly lower eutectic X_{SiO_2} -value at $P = 24 - 25$ GPa than calculated by de Koker et al. (2013) based on ab initio simulations with $X_{\text{SiO}_2} = 0.63$ (Figure 5.2) or

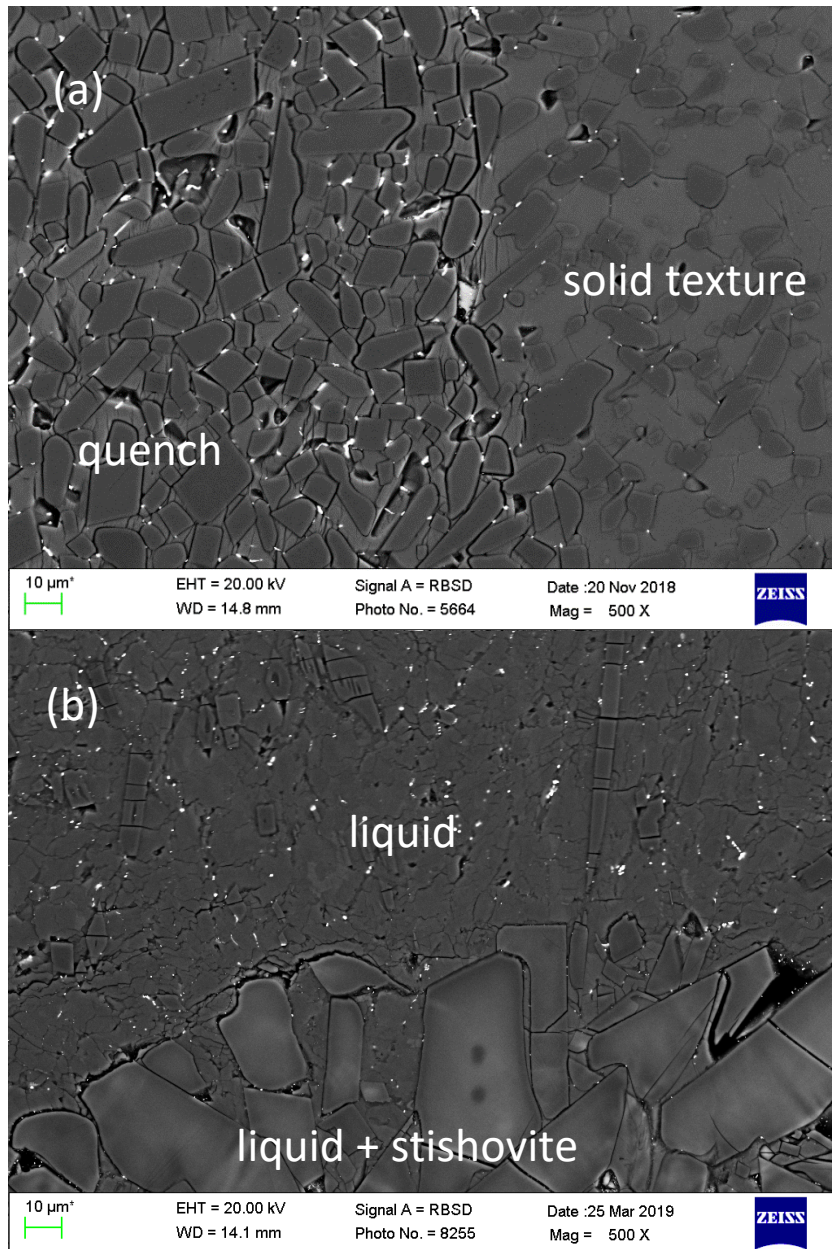


Figure 5.1: Scanning electron microprobe images showing (a) the low degree of partial melting in the experiment for $\text{Mg}_{0.3}\text{Si}_{0.7}\text{O}_{1.7}$ at $P = 24$ GPa and $T = 2750 \pm 100$ K, with quench texture on the left, and solid texture on the right, and (b) the experimental run product for $\text{Mg}_{0.4}\text{Si}_{0.6}\text{O}_{1.6}$ at $P = 24$ GPa and $T = 2750 \pm 100$ K where the sample is above the solidus; large stishovite crystals (bottom) coexist with a quenched liquid phase.

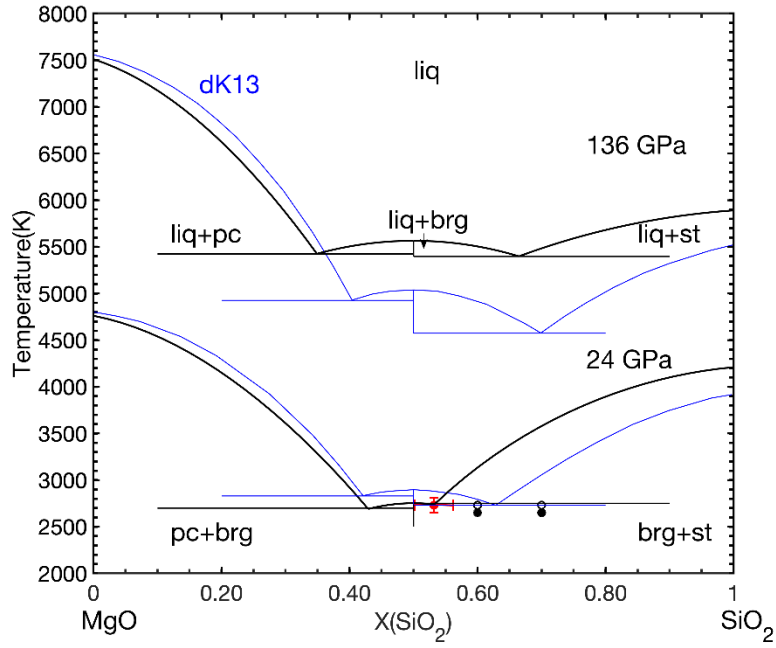


Figure 5.2: MgO-SiO₂ melting relations computed from our thermodynamic model at 24 GPa (bottom black graph), based on the experiments performed in the MgSiO₃-SiO₂ system, combined with the result for the MgO-MgSiO₃ system from Liebske and Frost (2012). The eutectic composition (red circle with error) is determined based on the experiment for Mg_{0.4}Si_{0.6}O_{1.6} at $P = 24$ GPa and $T = 2750 \pm 100$ K (open circle); starting compositions and temperature of the other three experiments (Table 3.1) are also shown, with the filled black circles for the experiments at $T = 2650 \pm 100$ K indicating that the experiments remained below the solidus. Melting relations at $P = 136$ GPa (top black graph) computed from our model. For comparison we include melting relations from the model of de Koker et al. (2013) (dK13, blue) both at $P = 24$ GPa and $P = 136$ GPa. Abbreviations: pc for periclase, brg for bridgmanite, st for stishovite and liq for liquid.

Table 5.1: Physical parameters for the Mie-Grüneisen Birch-Murnaghan thermodynamic model (equations 4.1, 4.2 and 4.5) as listed in the BurnMan database for the model of de Koker et al. (2013) (dK13) for SiO₂ stishovite, MgSiO₃ bridgmanite and MgO periclase; for stishovite, the first column reports our optimized values for F_0 and S_0 .

	SiO ₂ stishovite		MgSiO ₃ bridgmanite	MgO periclase
	This work	dK13	dK13	dK13
V_0 (cm ³ ·mol ⁻¹)	15.13		27.05	12.23
T_0 (K)	3000		3000	2000
F_0 (kJ·mol ⁻¹)	-2317 ± 3	-2275	-3355	-1165
K_0 (GPa)	181		167	110
K'_0	5.3		4.2	4.6
γ_0	1.39		1.89	1.41
q_0	1.33		1.49	0.63
S_0 (J·K ⁻¹ ·mol ⁻¹)	166 ± 1	167	338	120
C_{V0} (J·K ⁻¹ ·mol ⁻¹)	77.9		133.8	49.0

Table 5.2: Expansion coefficients a_{ij} for the excess Helmholtz energy (equation 4.9) in terms of finite strain f (equation 4.3) and a reduced temperature expression θ (equation 4.8, with the optimized exponent m) for SiO₂ and MgO liquids. Reference conditions of volume (V_0) and temperature (T_0), as well as the expansion orders (\mathcal{O}_f and \mathcal{O}_θ) in equation 4.9 are provided. The last two columns list the expansion coefficients from the model de Koker et al. (2013) (dK13) as given in the BurnMan database (Cottaar et al., 2014) for SiO₂ and MgO liquids, respectively. The first column lists our values obtained, with uncertainty. Three significant digits are reported for the fit parameters and S_{xs0} , P_{xs0} to 0.1 GPa.

	SiO ₂		MgO
	This work	dK13	dK13
V_0 (cm ³ ·mol ⁻¹)	29.8 ± 0.1	27.8	16.5
T_0 (K)	3000		
\mathcal{O}_f	5		3
\mathcal{O}_θ	2		
m	0.91		0.63
a_{00}	-2020 ± 5	-1950	-925
a_{10}	-227 ± 1	-227	-155
a_{01}	488 ± 10	455	261
a_{20}	4410 ± 30	2020	5320
a_{11}	-(218 ± 4)	-201	466
a_{02}	-(263 ± 6)	-217	-88.3
a_{30}	(36.3 ± 0.3) · 10 ³	48.4 · 10 ³	10.5 · 10 ³
a_{21}	401 ± 8	442	2000
a_{12}	-230 ± 5	73.1	50.7
a_{40}	-(655 ± 9) · 10 ³	-652 · 10 ³	-
a_{31}	(20.9 ± 0.4) · 10 ³	20.7 · 10 ³	-9.91 · 10 ³
a_{22}	585 ± 14	892	71.9
a_{50}	4.12 ± 0.08 · 10 ⁶	4.10 · 10 ⁶	-
a_{41}	-(137 ± 3) · 10 ³	-128 · 10 ³	-
a_{32}	-(52.5 ± 0.1) · 10 ³	-1230	-
S_{xs0} (J·mol ⁻¹ ·K ⁻¹)	-148	-138	-54.8
P_{xs0} (GPa)	-2.5	-2.7	-3.1

extrapolated from DAC experiments by Ozawa et al. (2018) with $X_{\text{SiO}_2} = 0.58$, but consistent with $X_{\text{SiO}_2} = 0.51$ modelled by Belmonte et al. (2017).

5.2 Determination of thermodynamic parameters

Using the SiO₂ liquid and stishovite parameters in the thermodynamic model of de Koker et al. (2013), we find that an effective interaction parameter of $-250 \text{ kJ/mol} \leq W_{\text{MgO-SiO}_2} \leq -200 \text{ kJ/mol}$ is required to reproduce the solidus temperatures of $T \sim 2750 \text{ K}$ for MgSiO₃-SiO₂ determined here. Nevertheless, we cannot find a satisfactory solution for $W_{\text{MgO-SiO}_2}$ that

Table 5.3: Thermodynamic properties of liquid SiO₂ at 0 GPa and 3000 K from the model developed here and the one implemented in BurnMan (Cottaar et al., 2014). Values from previous models by de Koker et al. (2009) (dK09) and Boukaré et al. (2015) (B15) are included for comparison. For dK09 we give values for the model with $\mathcal{O}_\theta = 2$ (equation 4.9).

Parameters	This Study	BurnMan	dK09	B15
V (cm ³ ·mol ⁻¹)	29.8	27.8	27.2	26.2
K_T (GPa)	14.6	6.2	7.1	16.2
K'_T	7.25	14.9	17.1	-
α (10 ⁻⁵ K ⁻¹)	1.2	3.9	12.1	4.7
S (J·mol ⁻¹ ·K ⁻¹)	198	206	223	-
C_P (J·mol ⁻¹ ·K ⁻¹)	130	116	137	137
γ	0.04	0.06	0.18	-

describes $X_{\text{SiO}_2} = 0.53 \pm 0.03$ for the eutectic adequately. This is not surprising considering that in the model of de Koker et al. (2013) liquidus T decreases rapidly from the high melting temperature (T_m) of stishovite with MgO content; We therefore consider modifications in the coefficients for the thermodynamic description of liquid SiO₂ in the model of de Koker et al. (2013) (Tables 5.2 and 5.3). In order to reasonably match T_m of SiO₂, we also consider changes in the thermodynamic description for stishovite which we restrict to reference energy and entropy (Table 5.1). For completeness, the thermodynamic parameters of MgO liquid are also provided in Table 5.4.

Rather than optimizing the thermodynamic parameters for SiO₂ liquid and stishovite separately from the Margules parameter $W_{\text{MgO-SiO}_2}$, we jointly determine them by using a least square Monte Carlo minimization. With only two constraints (the eutectics), the problem is underdetermined, and initial guesses and bounds for the parameters are important. We make choices that are guided by physical insight into (i) the thermodynamic parameters of SiO₂ liquid, (ii) the melting curve of stishovite, (iii) the range of values for the effective

Table 5.4: Thermodynamic properties of liquid MgO at 0 GPa and 3000 K from the model implemented in BurnMan (Cottaar et al., 2014) and used in our work. Values from previous models by de Koker and Stixrude (2009) (dK09) and Boukaré et al. (2015) (B15) are included for comparison. For dK09 we give values for the model with $\mathcal{O}_\theta = 2$ (equation 4.9).

Parameters	BurnMan	dK09	B15
V (cm ³ ·mol ⁻¹)	16.5	16.5	16.2
K_T (GPa)	33.6	32.2	37.7
K'_T	4.8	4.9	-
α (10 ⁻⁵ K ⁻¹)	9.4	12.6	9.1
S (J·mol ⁻¹ ·K ⁻¹)	174	175	-
C_P (J·mol ⁻¹ ·K ⁻¹)	75	78	73
γ	0.86	1.28	-

interaction parameter $W_{\text{MgO-SiO}_2}$ at 24 GPa discussed above, and (iv) mixing properties for the liquids along the MgO-SiO₂ join estimated by de Koker et al. (2013). The melting point of MgSiO₃ at 24 GPa is not used as a constraint; rather, it serves as a consistency check for the results of the mixing model and the thermodynamic parameters for SiO₂ liquid. Using 1000 Monte Carlo passes, we find an optimized thermodynamic description for SiO₂ (Tables 5.1 and 5.2) and model a T -dependent Margules parameter (Section 4.6) of

$$W_{\text{MgO-SiO}_2} = -174(\pm 4) \frac{\text{kJ}}{\text{mol}} - 17(\pm 2) \frac{\text{J}}{\text{mol}\cdot\text{K}} T. \quad (5.1)$$

The value for W_S is consistent with entropy of mixing reported by de Koker et al. (2013) from ab-initio simulations. At 25 GPa, minimum values for excess Gibbs energy of mixing in the various thermodynamic models developed for high P applications fall in the range of - (50-60) kJ/mol, with the exception of that of Miyazaki and Korenaga (2019) (Figure 5.3). At

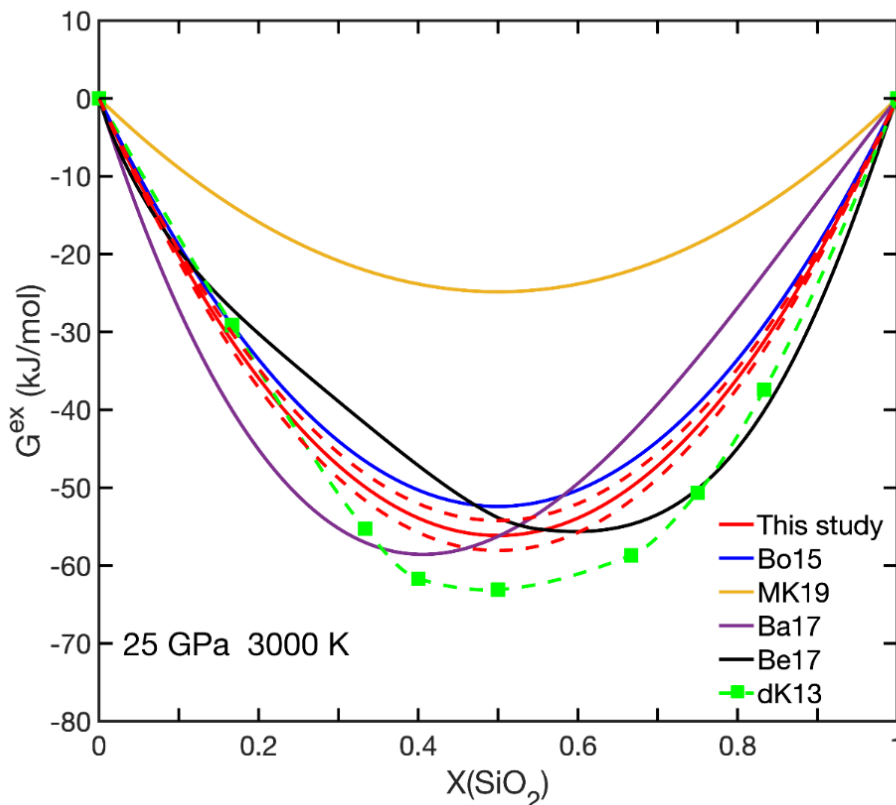


Figure 5.3: Excess Gibbs energy of mixing of MgO-SiO₂ liquids at 25 GPa, 3000 K, showing a comparison of the thermodynamic analysis Belmonte et al. (2017) (Be17, solid black) with thermodynamic models developed for and used at high P . Of those, our model (red line with uncertainty given by the dotted lines), and that of Baron et al. (2017) (Ba17, purple line) are only T dependent, for Boukaré et al. (2015) (Bo15, blue line) and Miyazaki and Korenaga (2019) (MK19, golden line), we use $P = 25$ GPa in evaluating their models. Only Baron et al. (2017) use an asymmetric model. Results by de Koker et al. (2013) (dK13, green symbols) are shown for compositions for which molecular dynamics simulations were performed.

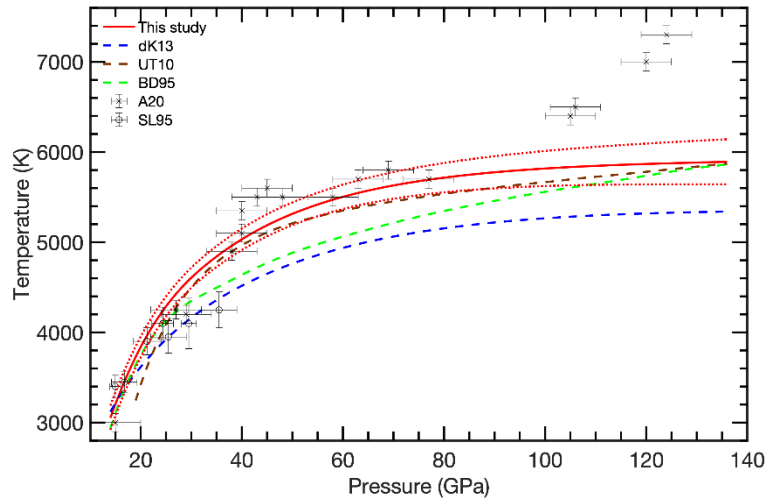


Figure 5.4: Melting curve of SiO_2 stishovite. Results from our thermodynamic model are shown by red solid lines, the red dotted lines represent uncertainties calculated by Monte Carlo simulations (two standard deviations). We include experimental data by Shen and Lazor (1995) (SL95, crosses) and Andrault et al. (2020) (A20, circles). Previously determined melting curves (dashed lines) from *ab initio* simulations by Usui and Tsuchiya (2010) (UT10, brown) and Belonoshko and Dubrovinsky (1995) (BD95, green) and by the thermodynamic model of de Koker et al. (2013) (dK13, blue) are shown for comparison.

this (and higher) P , the mixing model by de Koker et al. (2013) shows very little asymmetry.

Any P dependence discussed below hinges on the thermodynamic description of the liquid and solid components, and an implicit P dependence of the interaction parameter via T . In this context, not only the evolution of the eutectic points with P are important, but also the melting curve $T_m - P$ for MgSiO_3 as a consistency check as it involves both thermodynamic parameters for SiO_2 and the parametrization of $W_{\text{MgO-SiO}_2}$ (equation 5.1), similar to its role at 24 GPa.

5.3 MgO-SiO₂ melting relations at experimental pressure at 24 GPa

Combining $W_{\text{MgO-SiO}_2}$ and the modified thermodynamic parameters as described above, we compute the MgO-SiO₂ phase diagram at $P = 24$ GPa (Figure 5.2). It hinges on five points: T_m of MgO, MgSiO₃ and SiO₂ and the two eutectic points.

$T_m = 4760$ K for MgO computed by BurnMan is very close to that reported in de Koker et al. (2013) (4800 K). For stishovite, we compute $T_m = 4210 \pm 120$ K, with the uncertainty (two standard deviations) determined by 1000 Monte Carlo passes, varying the newly determined

thermodynamic parameters (Tables 5.1 and 5.2), slightly higher than $T_m = 3920$ K from de Koker et al. (2013), but consistent with DAC experiments that bracket melting with $T = 3800 - 4300$ K at $P = 22 - 29$ GPa (Shen and Lazor, 1995) and $T = 4000 - 4400$ K at $P = 27 - 29$ GPa (Andrault et al., 2020) (Figures 5.4).

In the modified model, bridgmanite melting is determined as $T_m = 2750 \pm 120$ K at 24 GPa (Figures 5.2 and 5.5a), slightly below $T_m = 2800 - 2900$ K bracketed in MA experiments by Ito and Katsura (1992), DAC experiments by Zerr and Boehler (1993) and molecular dynamics results by Di Paola and Brodholt (2016). Shock wave experiments (Mosenfelder et al., 2009; Fratanduono et al., 2018) and the thermodynamic assessments of de Koker et al. (2013) and Liebske and Frost (2012) also report slightly larger T_m , most of them marginally within the error bar estimated in the Monte Carlo simulations (Figure 5.5a). The relatively low T_m of bridgmanite established here is directly linked to its narrow stability range on the liquidus in terms of X_{SiO_2} , especially for the SiO_2 -rich side of the phase diagram. Enhancing bridgmanite stability, e.g., by a constant shift of the reference energy in the underlying thermodynamic model of the solid, would inevitably move the eutectic point(s) further away from enstatite composition, making it impossible to match the experimental results. The eutectic points themselves are reproduced well in the Monte Carlo simulations with $T_e = 2690 \pm 100$ K at $X_{\text{SiO}_2} = 0.43 \pm 0.01$ and $T_e = 2740 \pm 120$ K at $X_{\text{SiO}_2} = 0.53 \pm 0.01$. The eutectic T of the latter is smaller than T_m for MgSiO_3 by 10 K only, reflecting the very shallow curvature of the liquidus curve in the vicinity of MgSiO_3 (Figure 5.3). Similar to X_{SiO_2} , a slightly smaller value of T_e for the MgO - MgSiO_3 eutectic is consistent with the thermodynamic assessment of Belmonte et al. (2017).

5.4 MgO-SiO₂ melting relations at lower mantle pressures

As mentioned above, the melting curves for MgO and SiO_2 provide important anchor points for the phase relations at higher P , and that of MgSiO_3 serves as a test for the validity and consistency of the liquid model. For MgO , the melting curve reaches $T_m = 7510$ K at $P = 136$ GPa, CMB pressure, similar to de Koker et al. (2013). This is lower than in the model of Liebske and Frost (2012) with $T_m = 7880$ K, but consistent with a recent thermodynamic assessment of MgO melting (Fuchizaki, 2019). With the changes in the thermodynamic parameters for SiO_2 liquid and stishovite, T_m of SiO_2 at $P = 24$ GPa is larger by ~ 300 K

compared to de Koker et al. (2013) (Figure 5.2), a difference that increases to ~ 550 K at CMB pressure (Figure 5.4). However, our computed melting curve closely follows the experimental data on T_m by Andrault et al. (2020) up to 80 GPa; for $P > 30$ GPa the melting curve computed by Usui and Tsuchiya (2010) is within the margin of error, and they approach the same value at CMB pressures. As has been pointed out by de Koker et al. (2013), potential stishovite metastability in the model – due to the presence of CaCl_2 -

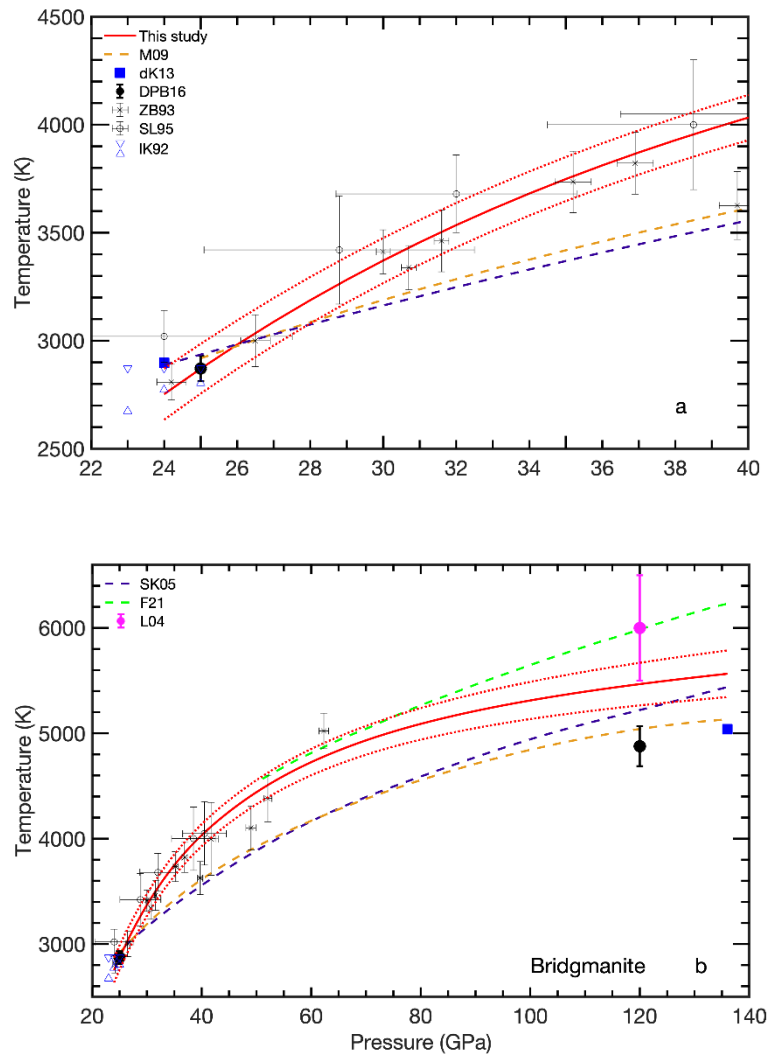


Figure 5.5: Melting curves for MgSiO_3 bridgmanite at lower mantle pressures (a: 20 – 40 GPa and b: 20 – 140 GPa). Results from our thermodynamic model are shown by red solid lines, the red dotted lines represent uncertainties calculated by Monte Carlo simulations. Multi-anvil experiments (Ito and Katsura, 1992) (IK92, blue triangles up and down) bracket melting, and melting temperatures in diamond anvil cell experiments are reported by Zerr and Boehler (1992) (ZB92, crosses) and Shen and Lazor (1995) (SL95, open circles). Melting temperatures from ab-initio simulations by Di Paola and Brodholt (2016) (DPB16, filled black circles) and the model of de Koker et al. 2013 (dK13, blue squares) as well as melting curves (dashed lines) from shock wave experiments by Fratanduono et al. (2018) (F18, green) and Mosenfelder et al. (2009) (M09, orange) and from ab-initio simulations by Stixrude and Karki (2005) (SK05, blue) are included.

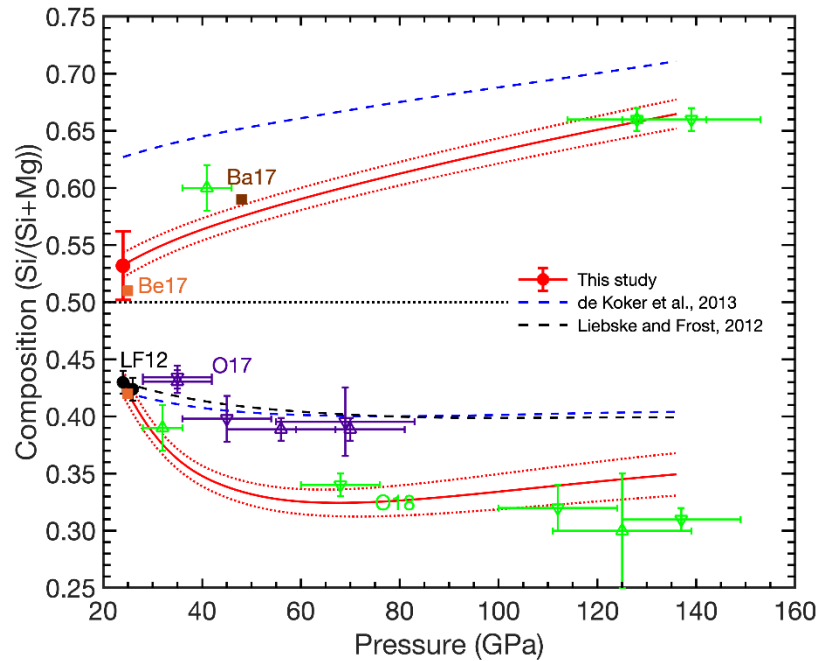


Figure 5.6: Eutectic compositions in the MgO-SiO₂ system at lower mantle pressures. Filled circles indicate liquid compositions based on our multi-anvil press experiments (red) and those by Liebske and Frost (2012) (LF12, black). Diamond anvil cell experiments by Baron et al. (2017) (Ba17, brown), Ozawa et al. (2018) (O18, green) and Ohnishi et al. (2017) (O17, purple) are included, with triangles up and down in the latter two bracketing the eutectic composition, along with results by Belmonte et al. (2017) (Be17, orange) at $P = 25$ GPa. Results from our model are shown by the red solid curves with uncertainties from Monte Carlo simulations given by red dotted curves; they are compared to previous models by Liebske and Frost (2012) (black dashed curve) and de Koker et al. (2013) (blue dashed curves).

structured SiO₂ (Tsuchida and Yagi, 1989) or seifertite (Dubrovinsky et al., 2001) – is negligible or has a small effect on T_m at $P = 136$ GPa, respectively. Which of the high- P phases for SiO₂ is in equilibrium with the liquid at lowermost mantle conditions remains unclear based on the Clapeyron slopes of the transitions determined in experiments (e.g., Grocholski et al., 2013; Fischer et al., 2018; Sun et al., 2019).

For MgSiO₃, the melting curve predicted by our model shows a steep initial increase with P (Figure 5.5a), closely following the trend of the DAC experiments (Zerr and Bohler, 1993, Shen and Lazor 1995) to 40 GPa, and – with larger scatter in the data – to 62 GPa, the highest P achieved in Zerr and Bohler (1993). It also matches the recent melting curve by Fei et al. (2021) based on shock wave experiments for much of the lower mantle P range (50-80 GPa). However, shock wave experiments (Mosenfelder et al., 2009; Fratanduono et al., 2018; Fei et

al., 2021) vary largely in their estimates of the melting curve. At higher P , our predicted melting curve flattens and reaches 5560 ± 220 K at 136 GPa. The melting temperature predicted by Stixrude and Karki (2005) at CMB P is within the margin of error of our model, but their melting curve shows a more uniform increase for LM pressure.

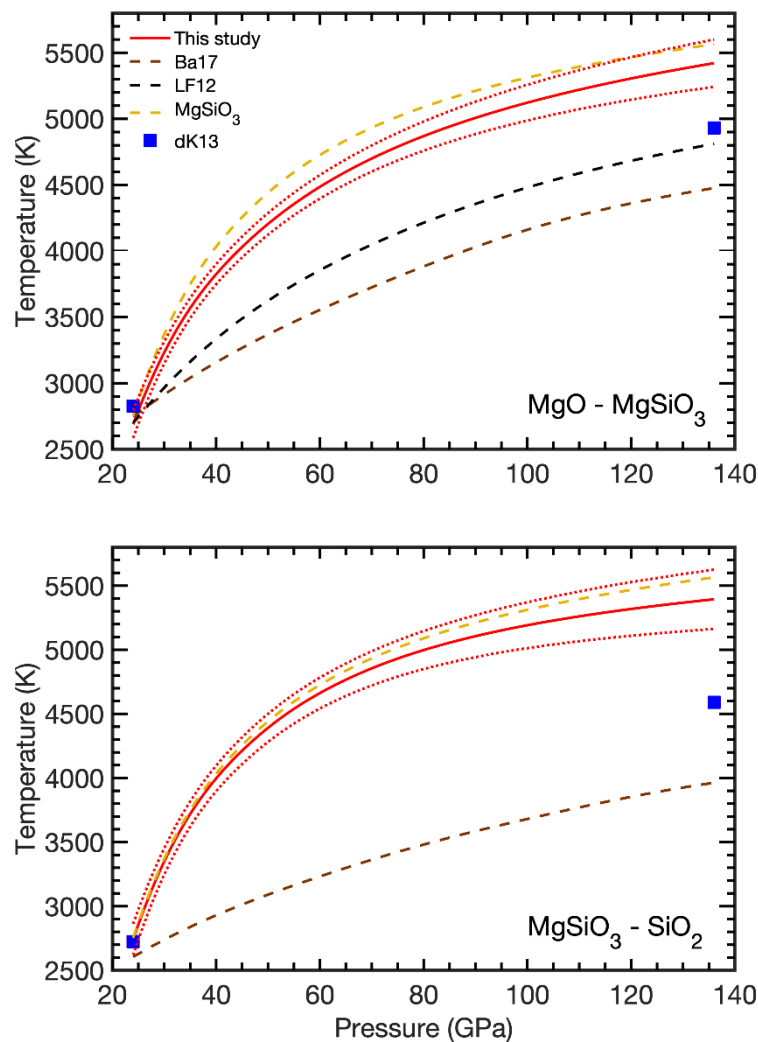


Figure 5.7: Eutectic temperatures in the MgO-MgSiO₃ (a) and the MgSiO₃-SiO₂ systems (b) at lower mantle pressures. Our results are shown by red curves (uncertainties in dotted lines from Monte Carlo simulations), those of Baron et al. (2017) in brown (Ba17), by de Koker et al. (2013) at $P = 24$ GPa and at $P = 136$ GPa by blue symbols (dK13). For the MgO-MgSiO₃ system, eutectic temperatures of the model by Liebske and Frost (2012) are shown in black (LF12). For reference, we include the MgSiO₃ melting curve from our model (golden dashed curves) in both panels.

The consistency of predicted melting curve evolution with prior data for all three congruently melting compositions along the MgO-SiO₂ join allows us to calculate the phase diagram at $P = 136$ GPa with some confidence (Figure 5.2) and to explore the evolution of both

eutectics in terms of X_{SiO_2} (Figure 5.6) and T_e (Figure 5.7).

In agreement with previous work, we find that both eutectics move away from MgSiO_3 with P . For the MgO-MgSiO_3 eutectic, X_{SiO_2} shifts to lower values with P significantly faster than in the models of de Koker et al. (2013) and Liebske and Frost (2012) or the experimental brackets determined in the DAC by Ohnishi et al. (2017) between 45 and 70 GPa. The P dependence of the eutectic composition for MgO-MgSiO_3 agrees well with a second set of DAC experiments by Ozawa et al. (2018) over the P range of the entire LM. The MgO-MgSiO_3 eutectic in our model has a minimum value of $X_{\text{SiO}_2} = 0.32 \pm 0.02$ at $P \sim 60$ GPa, beyond which it increases quasi-linearly with P to reach $X_{\text{SiO}_2} = 0.35 \pm 0.02$ at CMB pressure. This P behavior stems from the balance between a negative T dependence of $W_{\text{MgO-SiO}_2}$ and T_m for MgO increasing steeply with P : A smaller value (i.e., larger in magnitude) for $W_{\text{MgO-SiO}_2}$ results in larger X_{SiO_2} at the eutectic, a larger T_m for MgO in smaller X_{SiO_2} .

As discussed above, the $\text{MgSiO}_3\text{-SiO}_2$ eutectic composition is close to MgSiO_3 with $X_{\text{SiO}_2} = 0.53 \pm 0.01$ at $P = 24$ GPa in our experiments and model, consistent with Belmonte et al. (2017), but significantly lower than X_{SiO_2} calculated by de Koker et al. (2013). As T_m for SiO_2 does not increase with P at the same rate as that for MgO , eutectic X_{SiO_2} moves to larger values with P , reaching a value of $X_{\text{SiO}_2} = 0.66 \pm 0.01$ at 136 GPa. As for the MgO-MgSiO_3 system, experiments by Ozawa et al. (2018) at $P = 128$ GPa and $P = 139$ GPa agree well with our prediction, with values that are smaller than the model of de Koker et al. (2013). While Baron et al. (2017) assume the chemical evolution of the eutectic following de Koker et al. (2013) in their data analysis, the actual composition reported for one sample at $P = 48$ GPa reveals a significantly lower value with $X_{\text{SiO}_2} = 0.59$, within the margin of error of our model prediction, and in general agreement with data by Ozawa et al. (2018) at $P = 41$ GPa.

Eutectic temperatures in the MgO-MgSiO_3 and $\text{MgSiO}_3\text{-SiO}_2$ systems are very close to one another, rising from $T_e = 2690 \pm 100$ K and $T_e = 2740 \pm 120$ K at $P = 24$ GPa to $T_e = 5420 \pm 180$ K and $T_e = 5390 \pm 230$ K at $P = 136$ GPa, respectively (Figures 5.2 and 5.7). MgO-MgSiO_3 and $\text{MgSiO}_3\text{-SiO}_2$ eutectic temperatures cross at $P \sim 125$ GPa, reflecting the opposing trends of eutectic X_{SiO_2} relative to MgSiO_3 (Figure 5.6). The difference of T_e to the

melting curve of MgSiO₃ does not exceed 200 K over the whole LM. At CMB pressure, our model shows higher T_e by 500-700 K than the models of de Koker et al. (2013) and Liebske and Frost (2012) for MgO-MgSiO₃, and higher T_e by 800 K compared to de Koker et al. (2013) for MgSiO₃-SiO₂. Eutectic T estimated by Baron et al. (2017) appear rather low in this context.

5.5 Melting near the core mantle boundary

This similarity in T_e – and therefore solidus temperature – for MgO-MgSiO₃ and MgSiO₃-SiO₂ predicted here suggests that melting of basalt at lower T than peridotite (Tateno et al., 2014; 2018; Kuwahara et al., 2018; Andraut et al., 2014; Pradhan et al., 2015) – invoked as an explanation for the occurrence of the ULVZ in the lowermost mantle (e.g., Thorne et al., 2019) – is not simply tied to its higher X_{SiO_2} value. Rather, further differences in chemical composition will influence T_m and melt relations either directly within a solid solution (e.g., a higher FeO or Al₂O₃ content in the bridgmanite solid solution) or through changes in the resulting phase assemblage.

Compared to mantle pyrolite (Workman and Hart, 2005), oceanic crust is strongly enriched in Al₂O₃, CaO and Na₂O, while the FeO content is similar in both lithologies (e.g., Chermia et al., 2015). For oceanic crust this leads to a phase assemblage that differs in various aspects from peridotite at LM pressure: (i) it contains significantly more CaSiO₃ perovskite (e.g., Chust et al., 2017) and (ii) SiO₂ occurs as a free phase rather than the ferropericlase solid solution. Both CaSiO₃ perovskite and SiO₂ stishovite in the oceanic crust dissolve a few % of Al₂O₃ and very little FeO (e.g., Kuwahara et al., 2018; Tateno et al., 2018), while ferropericlase in a pyrolytic composition contains up to 20% FeO (e.g., Chust et al., 2017; Kuwahara et al., 2018). Further, (iii) for basalt an Al₂O₃ dominated mineral occurs in the LM, either as Ca-ferrite (Irifune and Ringwood, 1993; Tateno et al., 2018) or the NAL phase (Kato et al., 2013; Imada et al., 2012). As a consequence of these phase relations, bridgmanite in a basaltic composition can be expected to be significantly enriched in FeO compared to a mantle peridotite. A high FeO content in partial melts from basalt compositions at LM pressure (Pradhan et al., 2015; Kuwahara et al., 2018, Tateno et al., 2018) suggests that the solidus T in the resulting bridgmanite is significantly lower than the eutectic in the MgSiO₃-SiO₂ system established here. This is further supported by the

observation that while CaSiO_3 perovskite is the phase on the solidus in peridotite at LM pressure, it becomes the liquidus phase for MORB compositions, and bridgmanite simultaneously becomes the solidus phase (Tateno et al., 2014; 2018; Pradhan et al., 2015; Kuwahara et al., 2018).

However, the chemical complexity of natural or model systems investigated in these studies makes it challenging to disentangle the causes for these discrepancies. In order to analyze the influence of other chemical components in a systematic way by building up a thermodynamic model for mantle compositions, controlled melting experiments in the MA press like the ones performed here are required. The choice of systems should not simply be dictated by chemical abundances, but also the crystal chemical and phase relation arguments outlined in the previous paragraph, such a model should be built up successively from the two-component system explored here to FeO-MgO-SiO₂ (Chapter 6) and subsequently to FeO-MgO-Al₂O₃-SiO₂ systems which will provide successive insight into the influence of FeO on melting in the bridgmanite solid solution and the addition of an Al₂O₃-rich phase to the assemblage on melting relations.

5.6 Summary

In multi-anvil experiments at 24 GPa we have measured the compositions of partial melts formed from a $\text{Mg}_{0.4}\text{Si}_{0.6}\text{O}_{1.6}$ starting composition at a temperature of 2750 ± 100 K. Scanning electron microscope and electron microprobe analysis of the recovered experimental charges reveal that stishovite is the crystalline phase at the liquidus, and the coexisting liquid has a composition of $X_{\text{SiO}_2} = 0.53 \pm 0.03$. This implies an MgSiO_3 -SiO₂ eutectic that is very close to MgSiO_3 bridgmanite in composition which is therefore the liquidus phase in the MgO-SiO₂ system over a compositional range from $X_{\text{SiO}_2} = 0.43$ (Liebske and Frost, 2012) to $X_{\text{SiO}_2} = 0.53$, with very similar eutectic (solidus) temperatures. Using these eutectics as constraints to the thermodynamics for the liquid components SiO₂ and MgO as well as the solid phases SiO₂ stishovite, MgO periclase and MgSiO_3 bridgmanite, we model the melting phase relations in the MgO-SiO₂ system using a symmetric solution model for the liquid components.

The extrapolation of our thermodynamic description for melting relations to higher pressures hinges on its temperature dependence and the melting curves of MgO and SiO₂. Our model

describes melting of MgSiO_3 bridgmanite consistent with diamond anvil cell experiments up to 60 GPa, and recent shock wave experiment to 80 GPa. In our model, the eutectic compositions move to $X_{\text{SiO}_2} = 0.35 \pm 0.02$ and $X_{\text{SiO}_2} = 0.66 \pm 0.02$ at core-mantle boundary pressure, respectively. Eutectic temperatures of these two compositions remain similar, suggesting that lower solidus temperatures of basalt over peridotite in the deep mantle – which has been observed in a series of prior experiments on natural or model compositions – must be related to chemical components other than SiO_2 and MgO .

6. Iron partitioning and melting phase relations in FeO-MgO-SiO₂ system under lower mantle conditions

The FeO component in mantle composition exerts a strong influence on the structure and evolution of the Earth's lower mantle (Chapter 1) as it strongly affects physical properties of mineral phases and melting relations (Chapter 2). As illustrated in Figure 2.2, significant variations exist in experimentally determined partitioning of FeO between bridgmanite and the coexisting liquid, and multi-anvil experiments report $K_D = (\text{Fe}^{\text{solid}}/\text{Mg}^{\text{solid}})/(\text{Fe}^{\text{liquid}}/\text{Mg}^{\text{liquid}})$ between 0.2 and 0.5 at 24 GPa (Hirose and Fei 2002; Trønnes and Frost 2002; Liebske et al., 2005) (Figure 2.2). Differences in iron partitioning can be caused by T and composition (Liebske et al., 2005), but to date their relative influence on K_D have not been systematically quantified. Here, we perform multi-anvil experiments to investigate melting phase relations in the model system $(\text{Mg}_{1-x}\text{Fe}_x)\text{SiO}_3$ at 24 GPa, with $x = 0.1, 0.2, 0.3$ and 0.5 , and in a T range 2510-2650 K (Table 3.2), and extract thermodynamic information from the data to model melt relations in the FeO-MgO-SiO₂ system at 24 GPa, evaluate these along selected binary joins, and compare to experiments where available; finally we extrapolate to conditions of the CMB.

6.1 Experimental results

Recovered samples from the $(\text{Mg}_{0.9}\text{Fe}_{0.1})\text{SiO}_3$ melting experiments (Table 3.2) are characterized by two distinct parts in the capsule, representing a quenched liquid portion coexisting with bridgmanite (Figure 6.1). On the left, the liquid exhibits a bright net structure with high iron concentration. Solid crystals are darker and contain less iron. Similar observations also hold for the starting compositions $(\text{Mg}_{0.8}\text{Fe}_{0.2})\text{SiO}_3$ and $(\text{Mg}_{0.7}\text{Fe}_{0.3})\text{SiO}_3$, while for $(\text{Mg}_{0.5}\text{Fe}_{0.5})\text{SiO}_3$, the solid portion consists of an assembly of bridgmanite, magnesiowüstite and stishovite (Figure 6.2). The occurrence of the multi-phase assemblage in coexistence with the liquid suggests that the solubility limit of FeSiO_3 in bridgmanite in equilibrium with the liquid has been reached in the experiment.

The chemical compositions of coexisting bridgmanite and liquid phases measured by EPMA are listed in Table 6.1. Bridgmanite maintains a stoichiometry $X_{\text{SiO}_2} = 0.5$, suggesting that all iron is incorporated as FeO rather than Fe_2O_3 . While the FeO content in bridgmanite increases in a quasi-linear fashion, the presence of a multi-component phase assemblage in equilibrium with the liquid for the $(\text{Mg}_{0.5}\text{Fe}_{0.5})\text{SiO}_3$ starting composition yields a

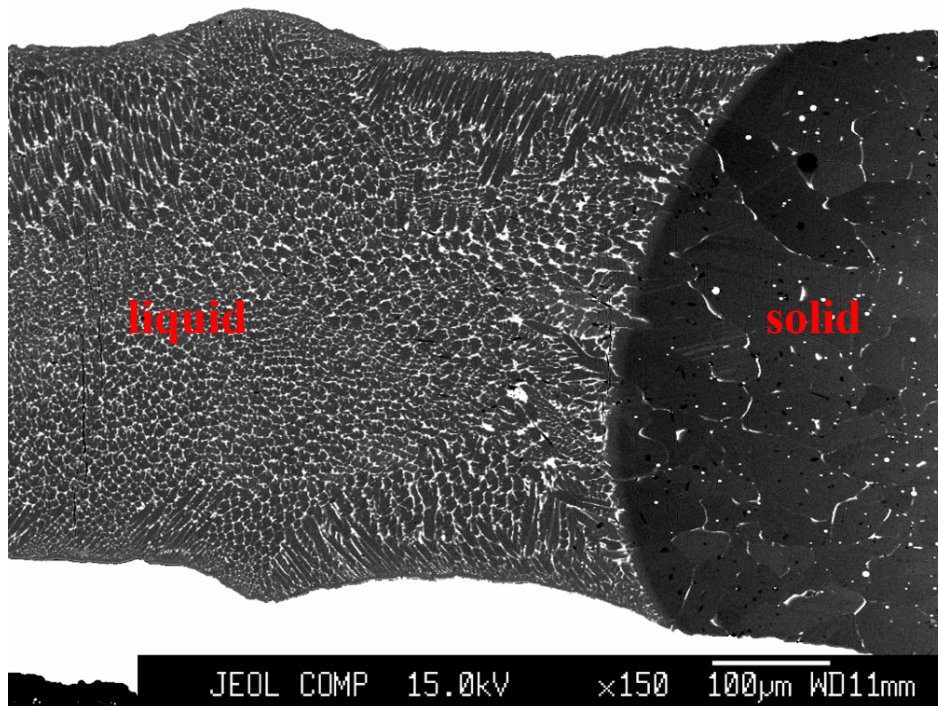


Figure 6.1: Back scattered electron image of a recovered experimental product with $(\text{Mg}_{0.9}\text{Fe}_{0.1})\text{SiO}_3$ starting composition heated to 2650 ± 100 K at 24 GPa. The sample has experienced partial melting, with typical melt quench texture on the left side. The melt coexists with bridgmanite (dark field on the right side) showing that bridgmanite is the phase on the liquidus.

solubility limit for FeSiO_3 in bridgmanite of $X_{\text{FeSiO}_3} = 0.16 \pm 0.02$. We find that the content of oxide components in the liquid correlates linearly with X_{FeO} in the solid, with FeO preferentially partitioning into the liquid, while MgO and SiO_2 are refractory and remain in the solid (Figure 6.3), with MgO more refractory than SiO_2 .

At similar pressure (26 ± 1 GPa), EPMA data for bridgmanite melting in peridotite with 30 %wt excess Fe metal (Liebske et al., 2005) agree well with the FeSiO_3 content of both our liquid and solid bridgmanite. This suggests that melting phase relations in the FeO-MgO- SiO_2 system provide a reliable analogue for complex systems such as peridotite or chondrite. An Al_2O_3 -rich composition investigated by Liebske et al. (2005) leads to a smaller iron content in bridgmanite, showing that compositions with higher Al_2O_3 – including basalts (Table 1.1) – appear to affect iron partitioning strongly. This and similar compositional effects may be responsible for differing K_D values in previous experiments (Nomura et al., 2011; Andrault et al., 2012).

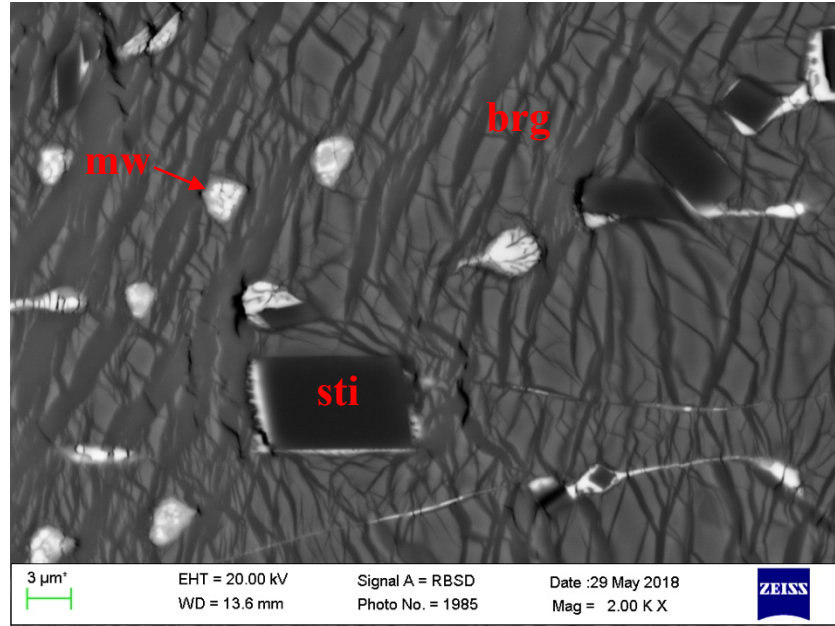


Figure 6.2: Scanning electron microscope image for the solid portion of the recovered run product from the $(\text{Mg}_{0.5}\text{Fe}_{0.5})\text{SiO}_3$ melting experiment at 24 GPa and 2510 ± 100 K. Three solid phases coexist: bridgmanite (brg), the dominant phase which features grey bands and lots of cracks, FeO-rich magnesiowüstite (mw) in bright white color (rounded grains with ~ 2 μm diameter), and stishovite (sti) as dark rectangular grains.

Table 6.1: Compositions of the solid and liquid components in the melting experiments performed in the multi-anvil press at 24 GPa. Each block lists in the first line the initial composition along the MgSiO_3 - FeSiO_3 join are listed, the heating power and corresponding temperature, the phases that are present in the recovered sample, as well as the experiment number. Below, the chemical analysis of the run products (solid and liquid) in terms of MgO, FeO and SiO_2 by electron microprobe are listed and compared to the prediction of the thermodynamic model we developed based on the results. Abbreviations are: liq for liquid, brg for bridgmanite, mw for magnesiowüstite and sti for stishovite.

	bridgmanite composition (mol fraction)		liquid composition (mol fraction)	
	measurements	model	measurements	model
$(\text{Mg}_{0.9}\text{Fe}_{0.1})\text{SiO}_3$, 449 W (2650 \pm 100 K), phases: liq + brg (S6953)				
MgO	0.485 ± 0.010	0.484	0.452 ± 0.012	0.444 ± 0.011
FeO	0.015 ± 0.009	0.017	0.046 ± 0.009	0.046 ± 0.009
SiO_2	0.499 ± 0.010	0.500	0.502 ± 0.012	0.509 ± 0.010
$(\text{Mg}_{0.8}\text{Fe}_{0.2})\text{SiO}_3$, 443 W (2615 \pm 100 K), phases: liq + brg (S6992)				
MgO	0.463 ± 0.010	0.467	0.418 ± 0.008	0.412 ± 0.020
FeO	0.033 ± 0.010	0.033	0.099 ± 0.008	0.111 ± 0.026
SiO_2	0.504 ± 0.010	0.500	0.483 ± 0.007	0.476 ± 0.031
$(\text{Mg}_{0.7}\text{Fe}_{0.3})\text{SiO}_3$, 435 W (2580 \pm 100 K), phases: liq + brg (S7024)				
MgO	0.446 ± 0.010	0.446	0.366 ± 0.008	0.357 ± 0.024
FeO	0.058 ± 0.010	0.055	0.184 ± 0.007	0.176 ± 0.041
SiO_2	0.496 ± 0.010	0.500	0.451 ± 0.007	0.467 ± 0.040
$(\text{Mg}_{0.5}\text{Fe}_{0.5})\text{SiO}_3$, 420 W (2510 \pm 100 K), phases: liq, brg, mw, sti (S7052)				
MgO	0.422 ± 0.010	0.415	0.304 ± 0.015	0.269 ± 0.031
FeO	0.083 ± 0.010	0.084	0.279 ± 0.018	0.338 ± 0.086
SiO_2	0.495 ± 0.010	0.500	0.417 ± 0.016	0.394 ± 0.059

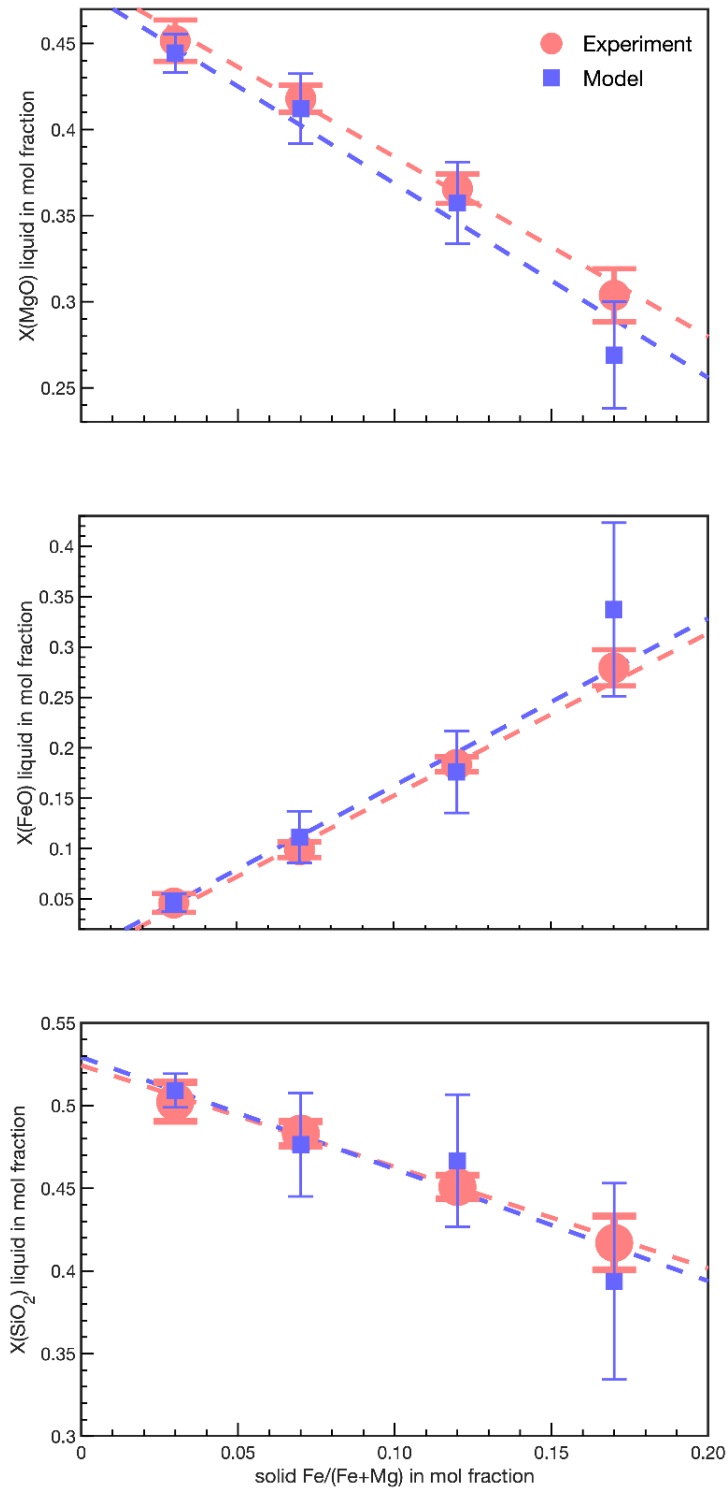


Figure 6.3: Liquid composition (MgO, FeO and SiO₂ fraction) as a function of iron content in the coexisting bridgmanite solid (Table 6.1). Data represent the experiments with starting compositions (Mg_{1-x}Fe_x)SiO₃, $x = 0.1, 0.2, 0.3$ and 0.5 from left to right. Experimental values are shown by red circles, the results from thermodynamic modelling in blue squares. Error bars are uncertainties are from experimental data or Monte Carlo simulations, respectively. Note that the temperature of the experiments is decreasing from 2650 to 2510 ± 100 K with increasing Fe content of the starting composition (Table 3.2).

Table 6.2: Physical parameters for the Mie-Grüneisen Birch-Murnaghan thermodynamic model (equations 4.1, 4.2 and 4.5) used in the BurnMan database for FeSiO₃ bridgmanite from the database of Stixrude and Lithgow-Bertelloni (2011) and for FeO wüstite based on Fischer et al. (2011). For wüstite, the parameters of the Mie-Grüneisen Birch-Murnaghan model from Fischer et al. (2011) are recomputed at 1600 K.

	FeSiO ₃ bridgmanite	FeO wüstite
V_0 (cm ³ ·mol ⁻¹)	26.83	13.05
T_0 (K)	2000	1600
F_0 (kJ·mol ⁻¹)	-3202	-830
K_0 (GPa)	216	122.6
K'_0	4.35	3.7
γ_0	1.66	1.45
q_0	1.1	0.5
S_0 (J·K ⁻¹ ·mol ⁻¹)	281	149
C_{V0} (J·K ⁻¹ ·mol ⁻¹)	124	57.1

6.2 Thermodynamic parameters for the FeO-MgO-SiO₂ system

For the endmembers in the MgO-SiO₂ system we continue to use the thermodynamic description discussed in Section 5.2, and complement these with models for the Fe-bearing system (Table 6.2): For FeSiO₃ bridgmanite we take the Mie-Grüneisen Birch-Murnaghan model of Stixrude and Lithgow-Bertelloni (2011). For solid FeO wüstite we implement the model of Fischer et al. (2011) in BurnMan, shifting the reference temperature to 1600 K, close to melting with 1650 K (Patnaik 2003). Liquid FeO parameters (Tables 6.3 and 6.4) are determined by matching the Gibbs energy of the solid along the melting curve (Section 6.3).

The interaction parameters for MgO-SiO₂ and FeO-SiO₂ are constrained from four data points (Table 6.1), by solving equations 4.32 and 4.33 simultaneously with a least square Monte Carlo minimization. For MgO-FeO we assume ideal mixing, following the prior work by Boukaré et al. (2015) and Miyazaki and Korenaga (2019). Since we do not have any P dependent experimental data, our modeled Margules parameters (stated with 1 σ uncertainty) depend only on T :

$$W_{\text{MgO-SiO}_2} = -184(\pm 3) \frac{\text{kJ}}{\text{mol}} - 16(\pm 2) \frac{\text{J}}{\text{mol}\cdot\text{K}} T \quad (6.1)$$

$$W_{\text{FeO-SiO}_2} = -41(\pm 9) \frac{\text{kJ}}{\text{mol}} - 2(\pm 3) \frac{\text{J}}{\text{mol}\cdot\text{K}} T \quad (6.2)$$

The $W_{\text{MgO-SiO}_2}$ parameters (both $W_{\text{MgO-SiO}_2}^0$ and $W_{\text{MgO-SiO}_2}^S$) are consistent with our result in Chapter 5 within 2 σ which we use as an initial guess in the Monte Carlo simulations.

$W_{\text{FeO-SiO}_2}$ is significantly smaller in magnitude than $W_{\text{MgO-SiO}_2}$, indicating a weaker

Table 6.3: Expansion coefficients a_{ij} for the excess Helmholtz energy (equation 4.9) in terms of finite strain f (equation 4.3) and a reduced temperature expression θ (equation 4.8, with optimized exponent m) for FeO liquids. Reference conditions of volume (V_0) and temperature (T_0), as well as the expansion orders (\mathcal{O}_f and \mathcal{O}_θ) in equation 4.9 are provided.

Parameters	FeO
V_0 (cm ³ ·mol ⁻¹)	15.05
T_0 (K)	3000
\mathcal{O}_f	3
\mathcal{O}_θ	2
m	0.64
a_{00}	-687
a_{10}	-101
a_{01}	189
a_{20}	7918
a_{11}	351
a_{02}	-43.9
a_{30}	$38 \cdot 10^3$
a_{21}	-848
a_{12}	152
a_{31}	$-52.5 \cdot 10^3$
a_{22}	-5756

interaction between iron and silicon, similar to the model by Boukaré et al. (2015) with $W_{\text{FeO-SiO}_2}^0 = -45.2$ kJ/mol. In their Monte Carlo sampling, Miyazaki and Korenaga (2019) find $W_{\text{FeO-SiO}_2}^0$ poorly constrained, with values ranging from $-170(\pm 45)$ kJ/mol to $-100(\pm 114)$ kJ/mol, which they attribute to the small amount of iron typically in the samples they use in the inversion and the very limited range of FeO stability above the solidus (Section 6.4). Our value for $W_{\text{FeO-SiO}_2}^\delta$ is zero within the margin of error which validates the assumption of T independence of the FeO-SiO₂ interaction by Boukaré et al. (2015) and Miyazaki and Korenaga (2019).

6.3 FeO melting curve under high pressure

Contrary to our approach for the MgO-SiO₂ system (Section 5.2) where we determine thermodynamic parameters for SiO₂ liquid and stishovite as well as the Margules parameter $W_{\text{MgO-SiO}_2}$ jointly based on the existing thermodynamic models of de Koker et al. (2013) and Stixrude and Lithgow-Bertelloni (2011), we need to construct a thermodynamic description for FeO liquid. For this we use the model of FeO wüstite by Fischer et al. (2011) (Table 6.2)

Table 6.4: Thermodynamic properties of liquid FeO at 0 GPa and 3000 K from the model developed here using BurnMan. Values from previous models by Boukaré et al. (2015) (B15), Frost et al. (2010) (F10) and Komabayashi (2014) (K14) are included from comparison.

Parameters	This Study	F10	K14	B15
V (cm ³ ·mol ⁻¹)	15.50	15.28	14.94	18.48
K_T (GPa)	49.26	53.2	81.6	30.19
K'_T	5.81	4.40	-	-
α (10 ⁻⁵ K ⁻¹)	6.34	5.76	4.7	9.54
S (J·mol ⁻¹ ·K ⁻¹)	218.06	218	218.1	-
C_P (J·mol ⁻¹ ·K ⁻¹)	81.99	80.2	-	137
γ	0.66	-	0.79	-

and fit the thermodynamic parameters for the liquid by matching the melting curve of FeO over a wide P range (equations 4.6 and 4.28, Tables 6.3 and 6.4). We chose the datasets of Lindsley (1966) at 1-3 GPa from piston cylinder experiments and that of Fu et al. (2018) at 50-120 GPa from DAC experiments (Figure 6.4). The former provides reliable T measurements at low P , which is widely used in the literature and agrees well with the extrapolation of high P melting data (McCammon et al., 1983; Beattie et al., 1991; Shen et al., 1993; Frost et al., 2010). The data of Fu et al. (2018) is based on modelling melt relations in the MgO-FeO system and extrapolating to the FeO endmember. Their data agree with direct DAC data of FeO melting at high P (Fischer and Campbell, 2010) and systematic considerations in the Fe-FeO (Oka et al., 2019) and FeO-SiO₂ (Kato et al., 2016) systems. In the P range 5-50 GPa, experiments differ significantly in terms of the melting curve for FeO (Figure 6.4), and by using the data from Lindsley (1966) and Fu et al. (2018) we avoid preferentially picking one data set over the other.

Our melting curve shows a relatively large dT/dP slope below 20-40 GPa, and a gradual T increase for higher P , while other models continue with a steep dT/dP (Komabayashi, 2014) to CMB P or predict a change in slope at higher P (Frost et al., 2010). These two models match the experimental brackets of liquidus and solidus T of MA experiments by Tsuno et al. (2007), with three data points in the P -range 15-21 GPa, and a single DAC experiment by Seagle et al. (2008) at 50 GPa, but direct melting experiments (Shen et al., 1993; Fischer and Campbell, 2010) yield significantly lower T . In addition to the dataset by Fu et al. (2018) used for fitting, our model matches the melt brackets by Tsuno et al. (2007) at the two lower P points, is in reasonable agreement with melting in the experiments by Shen et al. (1993) over their entire P range and with the data by Fischer and Campbell (2010) for $P > 30$ GPa. The data by Fischer and Campbell (2010) at lower P show significant scatter, and melting

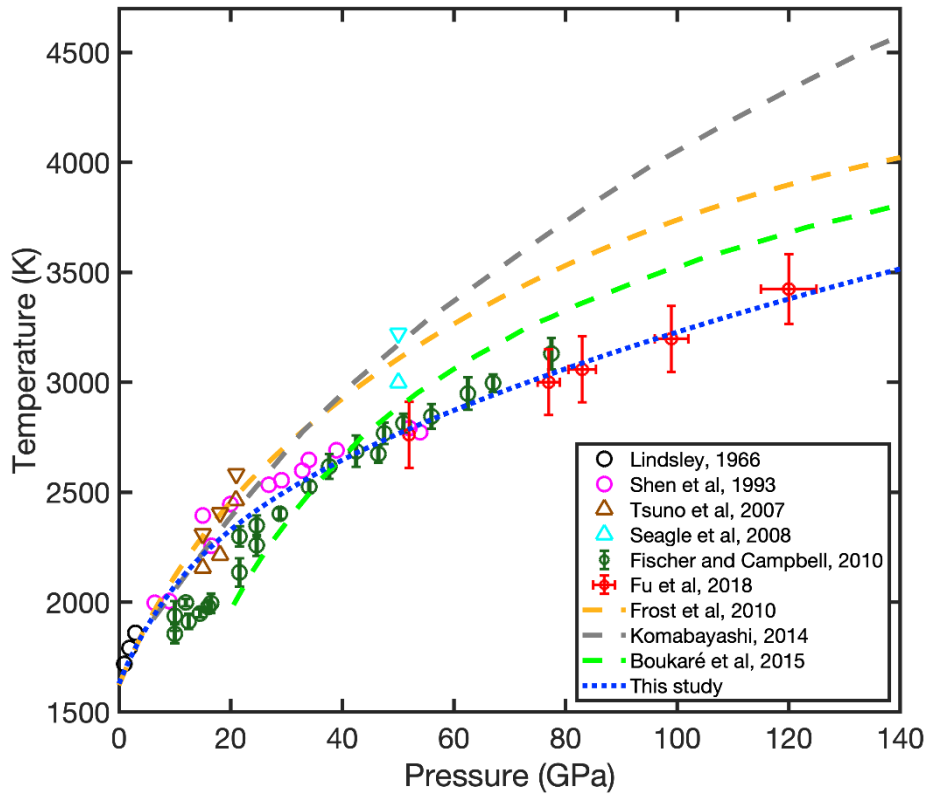


Figure 6.4: Melting curve of FeO constrained in our study (dotted blue line) by equating the Gibbs energy of wüstite and FeO liquid. For comparison we show previously established melting curves from models of Komabayashi, (2014) (grey dashed line), Boukaré et al, (2015) (green dashed line) and Frost et al. (2010) (orange dashed line) and experimental data by Lindsley (1966) (black circles), Shen et al. (1993) (magenta circles), Fischer and Campbell (2010) (dark green circles) and Fu et al. 2018 (red circles); melt brackets by Tsuno et al. (2007) (brown) and Seagle et al. (2008) (cyan) are indicated by triangles pointing up and down.

points that appear low in comparison to the piston cylinder experiments by Lindsley (1966) and melt brackets from MA experiments by Tsuno et al. (2007).

6.4 Iron partitioning and FeO-MgO-SiO₂ melting phase relations at 24 GPa

As mentioned in Section 6.1, the simplified FeO-MgO-SiO₂ system appears to represent partitioning data of mantle composition and complex natural system well (Liebske et al., 2005). We find K_D to increase from 0.20 to 0.35 with decreasing iron content in the coexisting solid bridgmanite (Figure 6.5), similar to the value established by Liebske et al. (2005) for a composition of peridotite plus 30 wt% iron (Figure 2.2) at 24 GPa and for peridotites in DAC experiments by Tateno et al. (2014) and Nomura et al. (2011) at 35 GPa. Significantly larger or smaller K_D values in other experiments at similar P (Hirose and Fei, 2002; Trønnes and Frost, 2002) (Figure 2.2), including the other two compositions melted in Liebske et al. (2005), suggest that they are caused by compositional variations. Our

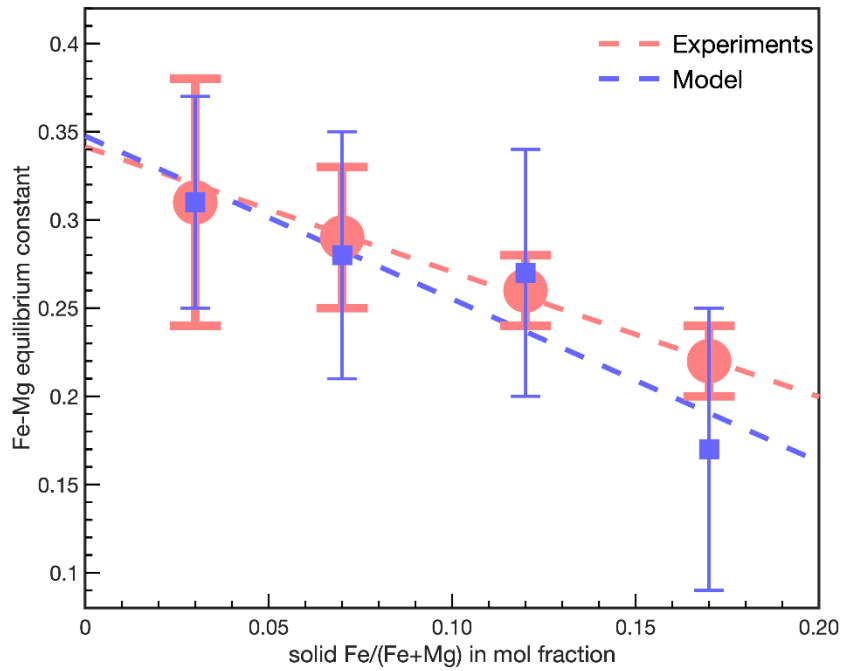


Figure 6.5: Fe-Mg equilibrium constant $K_D = (\text{Fe}^{\text{solid}}/\text{Mg}^{\text{solid}})/(\text{Fe}^{\text{liquid}}/\text{Mg}^{\text{liquid}})$ between bridgmanite and melt as a function of iron content in solid bridgmanite at 24 GPa and temperatures of the experiment (Table 6.1). The starting compositions are $(\text{Mg}_{1-x}\text{Fe}_x)\text{SiO}_3$, $x = 0.1, 0.2, 0.3$ and 0.5 from left to right. Experimental data are shown by red circles, and the thermodynamic model results by blue squares. Vertical lines represent the error bar and dashed lines show the compositional trend of K_D .

thermodynamic model reproduces experimental liquid compositions in coexistence with solid bridgmanite (Figure 6.3) and the resulting K_D (Figure 6.5) at experimental conditions well. Boukaré et al. (2015) demonstrate a strong dependence of K_D on T between the solidus and liquidus, with values decreasing from 0.8 to 0.2 (although they do not specify compositions). As temperatures in our experiments are close to the liquidus for all compositions considered (Figure 6.6), the agreement between these studies is encouraging. The model by Miyazaki and Korenaga (2019), by contrast, predicts $K_D \ll 0.1$ at 30 GPa, at odds with all other studies. This discrepancy may be related to the construction of their model from the MgO-FeO phase diagram with a very narrow liquid-solid coexistence, as they state in their discussion, or be related to their higher (less negative) values for excess Gibbs energy of mixing in the binary MgO-SiO₂ at 25 GPa at 3000 K (Figure 5.3).

Temperatures in the four melting experiments decrease quasi-linearly with FeSiO₃ content in bridgmanite (Table 6.1) while producing a comparable degree of partial melting. As briefly mentioned in the previous paragraph, experimental temperatures are in the range (marginally

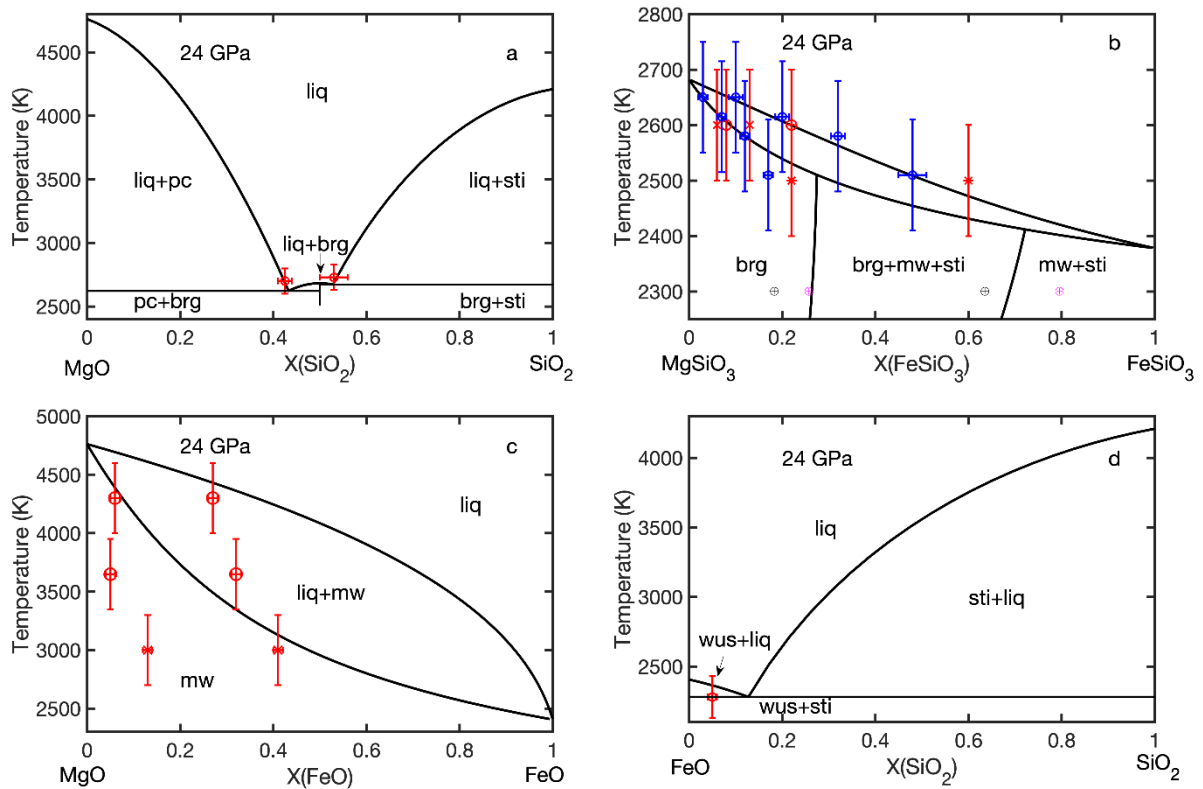


Figure 6.6: Computed melting phase relations at 24 GPa in the FeO-MgO-SiO₂ system along the binary joins. (a) For the MgO-SiO₂ join, the eutectic locations are consistent with previous multi anvil experiments (Liebske and Frost, 2012; Figure 5.3). (b) For the MgSiO₃-FeSiO₃ join, the thermodynamic model reproduces the coexisting solid and liquid compositions from our experiments (blue symbols), red symbols show the coexisting liquid and solid compositions from Liebske et al. (2005), for peridotite plus Fe metal (circles), CI chondritic analogue (asterisks), and an Al-rich peridotite (crosses). The computed solid phase boundaries are compared with the experimental data by Tange et al. (2009) with black circles at 22 GPa and magenta circles at 27 GPa. (c) For the MgO-FeO join, the phase relations are calculated with ideal mixing and compared with data by Du and Lee (2014) (red circles) and Deng and Lee (2017) (red crosses) at 27 GPa. (d) Computed FeO-SiO₂ system, in comparison to the eutectic location from Kato et al. (2016) at 27 GPa. Abbreviations are pc for periclase, brg for bridgmanite, sti for stishovite, wus for wüstite and liq for the liquid.

higher) of the liquidus T determined in our model (Figure 6.6) which decreases at a rate of 3-4 K per mol% FeSiO₃. At 24 GPa, we model a solidus T of 2590 K for (Mg_{0.9}Fe_{0.1})SiO₃, 50 K lower than the liquidus and 90 K below MgSiO₃ melting. This T difference between the solidus and liquidus is in reasonable agreement with that of Boukaré et al. (2015) (~ 70 K), although their solidus T (2760 K) is larger by more than 150 K than our model estimates. Nomura et al. (2011) reported a solidus T of 2600 K for (Mg_{0.89}Fe_{0.11})₂SiO₄ at 32 GPa which – with the Mg₂SiO₄ solidus providing a lower bound on MgSiO₃ melting (Figure 5.2) – can be seen as supporting a low solidus T , in general agreement with our data and model.

Melting phase relations in the FeO-MgO-SiO₂ system at 24 GPa based on our model are computed along four binary joins, MgO-SiO₂, MgSiO₃-FeSiO₃, MgO-FeO and FeO-SiO₂ (Figure 6.6) by solving equations 4.16, 4.22, 4.23, 4.28 and 4.29.

As we have discussed in Chapter 5 (Figure 5.2), the topology of the MgO-SiO₂ phase diagram is controlled by five points: MgO, SiO₂ and MgSiO₃ melting temperature, and two eutectic points (T and composition). For MgO and SiO₂, the endmember T_m are the same as in the model presented in Chapter 5, 4760 K for MgO and 4210 K for SiO₂ (Figures 5.2 and 6.6a). With the modified interaction parameters, T_m of MgSiO₃ bridgmanite is predicted at 2690 K, slightly lower than that presented in Chapter 5 with 2750 ± 120 K, but within the uncertainties. This difference can be traced to the larger absolute value of the Margules interaction parameter $W_{\text{MgO-SiO}_2}$ in the FeO-MgO-SiO₂ model (equation 6.1) compared to that in the MgO-SiO₂ system (equation 5.1). Consistently, the difference in $W_{\text{MgO-SiO}_2}$ leads to slightly lower $T_e = 2620$ K at $X_{\text{SiO}_2} = 0.43$ and $T_e = 2670$ K at $X_{\text{SiO}_2} = 0.53$ (Figures 5.2 and 6.6a), compared to the MgO-SiO₂ model presented in Chapter 5; eutectic compositions are not affected by the small difference in mixing parameters.

Along the MgSiO₃-FeSiO₃ join (Figure 6.6b), the solidus and liquidus curves are well constrained by our measured bridgmanite and liquid compositions (Table 6.1). The model predicts $T_m = 2690$ K for MgSiO₃, and $T_m = 2350$ K for the fictitious FeSiO₃, slightly higher than the 2250 K reported by Boukaré et al. (2015) and 2190 ± 150 K by Kato et al. (2016). The solidus curve between these two points shows significant convexity, while the liquidus T decreases quasi-linearly with FeSiO₃ content with a rate of a little less than 4 K per mol% of FeSiO₃ up to $X_{\text{FeSiO}_3} \sim 0.5$, before the curve also becomes slightly convex. The largest difference between the solidus and liquidus occurs at $X_{\text{FeSiO}_3} = 0.30$ with 80 K. The FeSiO₃ content in bridgmanite and the liquid from melting experiments by Liebske et al. (2005) on peridotite plus 30 wt% iron metal is in very good, on a chondrite starting composition in reasonable agreement with our model, indicating that their small CaO and Al₂O₃ contents ($\lesssim 4$ wt%) do not influence iron partitioning strongly. By contrast, for a composition with ~ 7 wt% Al₂O₃, the liquid is depleted in FeSiO₃ compared to our model, probably caused by the charge-coupled substitution $\text{Mg}^{2+} + \text{Si}^{4+} = \text{Al}^{3+} + \text{Fe}^{3+}$ shifting the iron equilibrium towards bridgmanite (Hummer and Fei, 2012; Liu et al., 2016). For $X_{\text{FeSiO}_3} < 0.27$ the phase predicted on the solidus is bridgmanite, where it exceeds its FeSiO₃ solubility limit in the

model, a value somewhat larger than that determined in the experiments for $(\text{Mg}_{0.5}\text{Fe}_{0.5})\text{SiO}_3$ directly ($X_{\text{FeSiO}_3} = 0.16 \pm 0.02$), and the phase assemblage at the solidus becomes bridgmanite, magnesiowüstite and stishovite. For $X_{\text{FeSiO}_3} = 0.72$, the phase assemblage on the solidus becomes magnesiowüstite and stishovite in our model. The predicted boundaries of the solidus assemblages bracket the measurements of Tange et al. (2009) at 2270 K for 22 and 27 GPa semi-quantitatively, further validating the adjustments of thermodynamic parameters for SiO_2 stishovite discussed in Chapter 5. The higher saturation X_{FeSiO_3} for bridgmanite predicted in the model compared to the experimental data may be due to the assumption of ideal mixing between MgSiO_3 and FeSiO_3 bridgmanite.

For the $(\text{Mg}_{0.5}\text{Fe}_{0.5})\text{SiO}_3$ starting composition we directly observe the coexistence of bridgmanite and magnesiowüstite in the experimental charge (Figure 6.2) which allows us to also compute the equilibrium constant for Fe distribution $K_D^{\text{brg/mw}} = (\text{Fe}^{\text{brg}}/\text{Mg}^{\text{brg}})(\text{Mg}^{\text{mw}}/\text{Fe}^{\text{mw}})$ between these two phases and compare to the model prediction and other experiments. While the bridgmanite composition can be determined directly from EPMA (Table 6.1), the small size of the magnesiowüstite grains (in some cases $<1 \mu\text{m}$) in the solid assemblage (Figure 6.2) requires that the composition of the surrounding bridgmanite is subtracted from the EPMA data obtained with a beam diameter of $1 \mu\text{m}$. We approximate this correction by subtracting the SiO_2 content from magnesiowüstite spots. With a FeO-rich magnesiowüstite composition (FeO and MgO content of 0.849 ± 0.041 and 0.151 ± 0.049 in molar fraction, respectively), $K_D^{\text{brg/mw}} = 0.04 \pm 0.01$ at 24 GPa and 2510 ± 100 K. Using the same starting composition, Tange et al. (2009) report values of $K_D^{\text{brg/mw}}$ in the range of 0.1 at 22-27 GPa and ~ 2270 K, slightly higher than our value. This difference can be explained by the effect of T : $K_D^{\text{brg/mw}}$ in Tange et al. (2009) decreases from 0.2 to 0.1 as T increases from 1670 K to 2270 K, the latter still significantly lower than T in our experiment. Our model predicts $K_D^{\text{brg/mw}} = 0.13$ at the triple point, somewhat higher than the direct experimental estimate, again likely caused by the ideal mixing between MgSiO_3 and FeSiO_3 in the bridgmanite solution model.

In the MgO-FeO system at 24 GPa the solidus and liquidus lines hinge on the melting temperatures of MgO (4760 K) and FeO (2410 K), and show a strongly convex and mildly concave shape, respectively. This morphology differs significantly from previous

descriptions of the MgO-FeO melting relations (Du and Lee, 2014; Deng and Lee, 2017; Miyazaki and Korenaga, 2019; Deng et al., 2019). For a bulk composition of $\text{Mg}_{0.91}\text{Fe}_{0.09}\text{O}$ and 4300 K – T of the experiments in Du and Lee (2014) on this composition –, our model yields $X_{\text{FeO}}^{\text{solid}} = 0.08$ and $X_{\text{FeO}}^{\text{liquid}} = 0.36$, in reasonable agreement with their data ($X_{\text{FeO}}^{\text{solid}} = 0.06 \pm 0.01$ and $X_{\text{FeO}}^{\text{liquid}} = 0.27 \pm 0.01$). Partition data from melting experiments for magnesiowüstite with higher FeO content by Du and Lee (2014) and Deng and Lee (2017) at 27 GPa suggest very little T dependence, in contrast to our model prediction (Figure 6.6c). The MgO-FeO melting relations continue to be a topic of ongoing debate (Fu et al., 2018; Deng et al., 2019) due to conflicting data at higher P from Fu et al. (2018), on the one hand, and Du and Lee (2014) and Deng and Lee (2017), on the other hand. As Deng et al. (2019) point out, differences between these model descriptions of MgO-FeO melting can be traced to the enthalpy change at melting (ΔH^m) for the endmembers, determining the degree of convexity of the computed liquidus curves. $\Delta H_{\text{FeO}}^m > \Delta H_{\text{MgO}}^m$ in both models, by a factor of ~ 2 for Fu et al. (2018) and a factor of ~ 3 for Deng et al. (2019), the latter showing a steep decrease in liquidus T with FeO content, matching the data by Du and Lee (2014) and Deng and Lee (2017). By contrast, in our model $\Delta H_{\text{FeO}}^m \approx \Delta H_{\text{MgO}}^m$ which leads to the concave shape of the liquidus curve. As our thermodynamic description of liquid FeO (Section 6.3) is based on the melting curve of Fu et al. (2018), ΔH_{FeO}^m is similar, and we may need to reconsider the thermodynamic description for MgO that we adapted from de Koker et al. (2013) as described in Chapter 5.

The FeO-SiO₂ system is characterized by T_m of the endmembers, already discussed in the previous paragraphs, and a eutectic at which the solid phase coexisting with the liquid switches from wüstite to stishovite. These two solid phases also constitute the sub-solidus assemblage over the whole composition range. With T_m of SiO₂ significantly larger than that of FeO and a relatively small absolute interaction parameter for this join (equation 6.2), the eutectic composition is close to the FeO member, at T not much below FeO melting. Our model predicts $X_{\text{SiO}_2} = 0.13$ and $T_e = 2280$ K, the temperature in good agreement with measurements by Kato et al. (2016) in the DAC at 26 GPa; their $X_{\text{SiO}_2} = 0.05$, however, is significantly smaller. This difference in eutectic composition may be due to the heterogeneity in the small sample recovered from DAC experiments or the thermodynamic mixing properties in the FeO-SiO₂ system that are not captured by our model which is based on mixing along the MgSiO₃-FeSiO₃ join.

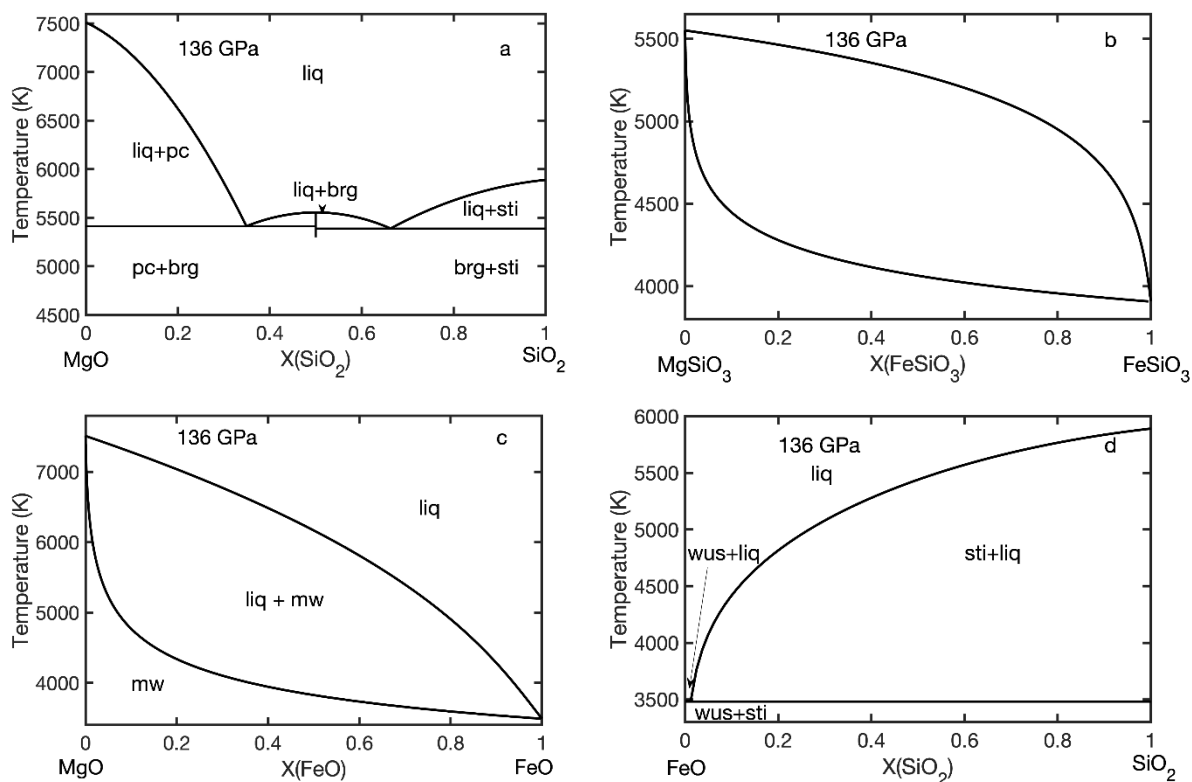


Figure 6.7: Melting phase relations in the MgO-FeO-SiO₂ system from our model along binary joins at 136 GPa: (a) MgO-SiO₂, (b) MgSiO₃-FeSiO₃, (c) MgO-FeO and (d) FeO-SiO₂. Abbreviations are pc for periclase, brg for bridgmanite, st for stishovite, wus for wüstite and liq for the liquid.

6.5 Iron partitioning and FeO-MgO-SiO₂ melting phase relations at CMB

Evaluating our thermodynamic model at CMB P leads to the melting relations along the four binaries shown in Figure 6.7. Predictions for the MgO-SiO₂ join are consistent with those shown in Figure 5.2, characterized by the large difference in T_m between MgO (7510 K) and SiO₂ (5891 K).

In the MgSiO₃-FeSiO₃ system, the phase loop between the solidus and liquidus expands significantly compared to 24 GPa, and the liquidus curve shows a concave character. This is partly caused by the significantly larger difference in T_m (1640 K) between MgSiO₃ (5550 K) and FeSiO₃ (3910 K) at CMB P compared to 330 K at 24 GPa. In contrast to Figure 6.6b, we refrain from computing the coexisting solid assemblage as their energetics and properties may not extrapolate well to these high T and P . For (Mg_{0.88}Fe_{0.12})SiO₃, representing a pyrolite FeO/MgO ratio (Table 1.1), the liquidus and solidus are 5510 K and 4400 K, respectively. While the solidus is in reasonable agreement with 4150 ± 150 K determined for a chondritic

mantle composition by Andrault et al. (2011) in DAC experiments, their liquidus T (4730 ± 150 K) is significantly lower. Our high liquidus T directly follows from the high T_m of MgSiO_3 bridgmanite and the shape of the liquidus curve. At melting, the equilibrium constant K_D for a $(\text{Mg}_{0.88}\text{Fe}_{0.12})\text{SiO}_3$ composition is in the range of 0.01-0.02, in general agreement with predictions from the model of Boukaré et al. (2015) ($K_D \sim 0.05$), as well as with DAC experiments on peridotite by Nomura et al. (2011) with $K_D = 0.08 \pm 0.02$ at 143 GPa and Tateno et al. (2014) with $K_D = 0.04 \pm 0.01$ at 169 GPa. The model of Miyazaki and Korenaga (2018), by contrast, predicts $K_D \sim 0.2$ at the solidus, significantly larger than the other work, and their K_D decreases by two orders magnitude between the solidus and liquidus; unfortunately, they do not show a MgSiO_3 - FeSiO_3 phase diagram that would help to better understand such behavior. The value for the partition coefficient of iron between the solid and the liquid, $D_{\text{Fe}} \sim 0.015$, in our model is significantly smaller than $D_{\text{Fe}} = 0.47 \pm 0.09$ at 110 GPa reported by Andrault et al. (2012) for a pyrolite composition, a difference that may be caused by an enhanced Fe incorporation into bridgmanite in the presence of Al_2O_3 in the starting composition (Wood and Rubie, 1996; Liebske et al., 2005) or changes in the SiO_2 content of the liquid phase. In both our experiments and the model (Figures 6.3 and 6.5), we observe that the SiO_2 content in the liquid and K_D are positively correlated (Figure 6.3 and 6.5). Interestingly, the SiO_2 content of 63.2 wt% at ~ 80 GPa reported by Andrault et al. (2012) is much larger than those by Nomura et al. (2011) and Tateno et al. (2014) with ~ 38 wt%, all for pyrolite. Also, as the magma ocean evolves in terms of SiO_2 content during crystallization, K_D likely changes, leading to an increased FeO content of the crystallizing minerals.

For the FeO-MgO join at 136 GPa, endmember T_m are computed as 3490 K and 7510 K, respectively. For a $\text{Mg}_{0.8}\text{Fe}_{0.2}\text{O}$ solid composition our model predicts a solidus T of 4360 K, and partitioning of FeO between the melt and solid of $D_{\text{Fe}} = 4.58$, somewhat higher than measured by Fu et al. (2018) in a DAC sample with $D_{\text{Fe}} = 3.6 \pm 0.2$. The difference may arise from the extrapolation of our thermodynamic parameters beyond the high-spin to low-spin transition in ferropiclasite (Lin et al., 2007; Lin et al., 2013) or changes in the enthalpy of melting (ΔH^m) with P (Deng and Lee, 2019; Fu et al., 2018). The role of the spin transition on D_{Fe} remains highly controversial between various studies (Ghosh and Karki, 2016; Fu et al., 2018), and it is difficult to assess its potential influence on the extrapolation of our low P model to lowermost mantle conditions.

Along the FeO-SiO₂ join, the difference between the endmember T_m becomes large (2400 K), shifting the eutectic location to $X_{\text{SiO}_2} = 0.01$ with $T_e = 3480$ K, barely below FeO melting. These values are very close to the data of Kato et al. (2016) at 123 GPa with $X_{\text{SiO}_2} = 0.01$ and $T_e \sim 3500$ K.

6.6 Summary and implications

We have performed multi-anvil melting experiments at 24 GPa to establish melting relations in the (Mg_{1-x}Fe_x)SiO₃ system with starting compositions $x=0.1, 0.2, 0.3$ and 0.5 . The presence of a multiphase assemblage for the For (Mg_{0.5}Fe_{0.5})SiO₃ experiments, in contrast to bridgmanite for smaller x , shows that the solubility limit for FeSiO₃ in bridgmanite has been exceeded in this experiment. Iron generally partitions strongly into the liquid, with the equilibrium constant between the solid and the liquid decreasing with Fe content from $K_D = 0.35$ at $x=0.1$ to $K_D = 0.2$ for $x=0.5$.

The experimentally determined composition of the coexisting solid and the liquid along the MgSiO₃-FeSiO₃ join are combined with thermodynamic descriptions of liquid and solid endmembers in the FeO-MgO-SiO₂ system to develop a model of melting relations. Our model matches well with available experimental data of phase boundaries for the MgSiO₃-FeSiO₃, MgO-SiO₂ and FeO-SiO₂ joins at 24 GPa. For the MgO-FeO solution, however, phase relations differ from previous experimental measurements, and this system continues to be the subject of vigorous debate. At 24 GPa, FeO partitioning in the FeO-MgO-SiO₂ system between the liquid and coexisting bridgmanite is in good agreement with model peridotites (Corgne et al., 2005; Liebske et al., 2005; Boukaré et al., 2015), but more Al₂O₃-rich compositions show different behavior (Liebske et al., 2005; Trønnes and Frost, 2002).

While for the MgO-SiO₂ system (Chapter 5) we relied on previously established thermodynamic models for the liquid and solid endmembers from de Koker et al. (2013), the addition of FeO requires thermodynamic descriptions for the FeSiO₃ and FeO solid and the FeO liquid. The former two we take from the Mie-Grüneisen Birch-Murnaghan description of Stixrude and Lithgow-Bertelloni (2005) and Fischer et al. (2011), respectively. By matching the FeO melting curve using the data by Lindsley (1966) and Fu et al. (2018) we determine thermodynamic parameters of FeO liquid in the formulation of de Koker et al. (2013).

As for the model in the MgO-SiO₂ system with experiments only performed at 24 GPa, P dependence hinges on the T -dependent interaction parameters (equations 6.1 and 6.2) and the melting curves of the endmembers. We extrapolate our model to P of the CMB, and predict a solidus T of 4400 K in the bridgmanite solid solution with a pyrolite FeO/MgO ratio. This T is significantly higher than most typical models of the mantle geotherm (Figure 2.3) (Anzellini et al., 2013; Chust et al., 2017; Hernlund et al., 2005; Stacey and Davies, 2008). More Fe-enriched reservoirs – which have been proposed as potential sources for the ULVZ in D'' (Nomura et al., 2011; Boukaré et al., 2015; Kato et al., 2016; Fu et al., 2018) – are predicted to melt partially at T below 4000 K, at the upper end of typical geotherms.

During fractional crystallization of the Earth's mantle from a magma ocean, FeO is partitioned into the liquid which results in an increase of the density of the melt. This could eventually lead to a density crossover at some stage of its evolution, i.e., the coexisting liquid becomes denser than the crystallizing solid. This can result in a dense basal magma ocean as proposed by Labrosse et al. (2007) which would be difficult to mix into the mantle by convection (Ballmer et al., 2017; Laneuville et al., 2018). The presence of ULVZ or LLVSZ in the lowermost mantle could signify remnants of this layer being stable to the present.

7. Density of Fe-bearing silicate melts at mantle conditions

Understanding melt properties at high pressure is of critical importance for magma ocean processes in the early Earth; especially the density contrast between melt and coexisting solids (forming, e.g., at the liquidus) determines its dynamics and crystallization (Labrosse et al., 2007; Ballmer et al., 2017). Solidifying material univariantly leads to a denser solid than the liquid, but for multivariant phase transitions, element partitioning between the liquid and the solid can counteract – or enhance – the density difference. With FeO partitioning into the melt in silicate systems as discussed in Chapter 6, the density difference between the magma ocean liquid and the solid crystallizing from it will be smaller than between a liquid and solid of the same composition, and may even result in a density crossover between the coexisting liquid and solid (Nomura et al., 2011; Karki et al., 2018) which would favor the formation of a stable basal magma ocean. This density inversion may be caused by differences in molar weight and volume, two contributions that are difficult to disentangle in experiments, but DFT-MD simulations can provide direct insight into these competing factors. As we already discussed in Chapter 6, the high-spin (HS) to low-spin (LS) transition in FeO-bearing minerals and melts further complicates the understanding of their physical behavior, including partitioning at lowermost mantle P , and potential non-linear effects on molar volume and compressibility (Muñoz Ramo and Stixrude, 2014; Ghosh and Karki, 2020).

Using glass as an analogue for silicate melts (*cf.* Chapter 8), a number of DAC experiments (Mao et al., 2014; Prescher et al., 2014; Dorfman et al., 2016; Solomatova et al., 2017) show that ferrous iron stays in a HS state at P throughout Earth's lower mantle, and the local environment of iron changes gradually with an increase in coordination number. For a Al-bearing silicate glass with composition $\text{Mg}_{0.79}\text{Fe}_{0.10}\text{Al}_{0.10}\text{Si}_{0.96}\text{O}_3$ (containing both Fe^{3+} and Fe^{2+}), Mao et al. (2014) reported $CN_{\text{FeO}} \sim 4$ at ambient condition, and coordination to continually increases to $CN_{\text{FeO}} \sim 8$ at 120 GPa. However, the abrupt change in FeO partitioning behavior in peridotite between liquid and solid reported by DAC studies at ~ 70 GPa (Figure 2.2) (Nomura et al., 2011; Tateno et al., 2014) suggests a significant change in the physical environment for Fe in the liquid at these conditions, and a HS-LS transition of iron in the liquid provides a possible mechanism.

Ab initio simulations on Fe-bearing silicates – either for the pure Fe-endmembers (Muñoz Ramo and Stixrude 2014; Sun et al., 2018) or for Fe-bearing compositions based on MgSiO_3

(Karki et al., 2018) show a HS to LS transition of iron in silicate melt over a broad P interval, but whether such a transition is relevant at P of the Earth's lower mantle remains unclear. Similarly, a recent comparison of the coordination number CN_{FeO} for HS and LS as well as Fe^{2+} and Fe^{3+} in Fe-bearing MgSiO_3 melts (Ghosh and Karki, 2020) reiterates the connection between the iron spin state and local Fe-O structure, especially in comparison to that of Mg-O. This warrants further investigation, and here we perform DFT-MD simulations on both Fe-bearing and Fe-free silicate melts based on an olivine stoichiometry in a supercell of 112 atoms, $16 \cdot \text{Mg}_2\text{SiO}_4$ and $14 \cdot \text{Mg}_2\text{SiO}_4 + 2 \cdot \text{Fe}_2\text{SiO}_4$, the latter corresponding to $(\text{Mg}_{0.875}\text{Fe}_{0.125})_2\text{SiO}_4$, at 3000 K over a wide compression range. The reference volume of the simulation cell size is $V_0 = 1391.2 \text{ \AA}^3$ ($52.36 \text{ cm}^3/\text{mol}$), and we perform simulations at V_X with $V_X/V_0 = 1.0, 0.8, 0.7, 0.6, 0.5$ and 0.4 , covering a P range from 0 GPa to more than 350 GPa. All simulations are performed for at least 8 ps after equilibrium, with a time step of 1 fs.

7.1 P - V - T equation of state and magnetic state

In our simulations, we find that iron stays in a HS state in the FeO-bearing olivine $(\text{Mg}_{0.875}\text{Fe}_{0.125})_2\text{SiO}_4$ for volumes in the range 52.36 to $36.65 \text{ cm}^3/\text{mol}$ (0 to 35 GPa) with an average magnetic moment of $4.0 \pm 0.1 \mu_B$ (Figure 7.1), calculated from the root mean square of the individual moments. This value obtained with the GGA+U method (Section 3.2.3) corresponds to the formal value from the electronic configuration of ionic Fe^{2+} with 4 unpaired 3d electrons. The value obtained here is somewhat higher than that in the Fe_2SiO_4 liquid determined by Muñoz Ramo and Stixrude (2014) with $3.7 \pm 0.4 \mu_B$, with larger $U = 4.75 \text{ eV}$ compared to $U = 3 \text{ eV}$ in our work. For the smaller volumes, the mean magnetic moments for iron decrease quasi-linearly with compression, reaching a value of $0.5 \pm 0.4 \mu_B$ at $20.95 \text{ cm}^3/\text{mol}$ ($\sim 370 \text{ GPa}$), i.e., the iron atoms are then predominantly in the low-spin state. Uncertainties at the two intermediate volumes, corresponding to 80 and 170 GPa are large ($\pm 0.9 \mu_B$), due to the strongly fluctuating magnetic moments on and differences between individual iron atoms. The decrease in magnetic moments with compression we observe is significantly faster than that described by Muñoz Ramo and Stixrude (2014) in their GGA+U results for Fe_2SiO_4 . Both their lower magnetic moment at large volume and the slower decay with compression is likely caused by the larger indirect magnetic exchange coupling between Fe atoms (Jiang and Guo, 2004) in Fe_2SiO_4 . It is interesting to note here that the drop in the iron partitioning coefficient observed in DAC melting experiments ~ 70

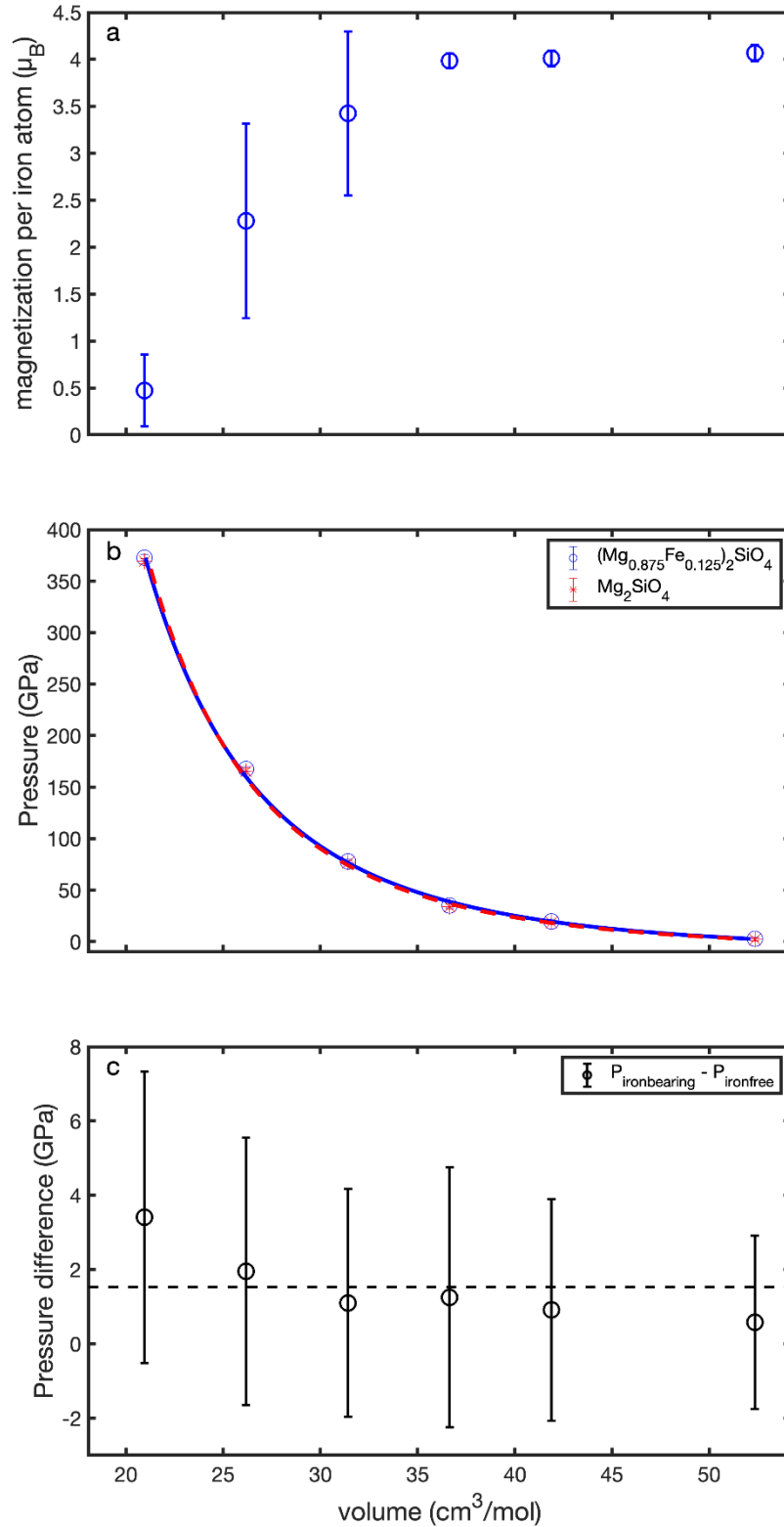


Figure 7.1: Upper panel: Magnetization in Bohr magnetons (μ_B) per iron atom as a function of molar volume at 3000 K for $14 \cdot \text{Mg}_2\text{SiO}_4 + 2 \cdot \text{Fe}_2\text{SiO}_4$, representing a $(\text{Mg}_{0.875}\text{Fe}_{0.125})_2\text{SiO}_4$ composition. Vertical bars represent the fluctuations of magnetic moment per atom. Middle panel: Calculated and fitted P-V equation of state at 3000 K for $(\text{Mg}_{0.875}\text{Fe}_{0.125})_2\text{SiO}_4$ (blue) and Mg_2SiO_4 (red). Lower panel: Pressure difference (black circle) between iron bearing and iron free simulations at different volumes with the average shown by the dashed line. Vertical bars represent the standard deviation from fluctuations in the molecular dynamic simulations.

Table 7.1: Fitted Tait equation of state parameters in iron bearing $(\text{Mg}_{0.875}\text{Fe}_{0.125})_2\text{SiO}_4$ and iron-free olivine liquid at 3000 K, compared with results from de Koker et al. (2008) for forsterite composition, and the chemical melt model of Lange and Carmichael (1987) at significantly lower T . V_0 is the equilibrium volume, K_0 the bulk modulus at zero pressure and K'_0 its pressure derivative.

	V_0 (cm ³ /mol)	K_0 (GPa)	K'_0
$(\text{Mg}_{0.875}\text{Fe}_{0.125})_2\text{SiO}_4$	55.3	40	3.7
Mg_2SiO_4 (This study)	55.0	38	3.8
Mg_2SiO_4 (dK08)	57.8	19	6.2
Mg_2SiO_4 (LC87, 2163 K)	52.4	12	-
$(\text{Mg}_{0.875}\text{Fe}_{0.125})_2\text{SiO}_4$ (LC87, 2163 K)	53.0	13	-

GPa (Nomura et al., 2011; Tateno et al., 2014), already discussed in Chapters 2 and 6, correlates with the onset of magnetic moment loss and the associated strong fluctuations.

As a closed fit of the isothermal P - V results for $(\text{Mg}_{0.875}\text{Fe}_{0.125})_2\text{SiO}_4$ obtained from DFT-MD is not possible in a satisfactory way using the Birch-Murnaghan equation of state (equation 4.1) due to the increasing deviations from the finite strain expression at the smallest volumes, we use the Tait equation of state (equation 4.10) to fit the results instead (Figure 7.1), with $\chi^2 = 0.767$. Differences between $(\text{Mg}_{0.875}\text{Fe}_{0.125})_2\text{SiO}_4$ and Mg_2SiO_4 in terms of P - V are small (1.5 GPa on average, and zero within the margin of error) and show a negligible volume dependence. This is also represented in the fit parameters (Table 7.1), with only a marginally larger zero-pressure volume (V_0) and corresponding bulk modulus (K_0) for $(\text{Mg}_{0.875}\text{Fe}_{0.125})_2\text{SiO}_4$ compared to Mg_2SiO_4 . While absolute values of V_0 and K_0 for $(\text{Mg}_{0.875}\text{Fe}_{0.125})_2\text{SiO}_4$ compared to Mg_2SiO_4 differ between our values and those of the global melt model of Lange and Carmichael (1987), not only because of T , they consistently predict slightly larger V_0 and K_0 for the Fe-bearing olivine composition. The negligible difference of computed P at the same volume for $(\text{Mg}_{0.875}\text{Fe}_{0.125})_2\text{SiO}_4$ and Mg_2SiO_4 – which can be interpreted as “chemical pressure” (Fournier, 1993; Muñoz Ramo and Stixrude, 2014) – over the whole compression range indicate that the partial molar volumes of MgO and FeO do not differ in the olivine liquid, at least to a molar Fe_2SiO_4 content of 0.125, and is irrespective of the spin state.

7.2 Melt structure under high pressure

Figure 7.2 shows the partial radial distribution functions $g(r)$ for Mg-O and Fe-O in the $14 \cdot \text{Mg}_2\text{SiO}_4 + 2 \cdot \text{Fe}_2\text{SiO}_4$ cell at large and small molar volume, representing low and high P , respectively. Due to the smaller number of Fe atoms in the cells, $g_{\text{Fe-O}}(r)$ shows

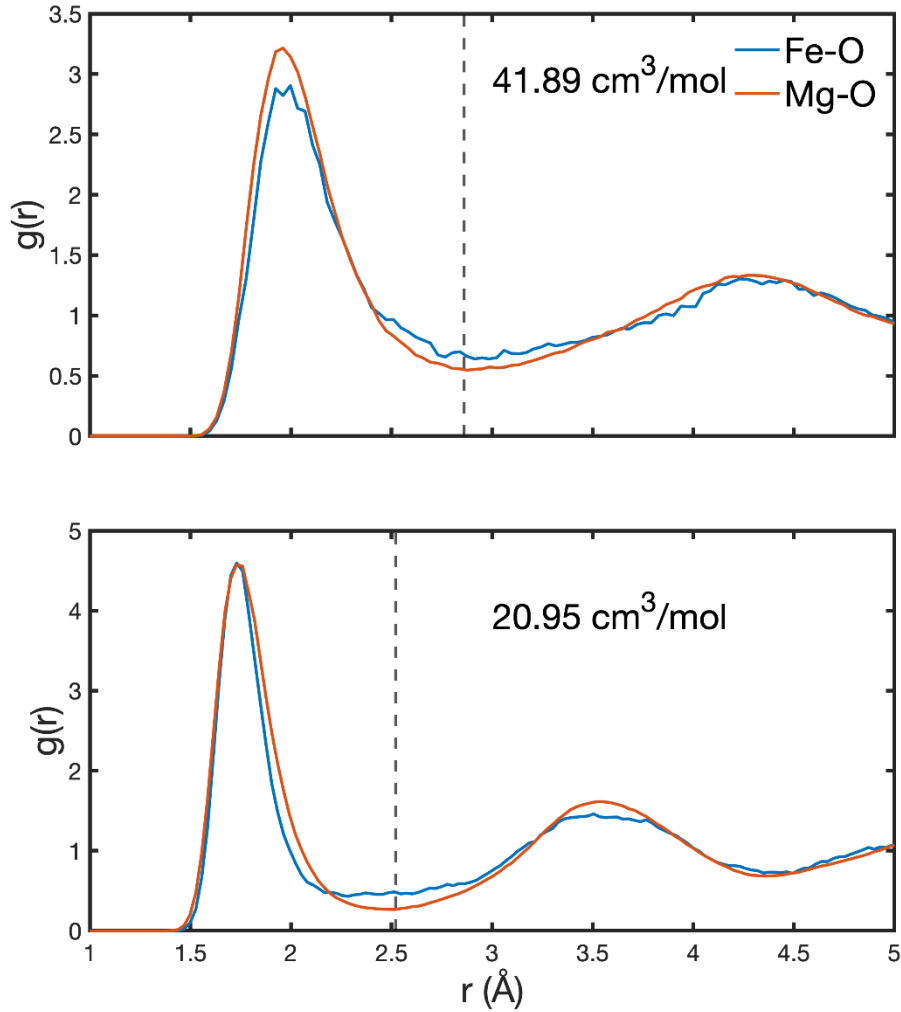


Figure 7.2: Fe-O and Mg-O radial distribution functions for liquid composition $(\text{Mg}_{0.875}\text{Fe}_{0.125})_2\text{SiO}_4$ at $41.89 \text{ cm}^3/\text{mol}$ ($\sim 20 \text{ GPa}$) and $20.95 \text{ cm}^3/\text{mol}$ ($\sim 370 \text{ GPa}$) and 3000 K . The blue curve represents Fe-O and the red Mg-O. The vertical dashed lines show the first minimum in $g(r)$ for Mg-O, 2.88 \AA and 2.52 \AA for $41.89 \text{ cm}^3/\text{mol}$ and $20.95 \text{ cm}^3/\text{mol}$, respectively.

significantly larger scatter than $g_{\text{Mg-O}}(r)$, and both maxima and minima are less well defined. $g_{\text{Mg-O}}(r)$ between the Fe-bearing and Fe-free compositions are identical (not shown). For $41.89 \text{ cm}^3/\text{mol}$ (20 GPa), the principal peak for the Mg-O and Fe-O radial distributions occurs at 1.95 \AA and – using the location of the first minimum to delineate the first coordination shell – $CN_{\text{FeO}} = 6.2$ and $CN_{\text{MgO}} = 6.3$, virtually identical. At twofold compression, our smallest volume with $20.95 \text{ cm}^3/\text{mol}$ (370 GPa), the principal peak for $g_{\text{Mg-O}}(r)$ and $g_{\text{Fe-O}}(r)$ and is still identical (1.73 \AA), but at larger r , the Fe-O distribution deviates significantly from that of Mg-O: For Fe-O it decreases more rapidly, and no pronounced minimum occurs before the second coordination shell. If we take $r = 2.50 \text{ \AA}$ for the minimum in $g_{\text{Mg-O}}(r)$, $CN_{\text{FeO}} = 7.6$ is significantly smaller than $CN_{\text{MgO}} = 8.3$, reflecting the steeper decrease in $g_{\text{Fe-O}}(r)$. With a higher density of Fe-O distances for $2.20\text{-}3.25 \text{ \AA}$,

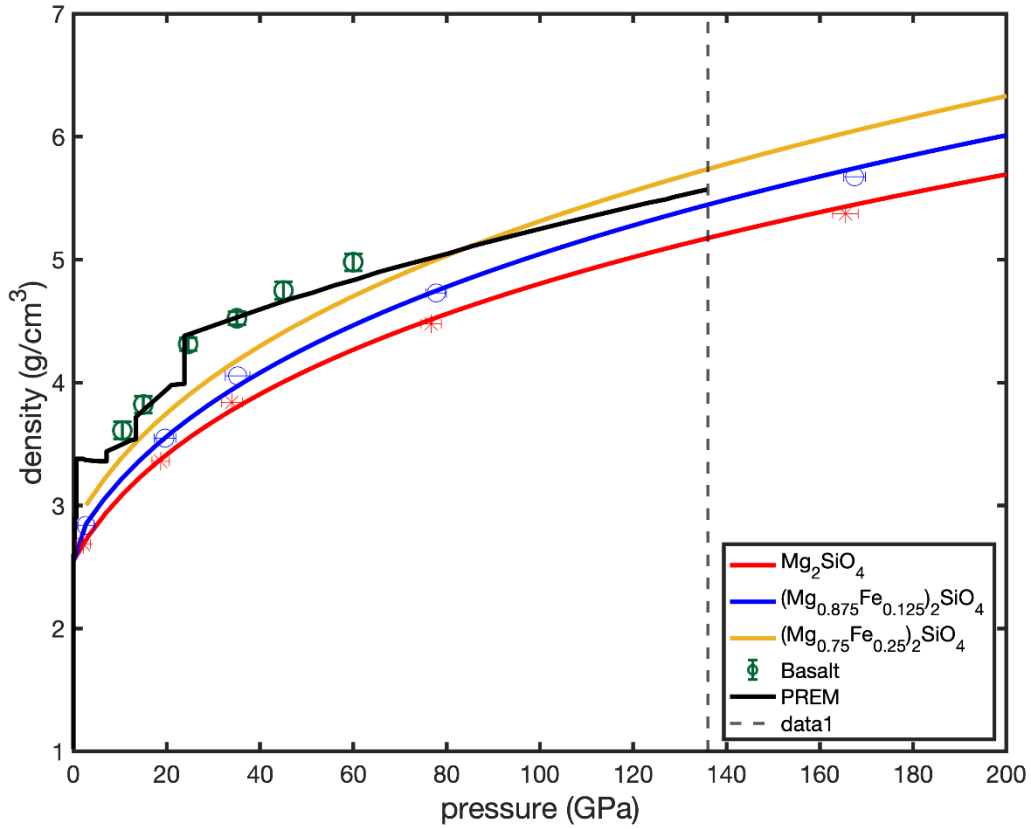


Figure 7.3: Density of $(\text{Mg}_{0.75}\text{Fe}_{0.25})_2\text{SiO}_4$, $(\text{Mg}_{0.875}\text{Fe}_{0.125})_2\text{SiO}_4$ and Mg_2SiO_4 melt from our simulations as a function of pressure along a 3000 K isotherm. Blue and red symbols are simulation results with the fit from the Tait equation of state as curves. The $(\text{Mg}_{0.75}\text{Fe}_{0.25})_2\text{SiO}_4$ curve (golden) is calculated assuming no volume change for FeO when increasing the FeO concentration. We compare to density measurements of basalt from Sanloup et al. (2013) (green points) in the T-range 2200-3300 K and the density profile of PREM (Dziewonski and Anderson, 1981). The vertical grey line indicates the pressure of the core-mantle boundary.

the coordination numbers become equal at 2.90 Å. This broad distribution of $g_{\text{Fe-O}}(r)$ surrounding the first minimum in $g_{\text{Mg-O}}(r)$ could be caused by spin fluctuations, with high spin Fe tending towards larger distances, but significant additional simulations for non-magnetic $14 \cdot \text{Mg}_2\text{SiO}_4 + 2 \cdot \text{Fe}_2\text{SiO}_4$ cells would be required to answer this question.

7.3 Density of melts under high pressure

With the pressure-volume equation of state for Mg_2SiO_4 and $(\text{Mg}_{0.875}\text{Fe}_{0.125})_2\text{SiO}_4$ liquid established, the density profile along an isotherm is constrained, and – under the assumption of a concentration independent molar volume of FeO – we can also readily compute a density profile for $(\text{Mg}_{0.75}\text{Fe}_{0.25})_2\text{SiO}_4$ (Figure 7.3). While most of the previous work has considered $(\text{Fe}_x\text{Mg}_{1-x})\text{SiO}_3$ (Karki et al., 2018; Caracas et al., 2019) – often even only an enstatite

composition (Akins et al., 2004; Petitgirard et al., 2015) – as a candidate for melting (including ourselves in the discussion of Chapter 6), our experiments in the MgO-SiO₂ system and related work on peridotite compositions (Nomura et al., 2011; Tateno et al., 2014) discussed in greater detail in Chapter 5 show that the eutectic composition is closer to an olivine composition, and olivine may therefore be more representative of partial melts formed in the lower mantle. Both forsterite and (Mg_{0.875}Fe_{0.125})₂SiO₄ melt have a lower density than PREM throughout the lower mantle which would make these melts buoyant compared to the solid mantle. However, with a higher fayalite content – explored here for (Mg_{0.75}Fe_{0.25})₂SiO₄ – the melt can reach higher densities, for $P > 85$ GPa. While these values are strictly valid for the 3000 K isotherm only, higher T along geotherm are expected to lead to a very small effect on density only (Karki et al., 2018). It is interesting to note that just atop the 410 km seismic discontinuity the estimated density of the (Mg_{0.75}Fe_{0.25})₂SiO₄ melt is also very similar to PREM. There, it is also similar in density to experiments on basalt at 10 GPa and 2200 K (Sanloup et al., 2013). Upon compression, the basaltic melt densifies significantly more strongly than the olivine, most likely caused by the coordination changes in the Si-O environment also supported by Sato and Funamori (2010), with basalt having a larger SiO₂ content (Table 1.1) compared to olivine.

7.4 Discussion and Conclusion

By comparing results from DFT-based molecular dynamics simulations for Mg₂SiO₄ and 14·Mg₂SiO₄ + 2·Fe₂SiO₄ liquids at 3000 K over a wide compression range, we show that the chemical pressure due to the addition of the fayalite component is negligible, strongly supporting the notion that the molar volume of FeO and MgO do not differ in olivine, at least up the fayalite concentration explored here (12.5 %mol). This is irrespective of the spin state of Fe that continually decreases starting at ~70 GPa, with is further supported by the local oxygen environment of Mg and Fe being very similar for much of the compression range. Only for the smallest volume considered, corresponding to a pressure exceeding 350 GPa, the Fe-O radial distribution function deviates significantly from that of Mg-O, with Fe coordination not as well defined as that of Mg. This may be related to different spin-states of Fe coexisting in the highly compressed liquid, leading to variable Fe-O distances, but further simulations would be required to confirm this hypothesis.

The onset of strong spin fluctuations and a decrease in average moment of the Fe atoms in

our simulations at ~ 70 GPa coincides with changes reported in Fe partitioning between bridgmanite and coexisting melt for experiments with a peridotite composition (Nomura et al., 2011; Tateno et al., 2014).

By extrapolating volume-composition relations from the two compositions considered explicitly to an olivine melt with 25 mol% of fayalite, we find that such a melt would be denser than the solid mantle at $P > 85$ GPa, i.e., deep in the mantle, and close to 10 GPa, the P just above the 410 km seismic discontinuity. For melting around the transition zone, typically volatiles are required (Gasparik, 1993) that also lower the solidus T such that partial melts will occur. These in turn would then also be volatile rich (Matsukage et al., 2005), leading to lower density that would then make these melts buoyant (Yuan et al., 2020), and therefore contribute to the low-velocity layer seismically observed above the 410 km seismic discontinuity (Tauzin et al., 2010).

However, during magma ocean crystallization, with large D_{Fe} , a dense basal magma ocean is possible (Section 6.6), with the high FeO content. As a high FeO content leads to a significant reduction in solidus T , partial melt may be present near the CMB and contribute to the ULVZ signature there (Kato et al., 2016; Fu et al., 2018).

8. Liquid and glass structure of Mg_2SiO_4 and MgSiO_3 from ab-initio simulations

Due to the high melting temperatures of silicates, and general experimental challenges in the study of melts at high pressure, many experiments use silicate glasses quenched from melts as analogues on melt structure (e.g., Benmore et al., 2011; Malfait et al., 2014; Lee et al., 2008; Wilding et al., 2004; Prescher et al., 2017). The extent of structural changes in the quench process with rates that generally do not exceed several 100 K/s (Posner et al., 2017) remains an open question in such studies and can potentially lead to differences in structural analysis and properties of melts and glass (Henderson et al., 2006; Stebbins, 2016). To characterize differences in the topology of MgSiO_3 and Mg_2SiO_4 melt and glass, we perform simulations at the same cell volumes V and therefore density ρ . Cells are setup with $V_{\text{ref}} = 11.86 \text{ \AA}^3/\text{atom}$ ($V_{\text{ref}} = 50.00 \text{ cm}^3/\text{mol}$ in Mg_2SiO_4 and $35.71 \text{ cm}^3/\text{mol}$ in MgSiO_3) ($\rho=2.8 \text{ g/cm}^3$) for both compositions, close to the density of vitreous MgSiO_3 ($\rho=2.77 \text{ g/cm}^3$) and Mg_2SiO_4 ($\rho=2.93 \text{ g/cm}^3$) (Leshner et al., 2009) which in turn are consistent with systematic consideration of the molar volumes for silicate liquids by Lange (1997) and Knoche et al. (1995) evaluated at the glass transition temperature (T_g) (Wilding et al., 2004b) of 1039 K for MgSiO_3 ($\rho=2.64\text{-}2.75 \text{ g/cm}^3$) and 1072 K for Mg_2SiO_4 ($\rho=2.89\text{-}3.04 \text{ g/cm}^3$); below T_g , the volume does not change further (Leshner et al., 2009; Moynihan, 1995). Cells are initially equilibrated at 6000 K and isochorically brought to 2000 K immediately (quenched) in order to investigate the melt structure near T_m . They are subsequently cooled to a glass at 300 K by different rates, keeping the cell volume constant. We present results for quench and a cooling rate of 0.1 K per MD step (i.e., 10^{14} K/s which we term “slow cooling”). At 2000 K we run the DFT-MD for at least 5 ps after initial equilibration of P , T and internal energy E to extract structural information; examining the mean-square displacement for all atoms at 2000 K we find all cells investigated to be in the liquid state. Similarly, for the glass structure at 300 K we perform DFT-MD simulations for at least 10 ps to obtain significantly improved statistics. During the cooling process one electronic optimization is performed for each time step.

The resulting Mg_2SiO_4 glass from the slow cooling process at $\rho=2.8 \text{ g/cm}^3$ is then compressed to $\rho=3.0 \text{ g/cm}^3$ ($V=46.92 \text{ cm}^3/\text{mol}$) and subsequently to $\rho=3.2 \text{ g/cm}^3$ ($V=43.97 \text{ cm}^3/\text{mol}$) (cold compression) to investigate the persistence of glass features under compression and to compare to the structure of high- P glass directly cooled from the liquid

(hot compression), similar to the approach and nomenclature of (Ghosh et al., 2014), but over a much narrower compression range.

8.1 Radial distribution functions

For $\rho=2.8 \text{ g/cm}^3$, both the forsterite and enstatite liquid at 2000 K are characterized by three peaks in $g_{\text{tot}}(r)$ (Figures 8.1): The principal peaks of $g_{\text{SiO}}(r)$ at $r=1.65 \text{ \AA}$, $g_{\text{MgO}}(r)$ at $r=1.99 \text{ \AA}$, and $g_{\text{OO}}(r)$ at $r=2.71 \text{ \AA}$. Due to the proportionally smaller number of Mg for MgSiO_3 enstatite (Figure 8.1d), the peak for $g_{\text{MgO}}(r)$ does not show prominently in $g_{\text{tot}}(r)$, it only appears as a low amplitude shoulder on the $g_{\text{SiO}}(r)$ peak which dominates $g_{\text{tot}}(r)$.

The same principal peak location for $g_{\text{SiO}}(r)$ in both forsterite and enstatite liquids reflects the stability of the SiO_4 -tetrahedra, and the peak at $r=1.65 \text{ \AA}$ falls in the experimental range of Si-O distances for forsterite (Smyth and Hazen, 1973) and enstatite (Morimoto and Koto, 1969) at ambient conditions (1.59-1.69 \AA , with an average of $1.64\pm 0.03 \text{ \AA}$). Liquid Mg-O and O-O distances in the melt are shorter than in the crystals, with values of $r_{\text{MgO}} = 2.11\pm 0.05 \text{ \AA}$ for both compositions and $r_{\text{OO}} = 2.86\pm 0.16 \text{ \AA}$ for MgSiO_3 and $r_{\text{OO}} = 2.96\pm 0.19 \text{ \AA}$ for Mg_2SiO_4 , respectively. It is further interesting to note that our results yield a slightly larger values of r for the principal peak in $g_{\text{SiO}}(r)$ than obtained by Karki (2010) for MgSiO_3 and de Koker et al. (2008) for Mg_2SiO_4 although their densities are smaller than the ones we used here, with 2.58 g/cm^3 for MgSiO_3 (Karki 2010) and 2.69 g/cm^3 (de Koker et al., 2008).

Principal peaks for $g_{\text{MgO}}(r)$ are consistent with the values of de Koker et al. (2008) for Mg_2SiO_4 at 3000 K and Karki (2010) for MgSiO_3 at 2500 K (both at 1.97 \AA). Similarly, the coordination number for Si and O ($CN_{\text{SiO}} = 4.1$) agrees with their values for enstatite and forsterite liquids; $CN_{\text{SiO}} = 1.0$ for Mg_2SiO_4 and $CN_{\text{SiO}} = 1.4$ for MgSiO_3 , the latter again consistent with values by Karki (2010). By contrast, the coordination of Mg and O differ significantly between the two compositions: For liquid Mg_2SiO_4 $CN_{\text{MgO}} = 5.2$ ($CN_{\text{OMg}} = 2.6$) and for MgSiO_3 at 2000 K they are $CN_{\text{MgO}} = 5.6$ ($CN_{\text{OMg}} = 1.9$) due to the smaller number of Mg in the composition), consistent with values in the previous study of de Koker et al. (2008) for Mg_2SiO_4 at 3000 K, but $CN_{\text{MgO}} = 5.6$ is somewhat larger for MgSiO_3 than values computed by Karki (2010) at 3000 K.

Quenching the liquid from 2000 K to 300 K leads to sharpening of the distributions – both in width and amplitude – in all $g_{\alpha\beta}(r)$ for both Mg_2SiO_4 and MgSiO_3 (Figures 8.1b and 8.1e),

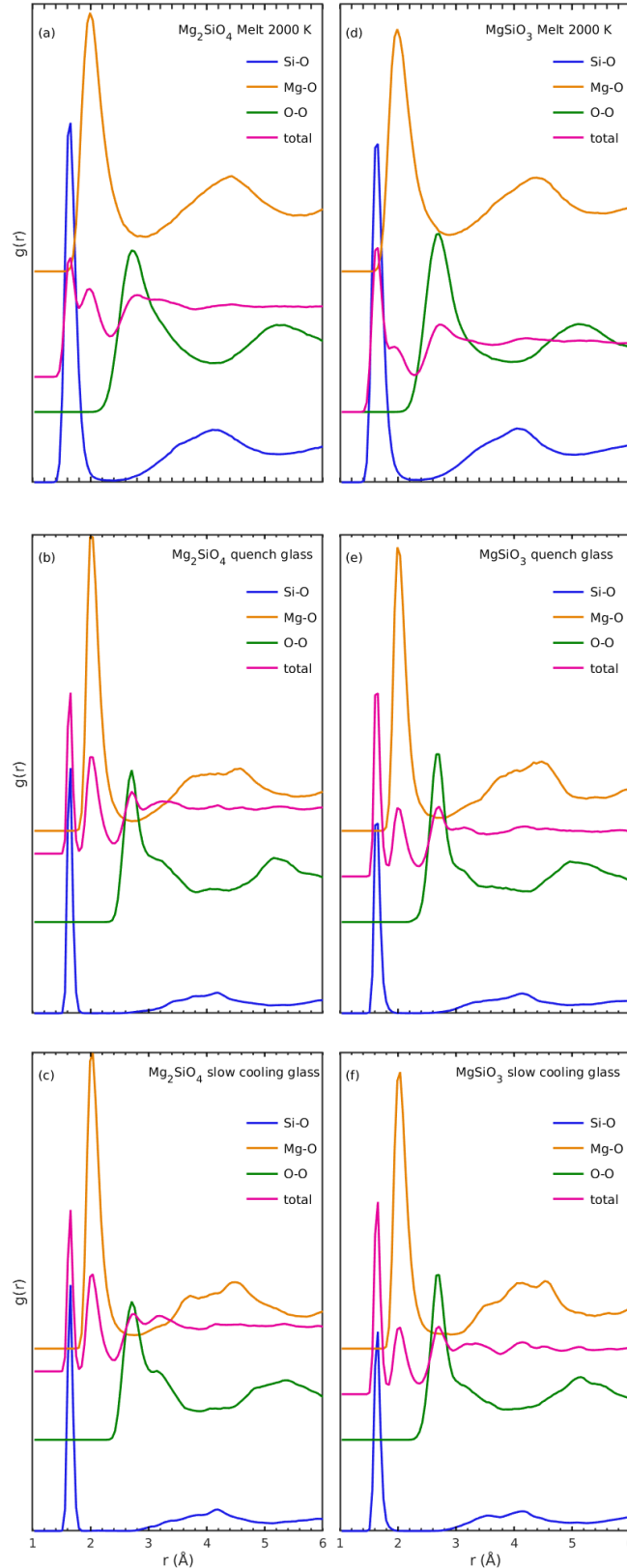


Figure 8.1: Total and partial radial distribution functions for Mg_2SiO_4 (left column) and MgSiO_3 (right column) melt at 2000 K (top), quenched (middle) and slowly cooled glass at 300 K (bottom). Total radial distribution function (magenta) and the contributions due to Si-O (blue), Mg-O (orange) and O-O (green) are shown. Peak heights are not to scale to emphasize characteristic features of the different partial distribution functions.

without the peaks shifting their positions. The width of the peaks decreases considerably, most prominently for $g_{\text{SiO}}(r)$. Peak locations and relative amplitudes of the dominant RDFs (Si-O and Mg-O) do not differ between the quenched and slowly cooled glasses. Coordination for O with silicon (CN_{OSi}) does not change relative to Mg_2SiO_4 and MgSiO_3 liquids, and same is true in $CN_{\text{SiO}}=4.1$ for MgSiO_3 , while $CN_{\text{SiO}} = 4.0$ for the Mg_2SiO_4 glasses. Mg-O coordination is more strongly affected: when the liquid is quenched, CN_{MgO} reduces to a value of 5.0 for both compositions; in the slowly cooled glass, relaxation effects lead to values of $CN_{\text{MgO}} = 5.2$ for MgSiO_3 and $CN_{\text{MgO}} = 5.1$ for Mg_2SiO_4 , with the relaxation also reflected in a shift of the first minimum in $g_{\text{MgO}}(r)$ to larger r .

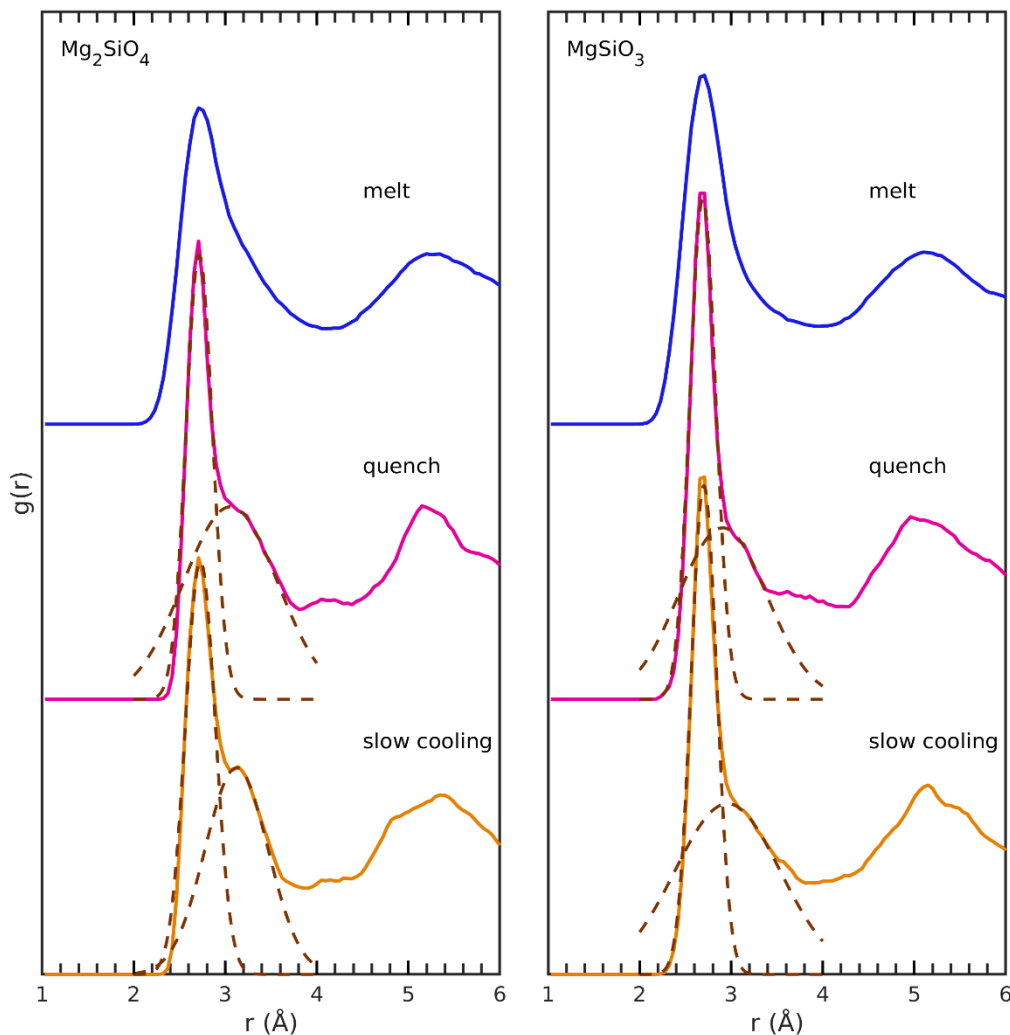


Figure 8.2: O-O radial distribution function for Mg_2SiO_4 (left) and MgSiO_3 (right) melt (2000 K, blue) and glass (300 K) for a density of 2.8 g/cm^3 . The glass is quenched from the melt directly (magenta) or cooled with a rate of 0.1 K/fs (orange). The principal peaks (and shoulders/satellites) in the O-O radial distribution function for the glasses are fit by two Gaussians.

For $g_{OO}(r)$, the first principal peak sharpens in the r -range 2.4-2.9 Å, but a shoulder emerges for both Mg_2SiO_4 and MgSiO_3 quenched glass at ~ 3.1 Å (Figures 8.1b, 8.1e and 8.2). When cooling with a rate of 0.1 K/fs, for Mg_2SiO_4 the shoulder turns to a satellite peak with a maximum at $r=3.14$ Å (Figures 8.1c and 8.2) that is also visible in $g_{\text{tot}}(r)$. By contrast, $g_{OO}(r)$ for the enstatite glass does not change relative to the quench (Figures 8.1f and 8.2). The amplitude for the principal peak in $g_{OO}(r)$ is slightly lower for the slowly cooled glass, both for Mg_2SiO_4 and MgSiO_3 (Figures 8.2).

In order to analyze the influence of the satellite peak in $g_{OO}(r)$ on the experimentally measurable X-ray and neutron structure, we fit Gaussians to the principal and satellite peaks (or shoulders) for Mg_2SiO_4 and MgSiO_3 glasses (Figure 8.2); fits to the principal peaks are very sharp (Gaussian RMS width of 0.20-0.24 Å) and reproduce them well. Gaussian fits constrain the satellite peak for the slowly cooled Mg_2SiO_4 glass well, while for the shoulders for the MgSiO_3 glasses and the Mg_2SiO_4 quench glass they are quite delocalized.

8.2 Structure factors

Total structure factors are calculated from the sum of S_{partial} with its X-ray and neutron scattering factors (equation 3.8). The total X-ray structure factors for the liquid as well as the quenched and slowly cooled glass are dominated by broad peaks in the range $q=1.8$ -2.6 Å⁻¹ (first sharp diffraction peak, FSDP) and 3.8-5.0 Å⁻¹ (Figure 8.3) which is in general agreement with experimental measurements of Benmore et al. (2011) and Kohara et al. (2011) (Figure 8.4). The FSDP for Mg_2SiO_4 (2.2-2.3 Å⁻¹) occurs at slightly larger q than for MgSiO_3 (2.1-2.2 Å⁻¹), again consistent with experiments by Benmore et al. (2011) and Kohara et al. (2011), but at larger (smaller) q than measured by Wilding et al. (2004) for Mg_2SiO_4 (MgSiO_3) (Figure 8.4). As X-rays scatter almost equally on all ions (isoelectronic Mg^{2+} , Si^{4+} and O^{2-}), the partial structure factors all contribute to the total X-ray structure factors. For both Mg_2SiO_4 and MgSiO_3 , S_{MgMg} , S_{MgSi} and S_{MgO} dominate the FSDP (Figure 8.3). The negative contribution from S_{MgO} is more pronounced for the forsterite composition due to the larger number of Mg-O pairs, leading to a smaller amplitude in the FSDP for Mg_2SiO_4 . (*cf.* relative amplitudes for S_{MgO} and S_{SiO} in Figure 8.3). A slight shift in q of the minimum for S_{MgO} between Mg_2SiO_4 and MgSiO_3 liquids is the primary cause for the difference in the FSPD location.

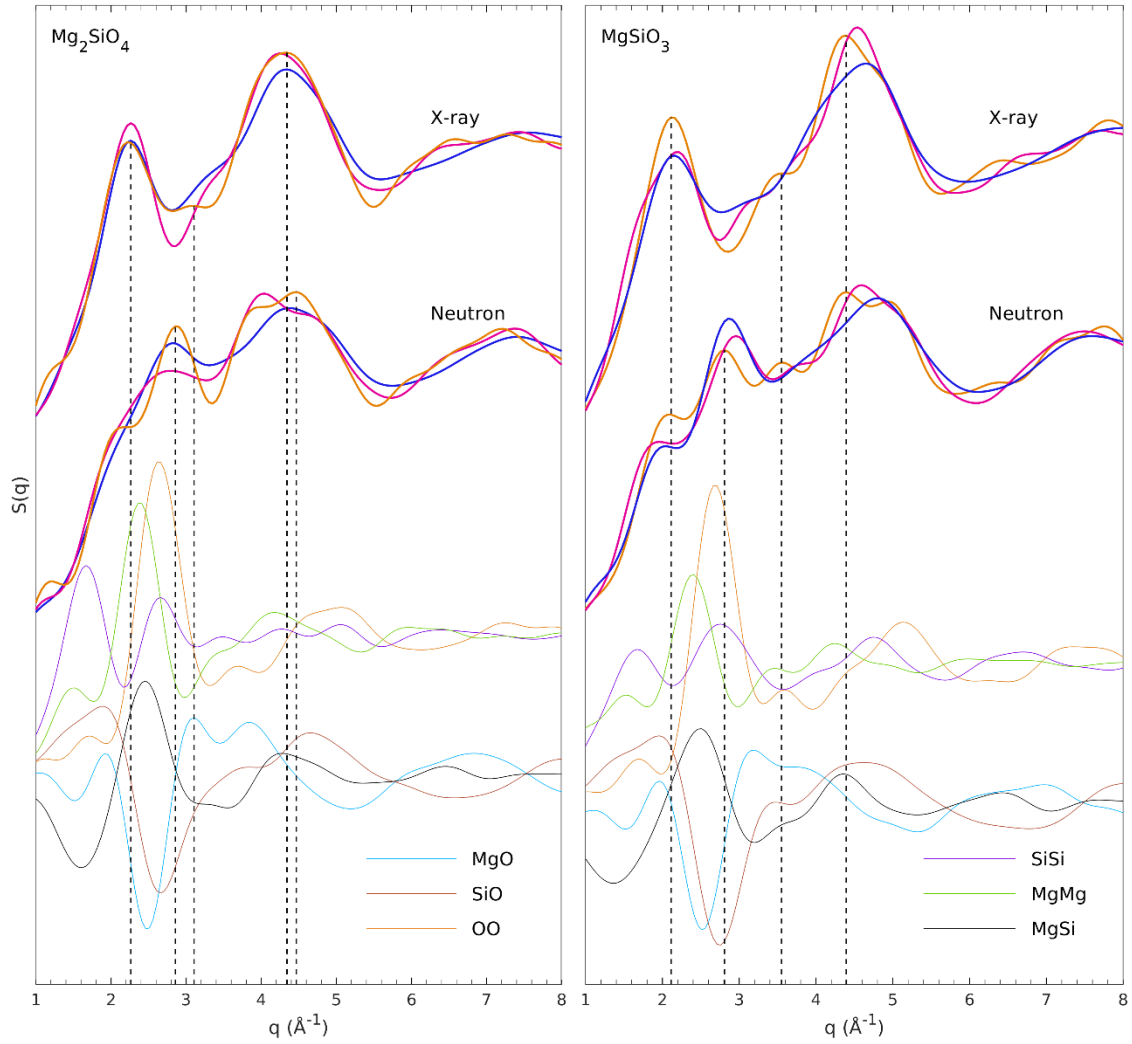


Figure 8.3: X-ray and Neutron total (thick lines) and partial structure factors for liquid (blue), quenched (magenta) and slowly cooled glass (orange), Mg_2SiO_4 (left), MgSiO_3 (right). Partial structure factors (thin lines) are for the slowly cooled glass: S_{MgO} in cyan, S_{SiO} in brownish red, S_{OO} in orange, S_{SiSi} in purple, S_{MgMg} in green and S_{MgSi} in black.

The location of the second broad peak in the X-ray structure factors is similarly determined from broad maxima in S_{MgSi} and S_{MgMg} with some contribution from S_{SiO} , with maxima shifted to larger q -values by $0.2\text{-}0.6 \text{ \AA}^{-1}$ (Figure 8.3); once weighted with the X-ray scattering factor, S_{SiSi} and S_{OO} do not contribute. S_{MgSi} for Mg_2SiO_4 peaks at lower q compared to MgSiO_3 give rise to the shift for the second peak.

The total X-ray structure factor of the glasses (both quench and slowly cooled) show peaks or shoulders between the FSDP and the second peak (q -range $3.0\text{-}3.6 \text{ \AA}^{-1}$), absent in the liquid, that are correlated with maxima in cation-oxygen partial structure factors. For the slowly cooled glass, S_{OO} influences the location of this peak for Mg_2SiO_4 and the shoulder for

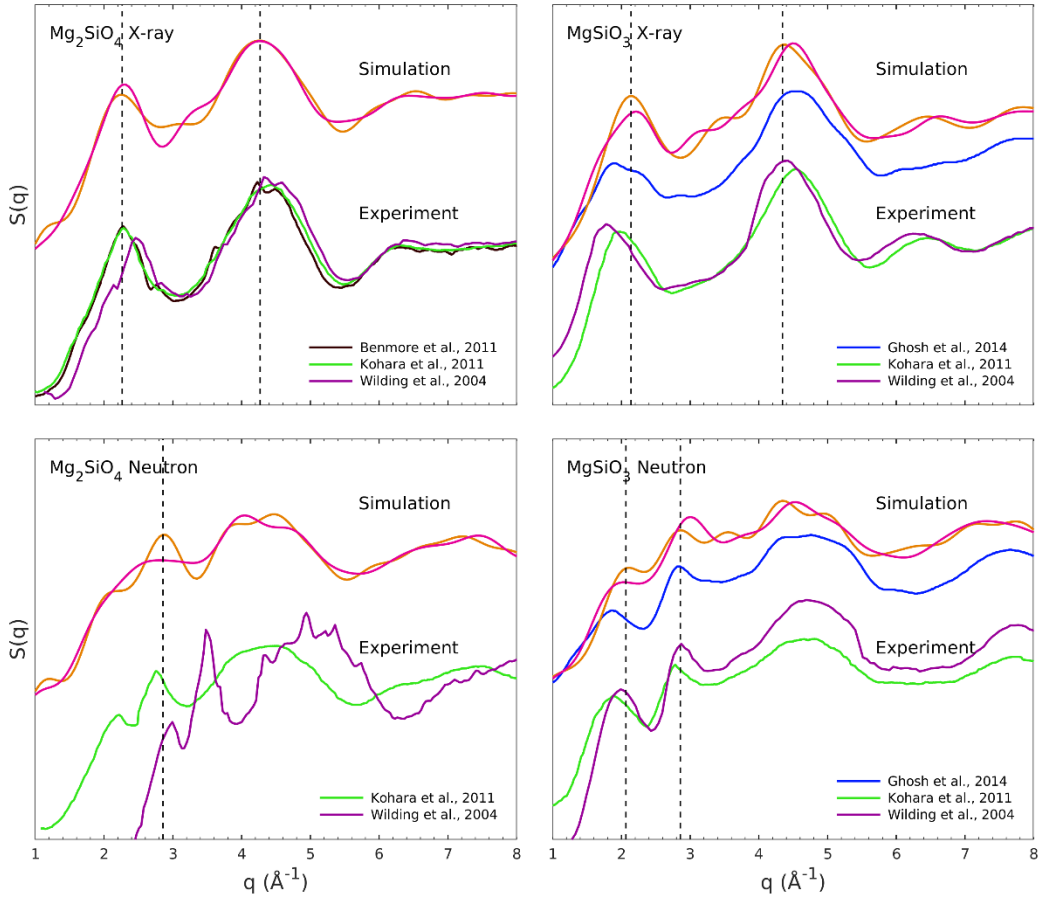


Figure 8.4: Comparison of total X-ray and Neutron structure factors for Mg_2SiO_4 and MgSiO_3 glass. Our results for the quenched glasses are shown in magenta, the slowly cooled glasses in orange. Experimental data are from Benmore et al. (2011) (black), Kohara et al. (2011) (green) and Wilding et al. (2004) (purple) are from experiments. Prior ab-initio simulations by Ghosh et al. (2014) are shown in blue.

MgSiO_3 .

Similar to the X-ray structure factor, the total neutron structure factors for the two silicate liquids are dominated by two peaks (Figure 8.3), with the FSDP occurring at $q=2.4\text{-}3.2 \text{ \AA}^{-1}$ for Mg_2SiO_4 and $q=1.6\text{-}2.4 \text{ \AA}^{-1}$ for MgSiO_3 , and the second peak at $q=4.0\text{-}5.0 \text{ \AA}^{-1}$ and $q=4.4\text{-}5.4 \text{ \AA}^{-1}$ for Mg_2SiO_4 and MgSiO_3 , respectively. These features are semi-quantitatively consistent with measurements of structure factors on both glasses by Kohara et al. (2011), while in the neutron measurements by Wilding et al. (2004) the peaks are shifted to larger q by a varying degree for Mg_2SiO_4 and MgSiO_3 (Figure 8.4). An additional peak measured for the silicate glasses at low q -range by Kohara et al. (2011) – $2.0\text{-}2.4 \text{ \AA}^{-1}$ for Mg_2SiO_4 and $1.6\text{-}2.4 \text{ \AA}^{-1}$ – is not present in DFT-MD simulations for the liquid, but appear for the glasses (peak position at $q=2.1\text{-}2.2 \text{ \AA}^{-1}$), more prominently for MgSiO_3 , consistent with the higher

relative amplitude of this peak measured by Kohara et al. (2011). The slow cooling rate further enhances this peak (Figure 8.3), suggesting that cooling rates do indeed influence the longer-range structure in the glass. Features of total neutron structure factors computed by Ghosh et al. (2014) for MgSiO₃, in particular relative peak amplitudes, are more consistent with our results for the quenched than the slowly cooled glass.

In addition to the emergence of the low- q peak, the second diffraction peak splits for the MgSiO₃ glass with the slow cooling rate: An additional peak at $q=3.3-3.7 \text{ \AA}^{-1}$ is present that also emerges as a shoulder in the results by Ghosh et al. (2014), but is not visible in the neutron diffraction experiments (Figure 8.4).

8.3 Oxygen-oxygen contributions to S_q

As oxygen is the strongest neutron scatterer in the Mg-silicates considered here, diffraction peaks are dominated by contributions from cation-oxygen partial structure factors and S_{OO} . The prominent peak for S_{OO} at $q=2.6-2.7 \text{ \AA}^{-1}$ (Figure 8.3) is partly offset by negative contributions from S_{SiO} and S_{MgO} , and shifted to larger q in the process. The position of the maxima for the second broad peak in the liquid is determined by S_{SiO} ($q=4.6-4.8 \text{ \AA}^{-1}$), and the broadening is caused by S_{MgO} (maximum at lower q) and S_{OO} (maximum at larger q). As the peaks in the partial structure factors sharpen and split for the glass, they give rise to more complex S_{total} as described above, with the low- q peaks ($2.1-2.2 \text{ \AA}^{-1}$) stemming from maxima for S_{SiO} and S_{MgO} ; the cation contributions (S_{MgMg} and S_{SiSi}) shift the maximum to slightly larger q (Figure 8.3). Features in S_{total} in the range $q=3.3-3.7 \text{ \AA}^{-1}$ arise from peaks in S_{OO} and S_{SiO} .

To test to what extent the differences in structure factor features between the liquid and the slowly cooled glass for Mg₂SiO₄ arise from the satellite peak in g_{OO} (Figure 8.2), we perform a Fourier transformation for comparison with S_{OO} (Figure 8.5): The Gaussian fit to the principal peak describes the general feature of the two maxima; however, the peak location of S_{OO} is not well reproduced in any of the glass systems considered. The first peak is located at a q -value that is too large by $0.2-0.3 \text{ \AA}^{-1}$, the second at a q -value too large by a similar amount for Mg₂SiO₄, although this second peak in S_{OO} for the slowly cooled glass is rather broad; for MgSiO₃, the second peak is well described by the Gaussian fit to the principal peak in g_{OO} . The Gaussian fitted to the satellite peak results in a first structure factor maximum at

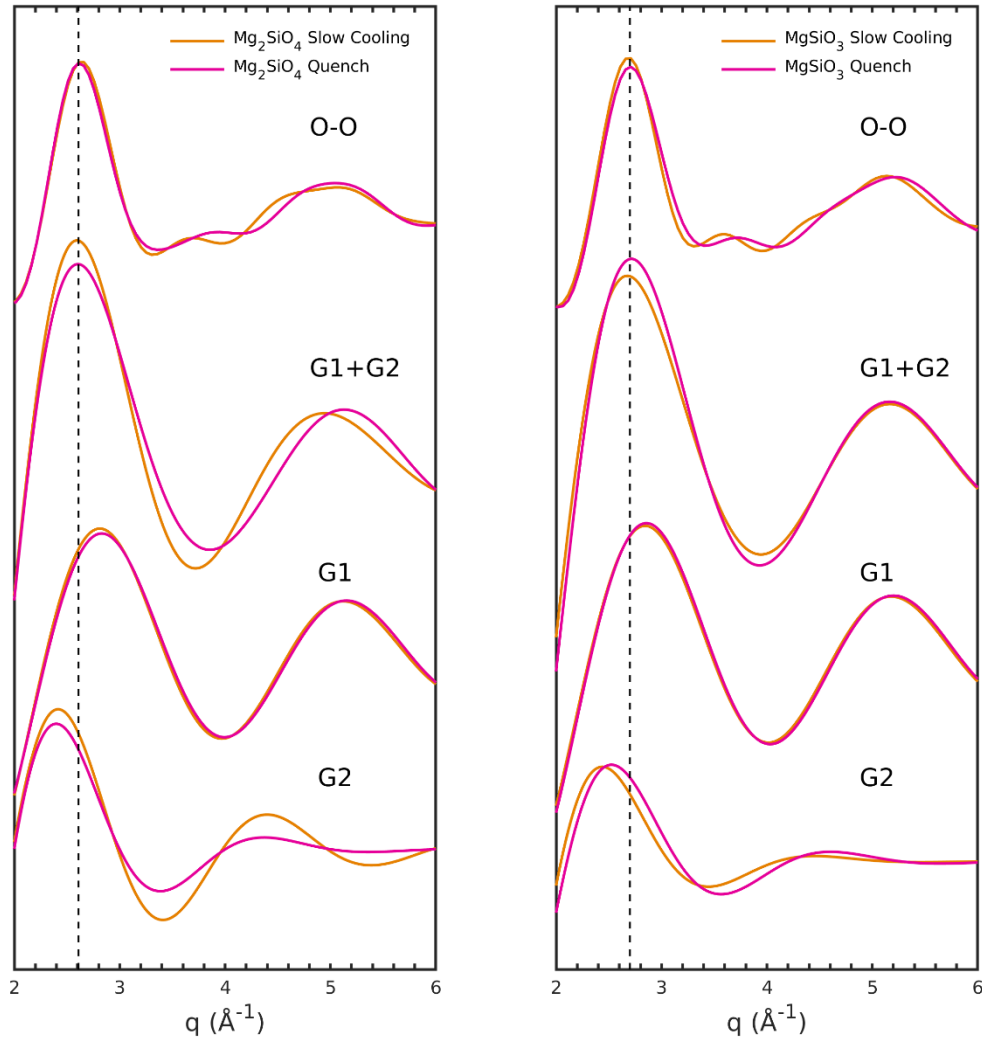


Figure 8.5: *O-O* partial structure factor and the components and sum of the Fourier transform for the two Gaussian fitted to the radial distribution function (Figure 8.2), representing their respective contribution to the *O-O* partial structure factor for Mg_2SiO_4 (left), MgSiO_3 (right) We show the results for slowly cooled (orange) and quenched glass (magenta).

lower q . The sum of both Gaussians describes the FSDP location for S_{OO} very well, only for quenched MgSiO_3 glass a small mismatch (0.05 \AA^{-1}) remains. At larger q , the second Gaussian shows a significant amplitude only for slowly cooled Mg_2SiO_4 glass with a narrow RMS width. For all others, the second amplitudes of their Fourier transforms are already small. Subtle features in the q -range $3.2\text{-}3.6 \text{ \AA}^{-1}$ for S_{OO} and therefore S_{neutron} are not described by such an analysis.

The occurrence of the satellite peak in g_{OO} at $r \sim 3.1$ Å for the slowly cooled Mg_2SiO_4 glass leaves no clear fingerprint in the structure factor, and the simulated neutron structure factors for the quenched and slowly cooled glasses describe the experimental data by Kohara et al. (2011) similarly well (Figure 8.4).

8.4 Glass under compression

When the slowly cooled glass is compressed, the satellite peak in $g_{OO}(r)$ for Mg_2SiO_4 disappears, with a small shoulder persisting to $\rho = 3.0$ g/cm³ which is absent at $\rho = 3.2$ g/cm³. For the higher densities, the hot compression, followed by slow cooling leads to radial distribution functions that are identical to the cold compressed results within the margins of errors of such an analysis. This suggests that the small degree of O-O ordering that we observe at low density is a transient feature that disappears in compression experiments, both for cold compression and in shock wave experiments along the Hugoniot (Akins et al., 2004) and off the Hugoniot paths accessible in new experimental approaches (McGonegle et al., 2020).

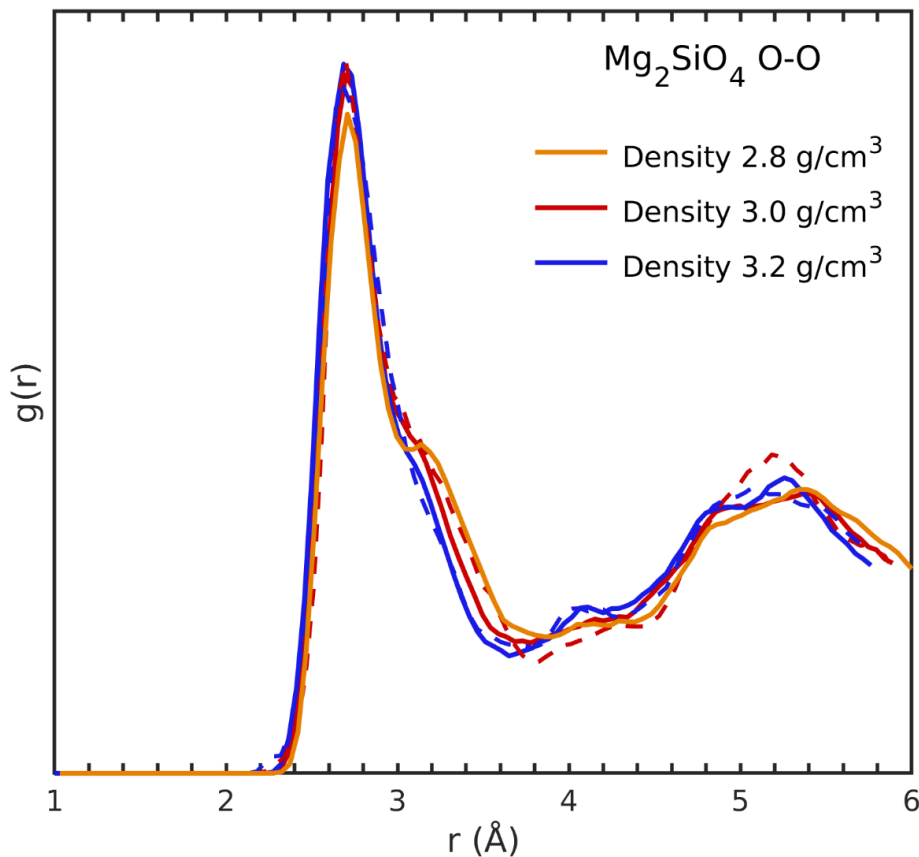


Figure 8.6: O-O radial distribution functions for compressed Mg_2SiO_4 glass starting from the slowly cooled glass with $\rho = 2.8$ g/cm³ (orange) at $\rho = 3.0$ g/cm³ (red) and $\rho = 3.2$ g/cm³ (blue).

8.5 Summary

In our simulations we compare the total and partial radial distribution functions in MgSiO_3 and Mg_2SiO_4 liquids at 2000 K with those of quenched and “slowly cooled” (with a rate of 0.1 K/fs) glass at 300 K to explore whether the liquid is appropriately represented by the glass. As expected, the radial distribution functions of the glass show sharper peaks, and in the glass we observe additional features in $g_{\text{OO}}(r)$, with some dependence of their occurrence on the cooling rate. In particular, for the slowly cooled Mg_2SiO_4 glass, a satellite peak appears at $r \sim 3.1$ Å which is clearly visible in the total radial distribution function, suggesting that the cooling rate indeed influences the glass structure.

As experiments do not have access to the radial distribution function directly, but to the structure factor $S(q)$ in reciprocal space, we explore to what extent features in the former influence the latter. With oxygen the strongest neutron scatterer, features resulting from $g_{\text{OO}}(r)$ should be more apparent in neutron diffraction data. While there is a generally better agreement between measured neutron $S(q)$ and the slowly cooled glass, there is no clear fingerprint in $S_{\text{OO}}(q)$ from the satellite peak.

For higher density, we do not see any difference in the structure of the glass regardless of whether it is compressed from ambient conditions or cooled from compressed liquid. While we indeed establish a difference in resulting glass structure depending on cooling rate, the question of whether this is crystallographically relevant remains open.

9. Conclusion

Understanding melt properties at high pressure is of critical importance for magma ocean processes in the early Earth. Especially the compositional and density difference between melt and coexisting solids (forming, e.g., at the liquidus) determines its compositional evolution, crystallization and dynamics (Labrosse et al., 2007; Ballmer et al., 2017). Here we contribute to an improved understanding of properties associated to melting relations for mantle compositions and physical properties of the solid and liquids along different lines and with different approaches. We have performed multi-anvil experiments, integrated the experimental results in thermodynamic models and performed ab initio simulations. We draw conclusions from each of these approaches, and briefly discuss limitations and possible next steps in that context.

9.1 Multi-anvil experiments

We have performed melting experiments in the $\text{MgSiO}_3\text{-SiO}_2$ system, and quenched melt is recovered from a $\text{Mg}_{0.4}\text{Si}_{0.6}\text{O}_{1.6}$ starting composition exposed to 24 GPa and $\sim 2750 \pm 100$ K. This sample shows stishovite crystals to coexist with the melt, and electron probe analysis determines the liquid composition as $X_{\text{SiO}_2} = 0.53 \pm 0.03$. This composition tightly constrains the eutectic point, close to the MgSiO_3 bridgmanite composition. Combined with previous experiments in the MgO-MgSiO_3 system (Liebske and Frost, 2012), our work completes the melting phase relations description along the MgO-SiO_2 join at pressures of the uppermost lower mantle.

We have performed melting experiments of $(\text{Mg}_{0.9}\text{Fe}_{0.1})\text{SiO}_3$, $(\text{Mg}_{0.8}\text{Fe}_{0.2})\text{SiO}_3$, $(\text{Mg}_{0.7}\text{Fe}_{0.3})\text{SiO}_3$ and $(\text{Mg}_{0.5}\text{Fe}_{0.5})\text{SiO}_3$ along the $\text{MgSiO}_3\text{-FeSiO}_3$ join, at 24 GPa, and partial melt was observed at temperatures of 2650 ± 100 K, 2615 ± 100 K, 2580 ± 100 K and 2510 ± 100 K, respectively. In the recovered samples, bridgmanite is found to coexist with melt. With increasing FeSiO_3 content of the starting composition, the FeO equilibrium constant $K_D^{\text{brg-liquid}}$ decreases with values of 0.31 ± 0.07 , 0.29 ± 0.04 , 0.26 ± 0.02 and 0.22 ± 0.02 , and the iron component in bridgmanite increases from $X(\text{FeO}/(\text{FeO}+\text{MgO})) = 0.03$, 0.07, 0.12 to 0.17. The occurrence of a solid phase assemblage of bridgmanite, magnesiowüstite plus stishovite for the $(\text{Mg}_{0.5}\text{Fe}_{0.5})\text{SiO}_3$ starting composition suggests that we have reached the solubility limit of FeSiO_3 in the bridgmanite solid solution.

In order to better understand the pressure dependence of melt relations and therefore crystallization in a deeper magma ocean, experiments at higher pressure and temperature for the MgO-SiO₂ and the FeSiO₃-MgSiO₃ systems would be very helpful, also to better constrain the thermodynamic models for melts coexisting with bridgmanite. With sintered diamond cubes and boron-doped diamond (BDD) heater, relevant conditions with pressures of 30 GPa and temperatures of 4000 K can be achieved in the multi-anvil press (Yamazaki et al., 2014; Xie et al., 2017).

After establishing melting relations in the three-component system FeO-MgO-SiO₂ in our work, adding Al₂O₃ to the experiments with pyrolite and basalt abundances provide a logical next stepping stone towards complex compositions of geological relevance. With its strong influence on the stability range of garnets (Gasparik 2014; Belmonte et al., 2017) and the coupled Fe³⁺+Al³⁺ ↔ Mg²⁺+Si⁴⁺ substitution in bridgmanite (Lin et al., 2016; Kumosov et al., 2017), Al₂O₃ is likely to have a strong influence on melt relations, significantly more so than CaO that forms its own mineral phase in the lower mantle, CaSiO₃ perovskite (Kurashina et al., 2004; Komabayashi et al., 2007).

9.2 Thermodynamic modelling

We have developed thermodynamic descriptions for the melting phase relations in the MgO-SiO₂ and the FeO-MgO-SiO₂ systems at pressures for Earth's lower mantle, and use the BurnMan toolkit (Cottaar et al., 2014) for implementation and evaluation. The thermodynamic description is based on the liquid oxide components (FeO, MgO, and SiO₂) and a number of solid phases: MgO periclase, MgSiO₃ bridgmanite and SiO₂ stishovite, plus FeO wüstite and FeSiO₃ bridgmanite for the FeO-MgO-SiO₂ system. Thermodynamic parameters for the solids are from the database of Stixrude and Lithgow-Bertelloni (2011), reformulated in the model of de Koker and Stixrude (2009) to make them compatible to the liquid description. Liquid parameters for MgO are from de Koker et al. (2013), for FeO parameters are fitted from the melting curve, including the most recent data at pressures of the lowermost mantle (Fu et al., 2018). Parameters for liquid SiO₂ and mixing properties (interaction parameters $W_{\text{MgO-SiO}_2}$ and $W_{\text{FeO-SiO}_2}$) are derived from our multi anvil data.

For the MgO-SiO₂ system, our model predicts the MgO-MgSiO₃ eutectic to evolve towards the MgO-rich side with increasing pressure, and reach values close to Mg₂SiO₄ ($X_{\text{SiO}_2} = 0.35 \pm 0.02$) at conditions of the core-mantle boundary. The MgSiO₃-SiO₂ eutectic becomes more silica rich with pressure and reaches $X_{\text{SiO}_2} = 0.66 \pm 0.01$ for the lowermost mantle. These predicted eutectic compositions confirm data by Ozawa et al. (2018) from diamond anvil cell experiments. The eutectic temperatures are very similar in both systems, with $\sim 5400 \pm 200$ K at core-mantle boundary pressure. Based on our model, the experimentally described lower solidus temperature for basalt relative to peridotite (Andrault et al., 2011; Andrault et al., 2014) at core-mantle boundary conditions cannot be explained within the MgO-SiO₂ binary; rather, it must be affected by other chemical components such as FeO, Al₂O₃ or CaO.

Our thermodynamic model in the FeO-MgO-SiO₂ system well reproduced experimental melting relations for the MgO-SiO₂, MgSiO₃-FeSiO₃ and FeO-SiO₂ binaries at 24 GPa. However, for the MgO-FeO system our computed solidus and liquidus curves differ significantly from the data by Du and Lee (2014) and Deng and Lee (2017) at 27 GPa. As Deng et al. (2019) point out, differences between model descriptions of MgO-FeO melting can be traced to the enthalpy change at melting (ΔH^m) for the endmembers, which we find very similar while previous studies describe $\Delta H_{\text{FeO}}^m > \Delta H_{\text{MgO}}^m$. This aspect of the model warrants further exploration.

Along the FeO-SiO₂ join, our model predicts a eutectic composition that is very close to FeO, consistent with diamond anvil cell experiments by Kato et al. (2016). Its temperature at 136 GPa (~ 3500 K), and therefore that of the solidus in the system is lower than the estimated mantle geotherm (Anzellini et al., 2013) near the core-mantle boundary which supports the idea that subducted banded-iron formations could cause partial melting in the lowermost mantle (Dobson and Brodholt, 2005; Kato et al., 2016) and contribute to the origin of seismic low-velocity zones there (Hernlund and Jellinek, 2010; McNamara et al., 2010). More robust constraints on the thermodynamic description of the FeO-MgO-SiO₂ system, especially by experiments at high pressure, would be helpful to confirm such properties.

9.3 Ab initio simulations

In our molecular dynamics simulations on FeO-bearing olivine (Mg₂₈Fe₄Si₁₆O₆₄) and forsterite liquids at 3000 K we show that the partial molar volume of MgO and FeO are

virtually indistinguishable; density differences only stem from the higher molar weight of FeO. Magnetic moments on the Fe atoms in $\text{Mg}_{28}\text{Fe}_4\text{Si}_{16}\text{O}_{64}$ are $4.0 \pm 0.1 \mu_{\text{B}}$ up to ~ 35 GPa (high spin), and then decrease with pressure, showing strong fluctuations, reflected in the large standard deviation at 370 GPa: $0.5 \pm 0.4 \mu_{\text{B}}$. The onset of the spin transition roughly agrees with the observation of strongly changing partitioning of FeO between solid and liquid at lower mantle pressure (Nomura et al., 2011).

In order to better constrain melt buoyancy during magma ocean crystallization for deep earth and exoplanets further simulations would be required that address whether the similarity in molar volume between MgO and FeO is independent on composition (e.g., by looking at $\text{Mg}_{1-x}\text{Fe}_x\text{SiO}_3$) or FeO concentration in the olivine.

In further molecular dynamics simulations, we have examined structural difference between Mg_2SiO_4 and MgSiO_3 melt and glass. Peaks in the radial distribution functions for the melts are broader and smaller in amplitude than for the glass. By varying the cooling rate when quenching the melt to the glass (immediate quench vs. 0.1 K per femtosecond), we find that “slowly” cooled glass shows more structural features, especially at small interatomic distances. However, differences are too small to significantly impact structure factors that are accessible in experiments by X-rays and neutrons, and reflect intermediate interatomic distances.

To address such cooling phenomena more realistically, larger-scale molecular dynamics simulations would be required. Not only large cells with thousands of atoms (rather than 210 used here), but also significantly slower cooling rates are required to approach experimental scenarios. Whether the system needs to be thermally equilibrated at various temperatures (Ghosh et al., 2014) or one electronic optimization cycle is sufficient to achieve converged results is another question that remains open. Machine learning potentials based on density functional results for a limited set of conditions provide access to this type of simulations, at an ab initio level of accuracy (Behler and Csányi, 2021; Deng and Stixrude, 2021).

References

- Abers, G. A., van Keken, P. E., Kneller, E. A., Ferris, A. and Stachnik, J. C. (2006). The thermal structure of subduction zones constrained by seismic imaging: Implications for slab dehydration and wedge flow. *Earth and Planetary Science Letters*, 241, 387-397.
- Akaogi, M., Ito, E. and Navrotsky, A. (1989). Olivine-modified spinel-spinel transitions in the system Mg_2SiO_4 - Fe_2SiO_4 : Calorimetric measurements, thermochemical calculation, and geophysical application. *Journal of Geophysical Research: Solid Earth*, 94, 15671-15685.
- Akins, J. A., Luo, S. N., Asimow, P. D. and Ahrens, T. J. (2004). Shock-induced melting of $MgSiO_3$ perovskite and implications for melts in Earth's lowermost mantle. *Geophysical Research Letters*, 31, L14612.
- Allen, M. P. and Tildesley, D. J. (1987). *Computer simulation of liquids*. Oxford University Press.
- Andrault, D., Bolfan-Casanova, N., Nigro, G. L., Bouhifd, M. A., Garbarino, G. and Mezouar, M. (2011). Solidus and liquidus profiles of chondritic mantle: Implication for melting of the Earth across its history. *Earth and Planetary Science Letters*, 304, 251-259.
- Andrault, D., Petitgirard, S., Nigro, G. L., Devidal, J. L., Veronesi, G., Garbarino, G. and Mezouar, M. (2012). Solid-liquid iron partitioning in Earth's deep mantle. *Nature*, 487, 354-357.
- Andrault, D., Pesce, G., Bouhifd, M. A., Bolfan-Casanova, N., Hénot, J. M., and Mezouar, M. (2014). Melting of subducted basalt at the core-mantle boundary. *Science*, 344, 892-895.
- Andrault, D., Bolfan-Casanova, N., Bouhifd, M. A., Boujibar, A., Garbarino, G., Manthilake, G., Mezouar, M., Monteux, J., Parisiades, P. and Pesce, G. (2017). Toward a coherent model for the melting behavior of the deep Earth's mantle. *Physics of the Earth and Planetary Interiors*, 265, 67-81.

Andraut, D., Morard, G., Garbarino, G., Mezouar, M., Bouhifd, M. A., and Kawamoto, T. (2020). Melting behavior of SiO₂ up to 120 GPa. *Physics and Chemistry of Minerals*, 47, 10.

Anzellini, S., Dewaele, A., Mezouar, M., Loubeyre, P. and Morard, G. (2013). Melting of iron at Earth's inner core boundary based on fast X-ray diffraction. *Science*, 340, 464-466.

Angel, R. J., Alvaro, M. and Gonzalez-Platas, J. (2014). EosFit7c and a Fortran module (library) for equation of state calculations. *Zeitschrift für Kristallographie-Crystalline Materials*, 229, 405-419.

Asphaug, E. (2014). Impact origin of the Moon? *Annual Review of Earth and Planetary Sciences*, 42, 551-578.

Badro, J. (2014). Spin transitions in mantle minerals. *Annual Review of Earth and Planetary Sciences*, 42, 231-248.

Ballmer, M. D., Lourenço, D. L., Hirose, K., Caracas, R., and Nomura, R. (2017). Reconciling magma-ocean crystallization models with the present-day structure of the Earth's mantle. *Geochemistry, Geophysics, Geosystems*, 18, 2785-2806.

Baron, M. A., Lord, O. T., Myhill, R., Thomson, A. R., Wang, W., Trønnes, R. G., and Walter, M. J. (2017). Experimental constraints on melting temperatures in the MgO–SiO₂ system at lower mantle pressures. *Earth and Planetary Science Letters*, 472, 186-196.

Behler, J. and Csányi, G. (2021). Machine learning potentials for extended systems: a perspective. *The European Physical Journal B*, 94, 142.

Belmonte, D., Ottonello, G., Zuccolini, M. V., and Attene, M. (2017). The system MgO-Al₂O₃-SiO₂ under pressure: A computational study of melting relations and phase diagrams. *Chemical Geology*, 461, 54-64.

Belonoshko, A. B., and Dubrovinsky, L. S. (1995). Molecular dynamics of stishovite melting. *Geochimica et Cosmochimica Acta*, 59, 1883-1889.

- Benmore, C. J., Soignard, E., Guthrie, M., Amin, S. A., Weber, J. K. R., McKiernan, K., Wilding, M. C. and Yarger, J. L. (2011). High pressure X-ray diffraction measurements on Mg₂SiO₄ glass. *Journal of Non-Crystalline Solids*, 357, 2632-2636.
- Bercovici, D., and Karato, S. I. (2003). Whole-mantle convection and the transition-zone water filter. *Nature*, 425, 39-44.
- Blander, M., and Pelton, A. D. (1987). Thermodynamic analysis of binary liquid silicates and prediction of ternary solution properties by modified quasichemical equations. *Geochimica et Cosmochimica Acta*, 51, 85-95.
- Blöchl, P. E. (1994). Projector augmented-wave method. *Physical review B*, 50, 17953.
- Born, M. and Oppenheimer, R. (1927). Zur Quantentheorie der Molekeln. *Annalen der Physik*, 389, 457-484.
- Bottinga, Y. (1985). On the isothermal compressibility of silicate liquids at high pressure. *Earth and planetary science letters*, 74, 350-360.
- Boukaré, C. E., Ricard, Y., and Fiquet, G. (2015). Thermodynamics of the MgO-FeO-SiO₂ system up to 140 GPa: Application to the crystallization of Earth's magma ocean. *Journal of Geophysical Research: Solid Earth*, 120, 6085-6101.
- Brown, P. J., Fox, A. G., Maslen, E. N., O'Keefe, M. A. and Willis, B. T. M. (2006). Intensity of diffracted intensities. In E. Prince, Ed., *International Tables for Crystallography*, vol. C, Kluwer, Dordrecht, Netherlands, 554–595.
- Caracas, R., Hirose, K., Nomura, R. and Ballmer, M. D. (2019). Melt–crystal density crossover in a deep magma ocean. *Earth and Planetary Science Letters*, 516, 202-211.
- Carter, P. J., Lock, S. J. and Stewart, S. T. (2020). The energy budgets of giant impacts. *Journal of Geophysical Research: Planets*, 125, e2019JE006042.

Cerantola, V., Bykova, E., Kuppenko, I., Merlini, M., Ismailova, L., McCammon, C., Bykov, M., Chumakov, A. I., Petitgirard, S., Kantor, I. and Svitlyk, V. (2017). Stability of iron-bearing carbonates in the deep Earth's interior. *Nature Communications*, 8, 15960.

Chemia, Z., Dolejš, D., and Steinle-Neumann, G. (2015). Thermal effects of variable material properties and metamorphic reactions in a three-component subducting slab. *Journal of Geophysical Research: Solid Earth*, 120, 6823-6845.

Chorażewski, M., Postnikov, E. B., Jasiok, B., Nedyalkov, Y. V. and Jacquemin, J. (2017). A fluctuation equation of state for prediction of high-pressure densities of ionic liquids. *Scientific Reports*, 7, 5563.

Chust, T. C., Steinle-Neumann, G., Dolejš, D., Schuberth, B. S. A., and Bunge, H. P. (2017). MMA-EoS: A computational framework for mineralogical thermodynamics. *Journal of Geophysical Research: Solid Earth*, 122, 9881-9920.

Corgne, A., Liebske, C., Wood, B. J., Rubie, D. C. and Frost, D. J. (2005). Silicate perovskite-melt partitioning of trace elements and geochemical signature of a deep perovskitic reservoir. *Geochimica et Cosmochimica Acta*, 69, 485-496.

Cottaar, S., Heister, T., Rose, I., and Unterborn, C. (2014). BurnMan: A lower mantle mineral physics toolkit. *Geochemistry, Geophysics, Geosystems*, 15, 1164-1179.

Dasgupta, R. (2018). Volatile-bearing partial melts beneath oceans and continents—Where, how much, and of what compositions? *American Journal of Science*, 318, 141-165.

Dauphas, N., Poitrasson, F., Burkhardt, C., Kobayashi, H., and Kurosawa, K. (2015). Planetary and meteoritic Mg/Si and $\delta^{30}\text{Si}$ variations inherited from solar nebula chemistry. *Earth and Planetary Science Letters*, 427, 236-248.

de Koker, N. P., Stixrude, L. and Karki, B. B., (2008). Thermodynamics, structure, dynamics, and freezing of Mg_2SiO_4 liquid at high pressure. *Geochimica et Cosmochimica Acta*, 72, 1427-1441.

de Koker, N., and Stixrude, L. (2009). Self-consistent thermodynamic description of silicate liquids, with application to shock melting of MgO periclase and MgSiO_3 perovskite. *Geophysical Journal International*, 178, 162-179.

de Koker, N., Karki, B. B., and Stixrude, L. (2013). Thermodynamics of the MgO– SiO_2 liquid system in Earth's lowermost mantle from first principles. *Earth and Planetary Science Letters*, 361, 58-63.

Deng, J., Miyazaki, Y. and Lee, K. K. (2019). Implications for the melting phase relations in the MgO–FeO system at core–mantle boundary conditions. *Journal of Geophysical Research: Solid Earth*, 124, 1294-1304.

Deng, J. and Stixrude, L. (2021). Thermal conductivity of silicate liquid determined by machine learning potentials. *Geophysical Research Letters* 48, e2021GL093806.

Deuss, A. and Woodhouse, J. (2001). Seismic observations of splitting of the mid-transition zone discontinuity in Earth's mantle. *Science*, 294, 354-357.

Di Paola, C., and Brodholt, J. P. (2016). Modeling the melting of multicomponent systems: the case of MgSiO_3 perovskite under lower mantle conditions. *Scientific Reports*, 6, 29830.

Dobson, D. P. and Brodholt, J. P. (2005). Subducted banded iron formations as a source of ultralow-velocity zones at the core–mantle boundary. *Nature*, 434, 371-374.

Dorfman, S. M. (2016). Phase diagrams and thermodynamics of lower mantle materials. *Deep Earth: Physics and Chemistry of the Lower Mantle and Core*, In: Terasaki, H., Fischer, R. A., editors. *Deep earth: physics and chemistry of the lower mantle and core*. American Geophysical Union, Washington D. C. 217, 241-252.

Dorfman, S. M., Dutton, S. E., Potapkin, V., Chumakov, A. I., Rueff, J. P., Chow, P., Xiao, Y., Cava, R. J., Duffy, T. S., McCammon, C. A. and Gillet, P. (2016). Electronic transitions of iron in almandine-composition glass to 91 GPa. *American Mineralogist*, 101, 1659-1667.

Dove, M. T., Tucker, M. G. and Keen, D. A. (2002). Neutron total scattering method: simultaneous determination of long-range and short-range order in disordered materials. *European Journal of Mineralogy*, 14, 331-348.

Dubrovinsky, L. S., Dubrovinskaia, N. A., Saxena, S. K., Tutti, F., Rekhi, S., Le Bihan, T., Shen, G. Y., and Hu, J. (2001). Pressure-induced transformations of cristobalite. *Chemical Physics Letters*, 333, 264-270.

Du, Z. and Lee, K. K. (2014). High-pressure melting of MgO from (Mg, Fe)O solid solutions. *Geophysical Research Letters*, 41, 8061-8066.

Dudarev, S. L., Botton, G. A., Savrasov, S. Y., Humphreys, C. J. and Sutton, A. P. (1998). Electron-energy-loss spectra and the structural stability of nickel oxide: An LSDA+ U study. *Physical Review B*, 57, 1505-1509.

Dziewonski, A. M. and Anderson, D. L. (1981). Preliminary reference Earth model. *Physics of the Earth and Planetary Interiors*, 25, 297-356.

Elardo, S. M., Draper, D. S., and Shearer Jr, C. K. (2011). Lunar Magma Ocean crystallization revisited: Bulk composition, early cumulate mineralogy, and the source regions of the highlands Mg-suite. *Geochimica et Cosmochimica Acta*, 75, 3024-3045.

Elkins-Tanton, L. T., Parmentier, E. M., and Hess, P. C. (2003). Magma ocean fractional crystallization and cumulate overturn in terrestrial planets: Implications for Mars. *Meteoritics & Planetary Science*, 38, 1753-1771.

Elkins-Tanton, L. T. (2008). Linked magma ocean solidification and atmospheric growth for Earth and Mars. *Earth and Planetary Science Letters*, 271, 181-191.

- Elkins-Tanton, L. T. (2012). Magma oceans in the inner solar system. *Annual Review of Earth and Planetary Sciences*, 40, 113-139.
- Everhart, T. E. and Thornley, R. F. M. (1960). Wide-band detector for micro-microampere low-energy electron currents. *Journal of scientific instruments*, 37, 246-248.
- Fabrichnaya, O., Saxena, S. K., Richet, P., and Westrum, E. F. (2004). *Thermodynamic data, models, and phase diagrams in multicomponent oxide systems*. Springer, Berlin, 198.
- Fedotenko, T., Dubrovinsky, L., Aprilis, G., Koemets, E., Snigirev, A., Snigireva, I., Barannikov, A., Ershov, P., Cova, F., Hanfland, M. and Dubrovinskaia, N. (2019). Laser heating setup for diamond anvil cells for in situ synchrotron and in house high and ultra-high pressure studies. *Review of Scientific Instruments*, 90, 104501.
- Fei, Y., Seagle, C. T., Townsend, J. P., McCoy, C. A., Boujibar, A., Driscoll, P., Shulenburg, L. and Furnish, M. D. (2021). Melting and density of MgSiO₃ determined by shock compression of bridgmanite to 1254 GPa. *Nature Communications*, 12, 1-9.
- Feynman, R.P. (1939). Forces in molecules. *Physical Review*, 56, 340.
- Fiquet, G., Auzende, A. L., Siebert, J., Corgne, A., Bureau, H., Ozawa, H., and Garbarino, G. (2010). Melting of peridotite to 140 gigapascals. *Science*, 329, 1516-1518.
- Fischer, R. A. and Campbell, A. J. (2010). High-pressure melting of wustite. *American Mineralogist*, 95, 1473-1477.
- Fischer, R. A., Campbell, A. J., Shofner, G. A., Lord, O. T., Dera, P. and Prakapenka, V. B. (2011). Equation of state and phase diagram of FeO. *Earth and Planetary Science Letters*, 304, 496-502.
- Fischer, R. A., Campbell, A. J., Chidester, B. A., Reaman, D. M., Thompson, E. C., Pigott, J. S., Prakapenka, V.B., and Smith, J. S. (2018). Equations of state and phase boundary for stishovite and CaCl₂-type SiO₂. *American Mineralogist*, 103, 792-802.

Fournier, J. M. (1993). Chemical pressure in actinide systems. *Physica B: Condensed Matter*, 190, 50-54.

Fratanduono, D. E., Millot, M., Kraus, R. G., Spaulding, D. K., Collins, G. W., Celliers, P. M., and Eggert, J. H. (2018). Thermodynamic properties of MgSiO₃ at super-Earth mantle conditions. *Physical Review B*, 97, 214105.

Frost, D. J., Poe, B. T., Trønnes, R. G., Liebske, C., Duba, A., and Rubie, D. C. (2004). A new large-volume multianvil system. *Physics of the Earth and Planetary Interiors*, 143, 507-514.

Frost, D. J., Asahara, Y., Rubie, D. C., Miyajima, N., Dubrovinsky, L. S., Holzappel, C., Ohtani, E., Miyahara, M. and Sakai, T. (2010). Partitioning of oxygen between the Earth's mantle and core. *Journal of Geophysical Research: Solid Earth*, 115, B02202.

Fuchizaki, K. (2019). Predicting the Melting Curve of MgO: An Essential Update. *Journal of the Physical Society of Japan*, 88, 065003.

Funamori, N., Jeanloz, R., Miyajima, N. and Fujino, K. (2000). Mineral assemblages of basalt in the lower mantle. *Journal of Geophysical Research: Solid Earth*, 105, 26037-26043.

Fumagalli, P. and Klemme, S. (2015). Phase transitions and mineralogy of the upper mantle. In: Gerald Schubert (editor-in-chief) *Treatise on Geophysics*, vol 2. 2nd edn, Elsevier, Oxford, 7–31.

Fu, S., Yang, J., Zhang, Y., Liu, J., Greenberg, E., Prakapenka, V. B., Okuchi, T. and Lin, J. F. (2018). Melting behavior of the lower-mantle ferropericlaase across the spin crossover: Implication for the ultra-low velocity zones at the lowermost mantle. *Earth and Planetary Science Letters*, 503, 1-9.

Gale, A., Dalton, C. A., Langmuir, C. H., Su, Y. and Schilling, J. G. (2013). The mean composition of ocean ridge basalts. *Geochemistry, Geophysics, Geosystems*, 14, 489-518.

Gasparik, T. (1993). The role of volatiles in the transition zone. *Journal of Geophysical Research: Solid Earth*, 98, 4287-4299.

Gasparik, T. (2014). System MgO–Al₂O₃–SiO₂. In *Phase Diagrams for Geoscientists*. Springer, New York, NY, 33-79.

Gazzillo, D., Giacometti, A., Guido Della Valle, R., Venuti, E. and Carsughi, F. (1999). A scaling approximation for structure factors in the integral equation theory of polydisperse nonionic colloidal fluids. *The Journal of Chemical Physics*, 111, 7636-7645.

Ghiorso, M. S., Carmichael, I. S., Rivers, M. L. and Sack, R. O. (1983). The Gibbs free energy of mixing of natural silicate liquids; an expanded regular solution approximation for the calculation of magmatic intensive variables. *Contributions to Mineralogy and Petrology*, 84, 107-145.

Ghosh, D. B., Karki, B. B., and Stixrude, L. (2014). First-principles molecular dynamics simulations of MgSiO₃ glass: Structure, density, and elasticity at high pressure. *American Mineralogist*, 99, 1304-1314.

Ghosh, D. B. and Karki, B. B. (2016). Solid-liquid density and spin crossovers in (Mg,Fe)O system at deep mantle conditions. *Scientific reports*, 6, 1-7.

Ghosh, D. B. and Karki, B. B. (2020). Effects of valence and spin of Fe in MgSiO₃ melts: Structural insights from first-principles molecular dynamics simulations. *Geochimica et Cosmochimica Acta*, 279, 107-118.

Green, D. H., Hibberson, W. O., and Jaques, A. L. (1979), Petrogenesis of mid-ocean ridge basalts. In *The Earth: Its Origin, Structure and Evolution*, edited by McElhinny, M. W., Elsevier, New York, 265 – 290.

Grocholski, B., Shim, S. H., and Prakapenka, V. B. (2013). Stability, metastability, and elastic properties of a dense silica polymorph, seifertite. *Journal of Geophysical Research: Solid Earth*, 118, 4745-4757.

Hall, H. T. (1958). Some high-pressure, high-temperature apparatus design considerations: Equipment for use at 100 000 atmospheres and 3000 °C. *Review of Scientific Instruments*, 29, 267-275.

Hayward, A. T. J. (1967). Compressibility equations for liquids: a comparative study. *British Journal of Applied Physics*, 18, 965-977.

Henderson, G. S., Calas, G., and Stebbins, J. F. (2006). The structure of silicate glasses and melts. *Elements*, 2, 269-273.

Hernlund, J. W., Thomas, C. and Tackley, P. J. (2005). A doubling of the post-perovskite phase boundary and structure of the Earth's lowermost mantle. *Nature*, 434, 882-886.

Hernlund, J. W., and Jellinek, A. M. (2010). Dynamics and structure of a stirred partially molten ultralow-velocity zone. *Earth and Planetary Science Letters*, 296, 1-8.

Hirose, K., Fei, Y., Ma, Y., and Mao, H. K. (1999). The fate of subducted basaltic crust in the Earth's lower mantle. *Nature*, 397, 53-56.

Hirose, K. and Fei, Y. (2002). Subsolvus and melting phase relations of basaltic composition in the uppermost lower mantle. *Geochimica et Cosmochimica Acta*, 66, 2099-2108.

Hirose, K. (2006). Postperovskite phase transition and its geophysical implications. *Reviews of Geophysics*, 44, RG3001.

Hohenberg, P. and Kohn, W. (1964). Inhomogeneous electron gas. *Physical Review*, 136, B864.

Holland, T. J. B., Hudson, N. F. C., Powell, R., and Harte, B. (2013). New thermodynamic models and calculated phase equilibria in NCFMAS for basic and ultrabasic compositions through the transition zone into the uppermost lower mantle. *Journal of Petrology*, 54, 1901–1920.

Huang, R. (2020). Bridgmanite crystal chemistry and iron content in the Earth's lower mantle (Doctoral dissertation).

Hummer, D. R. and Fei, Y. (2012). Synthesis and crystal chemistry of Fe³⁺-bearing (Mg, Fe³⁺)(Si, Fe³⁺)O₃ perovskite. *American Mineralogist*, 97, 1915-1921.

Irifune, T., Shinmei, T., McCammon, C. A., Miyajima, N., Rubie, D. C. and Frost, D. J. (2010). Iron partitioning and density changes of pyrolite in Earth's lower mantle. *Science*, 327, 193-195.

Ishii, T., Kojitani, H. and Akaogi, M. (2011). Post-spinel transitions in pyrolite and Mg₂SiO₄ and akimotoite–perovskite transition in MgSiO₃: precise comparison by high-pressure high-temperature experiments with multi-sample cell technique. *Earth and Planetary Science Letters*, 309, 185-197.

Ito, E., and Katsura, T. (1992). Melting of ferromagnesian silicates under the lower mantle conditions. In: Syono, Y., Manghnani, M.H. (Eds.), *High-Pressure Research: Applications to Earth and Planetary Sciences*. Terrapub., Tokyo, American Geophysical Union, Washington, DC, 315-322.

Ito, E. and Takahashi, E. (1989). Postspinel transformations in the system Mg₂SiO₄-Fe₂SiO₄ and some geophysical implications. *Journal of Geophysical Research: Solid Earth*, 94, 10637-10646.

Ito, E., Kubo, A., Katsura, T., and Walter, M. J. (2004). Melting experiments of mantle materials under lower mantle conditions with implications for magma ocean differentiation. *Physics of the Earth and Planetary Interiors*, 143, 397-406.

Jiang, X. and Guo, G. Y. (2004). Electronic structure, magnetism, and optical properties of Fe₂SiO₄ fayalite at ambient and high pressures: A GGA+ U study. *Physical Review B*, 69, 155108.

- Johnson, E. R., Wallace, P. J., Cashman, K. V., Granados, H. D., and Kent, A. J. (2008). Magmatic volatile contents and degassing-induced crystallization at Volcán Jorullo, Mexico: Implications for melt evolution and the plumbing systems of monogenetic volcanoes. *Earth and Planetary Science Letters*, 269, 478-487.
- Karki, B. B. (2010). First-principles molecular dynamics simulations of silicate melts: structural and dynamical properties. *Reviews in Mineralogy and Geochemistry*, 71, 355-389.
- Karki, B. B., Ghosh, D. B., Maharjan, C., Karato, S. I. and Park, J. (2018). Density-pressure profiles of Fe-bearing MgSiO₃ liquid: Effects of valence and spin states, and implications for the chemical evolution of the lower mantle. *Geophysical Research Letters*, 45, 3959-3966.
- Kato, C., Hirose, K., Nomura, R., Ballmer, M. D., Miyake, A. and Ohishi, Y. (2016). Melting in the FeO-SiO₂ system to deep lower-mantle pressures: Implications for subducted Banded Iron Formations. *Earth and Planetary Science Letters*, 440, 56-61.
- Katsura, T., Yoneda, A., Yamazaki, D., Yoshino, T. and Ito, E. (2010). Adiabatic temperature profile in the mantle. *Physics of the Earth and Planetary Interiors*, 183, 212-218.
- Kawai, N. and Endo, S. (1970). The generation of ultrahigh hydrostatic pressures by a split sphere apparatus. *Review of Scientific Instruments*, 41, 1178-1181.
- Kelemen, P. B., Shimizu, N., and Salters, V. J. (1995). Extraction of mid-ocean-ridge basalt from the upwelling mantle by focused flow of melt in dunite channels. *Nature*, 375, 747-753.
- Keppler, H., and Frost, D. J. (2005). Introduction to minerals under extreme conditions. In: Miletich, R. (Ed.), *Mineral Behavior at Extreme Conditions*. European Mineralogical Union, 1-30.
- Kittel, C., McEuen, P. and McEuen, P. (1996). *Introduction to solid state physics*. New York: Wiley. 105-130.

- Knoche, R., Dingwell, D. B. and Webb, S. L. (1995). Melt densities for leucogranites and granitic pegmatites: Partial molar volumes for SiO₂, Al₂O₃, Na₂O, K₂O, Li₂O, Rb₂O, Cs₂O, MgO, CaO, SrO, BaO, B₂O₃, P₂O₅, F₂O₋₁, TiO₂, Nb₂O₅, Ta₂O₅, and WO₃. *Geochimica et Cosmochimica Acta*, 59, 4645-4652.
- Kohara, S., Akola, J., Morita, H., Suzuya, K., Weber, J. K. R., Wilding, M. C. and Benmore, C. J. (2011). Relationship between topological order and glass forming ability in densely packed enstatite and forsterite composition glasses. *Proceedings of the National Academy of Sciences*, 108, 14780-14785.
- Kohn, W. and Sham, L. J. (1965). Self-consistent equations including exchange and correlation effects. *Physical Review*, 140, 1133.
- Komabayashi, T., Hirose, K., Sata, N., Ohishi, Y. and Dubrovinsky, L. S. (2007). Phase transition in CaSiO₃ perovskite. *Earth and Planetary Science Letters*, 260, 564-569.
- Komabayashi, T. (2014). Thermodynamics of melting relations in the system Fe-FeO at high pressure: Implications for oxygen in the Earth's core. *Journal of Geophysical Research: Solid Earth*, 119, 4164-4177.
- Kresse, G. and Furthmüller, J. (1996). Efficient iterative schemes for ab initio total-energy calculations using a plane-wave basis set. *Physical Review B*, 54, 11169.
- Kresse, G. and Joubert, D. (1999). From ultrasoft pseudopotentials to the projector augmented-wave method. *Physical Review B*, 59, 1758.
- Kurashina, T., Hirose, K., Ono, S., Sata, N. and Ohishi, Y. (2004). Phase transition in Al-bearing CaSiO₃ perovskite: implications for seismic discontinuities in the lower mantle. *Physics of the Earth and Planetary Interiors*, 145, 67-74.
- Kurnosov, A., Marquardt, H., Frost, D. J., Ballaran, T. B. and Ziberna, L. (2017). Evidence for a Fe³⁺-rich pyrolitic lower mantle from (Al, Fe)-bearing bridgmanite elasticity data. *Nature*, 543, 543-546.

Kuwahara, H., Nomura, R., Nakada, R., and Irifune, T. (2018). Simultaneous determination of melting phase relations of mantle peridotite and mid-ocean ridge basalt at the uppermost lower mantle conditions. *Physics of the Earth and Planetary Interiors*, 284, 36-50.

Labrosse, S., Hernlund, J. W., and Coltice, N. (2007). A crystallizing dense magma ocean at the base of the Earth's mantle. *Nature*, 450, 866-869.

Labrosse, S., Morison, A., Bolrão, D. P., Agrusta, R., Ballmer, M., Rozel, A., Deguen, R., Alboussiere, T., Tackley, P. J. and Dubuffet, F. (2019). Geodynamical and Geochemical Implications of a Long Lasting Basal Magma Ocean. In AGU Fall Meeting Abstracts, MR22A-03.

Lange, R. A. and Carmichael, I. S. (1987). Densities of Na₂O-K₂O-CaO-MgO-FeO-Fe₂O₃-Al₂O₃-TiO₂-SiO₂ liquids: new measurements and derived partial molar properties. *Geochimica et Cosmochimica Acta*, 51, 2931-2946.

Lange, R. A. (1997). A revised model for the density and thermal expansivity of K₂O-Na₂O-CaO-MgO-Al₂O₃-SiO₂ liquids from 700 to 1900 K: extension to crustal magmatic temperatures. *Contributions to Mineralogy and Petrology*, 130, 1-11.

Lee, S. K., Lin, J. F., Cai, Y. Q., Hiraoka, N., Eng, P. J., Okuchi, T., Mao, H. K., Meng, Y., Hu, M. Y., Chow, P. and Shu, J. (2008). X-ray Raman scattering study of MgSiO₃ glass at high pressure: Implication for triclustered MgSiO₃ melt in Earth's mantle. *Proceedings of the National Academy of Sciences*, 105, 7925-7929.

Leinenweber, K. D., Tyburczy, J. A., Sharp, T. G., Soignard, E., Diedrich, T., Petuskey, W. B., Wang, Y. and Mosenfelder, J. L. (2012). Cell assemblies for reproducible multi-anvil experiments. *American Mineralogist*, 97, 353-368.

Le Roux, S. and Jund, P. (2010). Ring statistics analysis of topological networks: New approach and application to amorphous GeS₂ and SiO₂ systems. *Computational Materials Science*, 49, 70-83.

- Leshner, C. E., Wang, Y., Gaudio, S., Clark, A., Nishiyama, N. and Rivers, M. (2009). Volumetric properties of magnesium silicate glasses and supercooled liquid at high pressure by X-ray microtomography. *Physics of the Earth and Planetary Interiors*, 174, 292-301.
- Liebske, C., Corgne, A., Frost, D. J., Rubie, D. C., and Wood, B. J. (2005). Compositional effects on element partitioning between Mg-silicate perovskite and silicate melts. *Contributions to Mineralogy and Petrology*, 149, 113-128.
- Liebske, C., and Frost, D. J. (2012). Melting phase relations in the MgO–MgSiO₃ system between 16 and 26 GPa: Implications for melting in Earth's deep interior. *Earth and Planetary Science Letters*, 345, 159-170.
- Lin, J. F., Vankó, G., Jacobsen, S. D., Iota, V., Struzhkin, V. V., Prakapenka, V. B., Kuznetsov, A. and Yoo, C. S. (2007). Spin transition zone in Earth's lower mantle. *Science*, 317, 1740-1743.
- Lin, J. F., Speziale, S., Mao, Z. and Marquardt, H. (2013). Effects of the electronic spin transitions of iron in lower mantle minerals: Implications for deep mantle geophysics and geochemistry. *Reviews of Geophysics*, 51, 244-275.
- Lin, J. F., Mao, Z., Yang, J., Liu, J., Xiao, Y., Chow, P. and Okuchi, T. (2016). High-spin Fe²⁺ and Fe³⁺ in single-crystal aluminous bridgmanite in the lower mantle. *Geophysical Research Letters*, 43, 6952-6959.
- Lindsley, D. H. (1966), Pressure-temperature relations in the system FeO-SiO₂, *Year Book Carnegie Inst. Washington*, 65, 226–230.
- Lissauer, J. J. (1993). Planet formation. *Annual Review of Astronomy and Astrophysics*, 31, 129-172.
- Lin, J. F., Speziale, S., Mao, Z. and Marquardt, H. (2013). Effects of the electronic spin transitions of iron in lower mantle minerals: Implications for deep mantle geophysics and geochemistry. *Reviews of Geophysics*, 51, 244-275.

Liu, Z., Liu, R., Shang, Y., Shen, F., Chen, L., Hou, X., Yao, M., Cui T., Liu, B., and Katsura, T. (2020). Aluminum solubility in bridgmanite up to 3000 K at the top lower mantle. *Geoscience Frontiers*, 12, 929-935.

Maas, C. and Hansen, U. (2015). Effects of Earth's rotation on the early differentiation of a terrestrial magma ocean. *Journal of Geophysical Research: Solid Earth*, 120, 7508-7525.

Makov, G. and Payne, M. C. (1995). Periodic boundary conditions in ab initio calculations. *Physical Review B*, 51, 4014.

Malfait, W. J., Seifert, R., and Sanchez-Valle, C. (2014). Densified glasses as structural proxies for high-pressure melts: Configurational compressibility of silicate melts retained in quenched and decompressed glasses. *American Mineralogist*, 99, 2142-2145.

Mao, H. K. and Bell, P. M. (1972). Electrical conductivity and the red shift of absorption in olivine and spinel at high pressure. *Science*, 176, 403-406.

Mao, Z., Lin, J. F., Yang, J., Wu, J., Watson, H. C., Xiao, Y., Chow, P. and Zhao, J. (2014). Spin and valence states of iron in Al-bearing silicate glass at high pressures studied by synchrotron Mössbauer and X-ray emission spectroscopy. *American Mineralogist*, 99, 415-423.

Martin-Short, R., Allen, R., Bastow, I. D., Porritt, R. W. and Miller, M. S. (2018). Seismic imaging of the Alaska subduction zone: Implications for slab geometry and volcanism. *Geochemistry, Geophysics, Geosystems*, 19, 4541-4560.

Maruyama, S. and Okamoto, K. (2007). Water transportation from the subducting slab into the mantle transition zone. *Gondwana Research*, 11, 148-165.

Matsukage, K. N., Jing, Z. and Karato, S. I. (2005). Density of hydrous silicate melt at the conditions of Earth's deep upper mantle. *Nature*, 438, 488-491.

Maurice, M., Tosi, N., Samuel, H., Plesa, A. C., Hüttig, C., and Breuer, D. (2017). Onset of solid-state mantle convection and mixing during magma ocean solidification. *Journal of Geophysical Research: Planets*, 122, 577-598.

McCammon, C. (1997). Perovskite as a possible sink for ferric iron in the lower mantle. *Nature*, 387, 694-696.

McGonegle, D., Heighway, P. G., Sliwa, M., Bolme, C. A., Comley, A. J., Dresselhaus-Marais, L. E., Higginbotham, A., Poole, A. J., McBride, E. E., Nagler, B. and Nam, I. (2020). Investigating off-Hugoniot states using multi-layer ring-up targets. *Scientific Reports*, 10, 13172.

McNamara, A. K., Garnero, E. J. and Rost, S. (2010). Tracking deep mantle reservoirs with ultra-low velocity zones. *Earth and Planetary Science Letters*, 299, 1-9.

McNamara, A. K. (2019). A review of large low shear velocity provinces and ultra low velocity zones. *Tectonophysics*, 760, 199-220.

Miyazaki, Y., and Korenaga, J. (2019). On the timescale of magma ocean solidification and its chemical consequences: 1. Thermodynamic database for liquid at high pressures. *Journal of Geophysical Research: Solid Earth*, 124, 3382-3398.

Monteux, J., Andrault, D., and Samuel, H. (2016). On the cooling of a deep terrestrial magma ocean. *Earth and Planetary Science Letters*, 448, 140-149.

Morimoto, N., and Koto, K. (1969). The crystal structure of orthoenstatite. *Zeitschrift für Kristallographie-Crystalline Materials*, 129, 65-83.

Mosenfelder, J. L., Asimow, P. D., Frost, D. J., Rubie, D. C., and Ahrens, T. J. (2009). The MgSiO₃ system at high pressure: Thermodynamic properties of perovskite, postperovskite, and melt from global inversion of shock and static compression data. *Journal of Geophysical Research: Solid Earth*, 114, 01203.

Moynihan, C. T. (1995). Structural relaxation and the glass transition. *Structure, Dynamics, and Properties of Silicate Melts, Reviews in Mineralogy*, 32, 1-20.

Murakami, M., Hirose, K., Kawamura, K., Sata, N. and Ohishi, Y. (2004). Post-perovskite phase transition in MgSiO_3 . *Science*, 304, 855-858.

Nakajima, M. and Stevenson, D. J. (2015). Melting and mixing states of the Earth's mantle after the Moon-forming impact. *Earth and Planetary Science Letters*, 427, 286-295.

Nishihara, Y., Doi, S., Kakizawa, S., Higo, Y., and Tange, Y. (2020). Effect of pressure on temperature measurements using WRe thermocouple and its geophysical impact. *Physics of the Earth and Planetary Interiors*, 298, 106348.

Nomura, R., Ozawa, H., Tateno, S., Hirose, K., Hernlund, J., Muto, S., Ishii, H., and Hiraoka, N. (2011). Spin crossover and iron-rich silicate melt in the Earth's deep mantle. *Nature*, 473, 199-202.

Nomura, R., Hirose, K., Uesugi, K., Ohishi, Y., Tsuchiyama, A., Miyake, A., and Ueno, Y. (2014). Low core-mantle boundary temperature inferred from the solidus of pyrolite. *Science*, 343, 522-525.

Nosé, S. (1984). A unified formulation of the constant temperature molecular dynamics methods. *The Journal of Chemical Physics*, 81, 511-519.

Oka, K., Hirose, K., Tagawa, S., Kidokoro, Y., Nakajima, Y., Kuwayama, Y., Morard, G., Coudurier, N. and Fiquet, G. (2019). Melting in the Fe-FeO system to 204 GPa: Implications for oxygen in Earth's core. *American Mineralogist*, 104, 1603-1607.

Ohta, K., Wakamatsu, T., Kodama, M., Kawamura, K. and Hirai, S. (2020). Laboratory-based x-ray computed tomography for 3D imaging of samples in a diamond anvil cell in situ at high pressures. *Review of Scientific Instruments*, 91, 093703.

- Ohtani, E., Moriwaki, K., Kato, T. and Onuma, K. (1998). Melting and crystal–liquid partitioning in the system $\text{Mg}_2\text{SiO}_4\text{–Fe}_2\text{SiO}_4$ to 25 GPa. *Physics of the Earth and Planetary Interiors*, 107, 75-82.
- Ohtani, E., Litasov, K., Hosoya, T., Kubo, T. and Kondo, T. (2004). Water transport into the deep mantle and formation of a hydrous transition zone. *Physics of the Earth and Planetary Interiors*, 143, 255-269.
- Ohnishi, S., Kuwayama, Y., and Inoue, T. (2017). Melting relations in the MgO–MgSiO_3 system up to 70 GPa. *Physics and Chemistry of Minerals*, 44, 445-453.
- Ozawa, K., Anzai, M., Hirose, K., Sinmyo, R., and Tateno, S. (2018). Experimental Determination of Eutectic Liquid Compositions in the MgO–SiO_2 System to the Lowermost Mantle Pressures. *Geophysical Research Letters*, 45, 9552-9558.
- Palme, H., and O'Neill, H. S. C. (2003). Cosmochemical estimates of mantle composition. *Treatise on Geochemistry*, 2, 1–38.
- Patnaik, P. (2003). *Handbook of inorganic chemicals*. New York: McGraw-Hill, 529, 769-771.
- Perdew, J. P., Ruzsinszky, A., Csonka, G. I., Vydrov, O. A., Scuseria, G. E., Constantin, L. A., Zhou, X. and Burke, K. (2008). Restoring the density-gradient expansion for exchange in solids and surfaces. *Physical Review Letters*, 100, 136406.
- Petitgirard, S., Malfait, W. J., Sinmyo, R., Kuppenko, I., Hennem, L., Harries, D., Dane, T., Burghammer, M. and Rubie, D. C. (2015). Fate of MgSiO_3 melts at core–mantle boundary conditions. *Proceedings of the National Academy of Sciences*, 112, 14186-14190.
- Posner, E. S., Rubie, D. C., Frost, D. J., Vlček, V., and Steinle-Neumann, G. (2017). High P–T experiments and first principles calculations of the diffusion of Si and Cr in liquid iron. *Geochimica et Cosmochimica Acta*, 203, 323-342.

Pozgay, S. H., Wiens, D. A., Conder, J. A., Shiobara, H. and Sugioka, H. (2009). Seismic attenuation tomography of the Mariana subduction system: Implications for thermal structure, volatile distribution, and slow spreading dynamics. *Geochemistry, Geophysics, Geosystems*, 10, Q04X05.

Pradhan, G. K., Fiquet, G., Siebert, J., Auzende, A. L., Morard, G., Antonangeli, D., and Garbarino, G. (2015). Melting of MORB at core–mantle boundary. *Earth and Planetary Science Letters*, 431, 247-255.

Prescher, C., Weigel, C., McCammon, C., Narygina, O., Potapkin, V., Kuppenko, I., Sinmyo, R., Chumakov, A. I. and Dubrovinsky, L. (2014). Iron spin state in silicate glass at high pressure: Implications for melts in the Earth's lower mantle. *Earth and Planetary Science Letters*, 385, 130-136.

Prescher, C., Prakapenka, V. B., Stefanski, J., Jahn, S., Skinner, L. B., and Wang, Y. (2017). Beyond sixfold coordinated Si in SiO₂ glass at ultrahigh pressures. *Proceedings of the National Academy of Sciences*, 114, 10041-10046.

Ramo, D. M. and Stixrude, L. (2014). Spin crossover in Fe₂SiO₄ liquid at high pressure. *Geophysical Research Letters*, 41, 4512-4518.

Ringwood, A. E. and Major, A. (1970). The system Mg₂SiO₄ and Fe₂SiO₄ at high pressures and temperatures. *Physics of the Earth and Planetary Interiors*, 3, 89-108.

Ringwood, A. E. (1991). Phase transformations and their bearing on the constitution and dynamics of the mantle. *Geochimica et Cosmochimica Acta*, 55, 2083-2110.

Rost, S., Garnero, E. J., Williams, Q., and Manga, M. (2005). Seismological constraints on a possible plume root at the core–mantle boundary. *Nature*, 435, 666-669.

Rubie, D. C.; Nimmo, F.; Melosh, H. J. (2007). Formation of Earth's core. In Stevenson D. J., editor, *Evolution of the Earth*, volume 9, Elsevier, Amsterdam, 51–90.

Sakamae, H. (2018). Electron Probe Microanalysis. In *Compendium of Surface and Interface Analysis*. Singapore: Springer. 139-142.

Saikia, A., Frost, D. J. and Rubie, D. C. (2008). Splitting of the 520-kilometer seismic discontinuity and chemical heterogeneity in the mantle. *Science*, 319, 1515-1518.

Sanloup, C., Drewitt, J. W., Konôpková, Z., Dalladay-Simpson, P., Morton, D. M., Rai, N., van Westrenen, W. and Morgenroth, W. (2013). Structural change in molten basalt at deep mantle conditions. *Nature*, 503, 104-107.

Sato, T. and Funamori, N. (2010). High-pressure structural transformation of SiO₂ glass up to 100 GPa. *Physical Review B*, 82, 184102.

Schmandt, B., Jacobsen, S. D., Becker, T. W., Liu, Z., and Dueker, K. G. (2014). Dehydration melting at the top of the lower mantle. *Science*, 344, 1265-1268.

Sears, V. F. (1992). Neutron scattering lengths and cross sections. *Neutron News*, 3, 26-37.

Seagle, C. T., Heinz, D. L., Campbell, A. J., Prakapenka, V. B. and Wanless, S. T. (2008). Melting and thermal expansion in the Fe–FeO system at high pressure. *Earth and Planetary Science Letters*, 265, 655-665.

Shen, G., Lazor, P. and Saxena, S. K. (1993). Melting of wüstite and iron up to pressures of 600 kbar. *Physics and Chemistry of Minerals*, 20, 91-96.

Shen, G., and Lazor, P. (1995). Measurement of melting temperatures of some minerals under lower mantle pressures. *Journal of Geophysical Research: Solid Earth*, 100, 17699-17713.

Simon, J. B., Armitage, P. J., Li, R., and Youdin, A. N. (2016). The mass and size distribution of planetesimals formed by the streaming instability. I. The role of self-gravity. *The Astrophysical Journal*, 822, 55.

Smyth, J. R., and Hazen, R. M. (1973). The crystal structures of forsterite and hortonolite at several temperatures up to 900 °C. *American Mineralogist: Journal of Earth and Planetary Materials*, 58, 588-593.

Solomatova, N. V., Jackson, J. M., Sturhahn, W., Rossman, G. R. and Roskosz, M. (2017). Electronic environments of ferrous iron in rhyolitic and basaltic glasses at high pressure. *Journal of Geophysical Research: Solid Earth*, 122, 6306-6322.

Song, X. and Ahrens, T. J. (1994). Pressure-temperature range of reactions between liquid iron in the outer core and mantle silicates. *Geophysical Research Letters*, 21, 153-156.

Stacey, F. D. and Davis, P. M. (2008). *Physics of the Earth*. Cambridge University Press, New York.

Stebbins, J. F. (2016). Glass structure, melt structure, and dynamics: Some concepts for petrology. *American Mineralogist*, 101, 753-768.

Stixrude, L., and Karki, B. (2005). Structure and freezing of MgSiO₃ liquid in Earth's lower mantle. *Science*, 310, 297-299.

Stixrude, L. and Lithgow-Bertelloni, C. (2005). Thermodynamics of mantle minerals-I. Physical properties. *Geophysical Journal International*, 162, 610-632.

Stixrude, L. and Lithgow-Bertelloni, C. (2011). Thermodynamics of mantle minerals-II. Phase equilibria. *Geophysical Journal International*, 184, 1180-1213.

Sun, S. S. (1982). Chemical composition and origin of the Earth's primitive mantle. *Geochimica et Cosmochimica Acta*, 46, 179-192.

Sun, N., Shi, W., Mao, Z., Zhou, C., and Prakapenka, V. B. (2019). High Pressure-Temperature Study on the Thermal Equations of State of Seifertite and CaCl₂-Type SiO₂. *Journal of Geophysical Research: Solid Earth*, 124, 12620-12630.

Sun, Y., Zhou, H., Yin, K. and Lu, X., (2019). First-principles study of thermodynamics and spin transition in FeSiO₃ liquid at high pressure. *Geophysical Research Letters*, 46, 3706-3716.

Tateno, S., Hirose, K., and Ohishi, Y. (2014). Melting experiments on peridotite to lowermost mantle conditions. *Journal of Geophysical Research: Solid Earth*, 119, 4684-4694.

Tateno, S., Hirose, K., Sakata, S., Yonemitsu, K., Ozawa, H., Hirata, T., Hirao, N., and Ohishi, Y. (2018). Melting phase relations and element partitioning in MORB to lowermost mantle conditions. *Journal of Geophysical Research: Solid Earth*, 123, 5515-5531.

Tange, Y., Takahashi, E., Nishihara, Y., Funakoshi, K. I. and Sata, N. (2009). Phase relations in the system MgO-FeO-SiO₂ to 50 GPa and 2000 °C: An application of experimental techniques using multianvil apparatus with sintered diamond anvils. *Journal of Geophysical Research: Solid Earth*, 114, B02214.

Tauzin, B., Debayle, E., and Wittlinger, G. (2010). Seismic evidence for a global low-velocity layer within the Earth's upper mantle. *Nature Geoscience*, 3, 718-721.

Thorne, M. S., Takeuchi, N., and Shiomi, K. (2019). Melting at the edge of a slab in the deepest mantle. *Geophysical Research Letters*, 46, 8000-8008.

Trønnes, R. G. and Frost, D. J. (2002). Peridotite melting and mineral–melt partitioning of major and minor elements at 22–24.5 GPa. *Earth and Planetary Science Letters*, 197, 117-131.

Tsuchida, Y., and Yagi, T. (1989). A new, post-stishovite high-pressure polymorph of silica. *Nature*, 340, 217-220.

Tsuno, K., Ohtani, E. and Terasaki, H. (2007). Immiscible two-liquid regions in the Fe–O–S system at high pressure: implications for planetary cores. *Physics of the Earth and Planetary Interiors*, 160, 75-85.

Usui, Y., and Tsuchiya, T. (2010). Ab initio two-phase molecular dynamics on the melting curve of SiO₂. *Journal of Earth Science*, 21, 801-810.

Virtanen, P., Gommers, R., Oliphant, T. E., Haberland, M., Reddy, T., Cournapeau, D., Burovski, E., Peterson, P., Weckesser, W., Bright, J. and Van Der Walt, S. J. (2020). SciPy 1.0: fundamental algorithms for scientific computing in Python. *Nature methods*, 17, 261-272.

Westrenen, W. V, and Morgenroth, W. (2013). Structural change in molten basalt at deep mantle conditions. *Nature*, 503, 104-107.

Wilding, M. C., Benmore, C. J., Tangeman, J. A., and Sampath, S. (2004). Evidence of different structures in magnesium silicate liquids: coordination changes in forsterite-to enstatite-composition glasses. *Chemical Geology*, 213, 281-291.

Wilding, M. C., Benmore, C. J., Tangeman, J. A., and Sampath, S. (2004b). Coordination changes in magnesium silicate glasses. *Europhysics Letters*, 67, 212.

Wood, B. J. and Rubie, D. C. (1996). The effect of alumina on phase transformations at the 660-kilometer discontinuity from Fe-Mg partitioning experiments. *Science*, 273, 1522-1524.

Wetherill, G. W. (1990). Formation of the Earth. *Annual Review of Earth and Planetary Sciences*, 18, 205-256.

Wood, B. J., and Halliday, A. N. (2005). Cooling of the Earth and core formation after the giant impact. *Nature*, 437, 1345-1348.

Wood, B. J., Walter, M. J. and Wade, J. (2006). Accretion of the Earth and segregation of its core. *Nature*, 441, 825-833.

Xie, L., Yoneda, A., Yoshino, T., Yamazaki, D., Tsujino, N., Higo, Y., Tange, Y., Irifune, T., Shimei, T. and Ito, E. (2017). Synthesis of boron-doped diamond and its application as a heating material in a multi-anvil high-pressure apparatus. *Review of Scientific Instruments*, 88, 093904.

Xie, L., Yoneda, A., Xu, F., Higo, Y., Wang, C., Tange, Y., King, A., Antonangeli, D., Morard, G. and Guignot, N. (2020). Boron–MgO composite as an X-ray transparent pressure medium in the multi-anvil apparatus. *Review of Scientific Instruments*, 91, 043903.

Yamazaki, D., Ito, E., Yoshino, T., Tsujino, N., Yoneda, A., Guo, X., Xu, F., Higo, Y. and Funakoshi, K. (2014). Over 1 Mbar generation in the Kawai-type multianvil apparatus and its application to compression of $(\text{Mg}_{0.92}\text{Fe}_{0.08})\text{SiO}_3$ perovskite and stishovite. *Physics of the Earth and Planetary Interiors*, 228, 262-267.

Yang, L., Karandikar, A. and Boehler, R. (2012). Flash heating in the diamond cell: Melting curve of rhenium. *Review of Scientific Instruments*, 83, 063905.

Yoshizaki, T., and McDonough, W. F. (2020). The composition of Mars. *Geochimica et Cosmochimica Acta*, 273, 137-162.

Yuan, L., Steinle-Neumann, G. and Suzuki, A. (2020). Structure and density of H_2O -rich Mg_2SiO_4 melts at high pressure from ab initio simulations. *Journal of Geophysical Research: Solid Earth*, 125, 2020JB020365.

Zerr, A., and Boehler, R. (1993). Melting of $(\text{Mg,Fe})\text{SiO}_3$ -perovskite to 625 kilobars: Indication of a high melting temperature in the lower mantle. *Science*, 262, 553-555.

Zheng, T., Zhao, L. and Zhu, R. (2009). New evidence from seismic imaging for subduction during assembly of the North China craton. *Geology*, 37, 395-398.

Acknowledgements

First of all, I would like to thank for the long-term important support from two of my supervisors: Gerd Steinle-Neumann and Dan Frost. Gerd is super helpful in dealing with the foreign students to adapt the life in Bayreuth, his habit of detailed everything as well as step by step logic plays an important role in modelling because it increases model robustness and towards figuring out key points in complex system. Dan is very good at powering students to overcome challenging scientific tasks, his fresh thinking always leads to insights into thermodynamics, he is very clear about research purpose and patient with research work.

Thanks for the endless support from Petra Buchert, she answers all the questions and solves all the requirements from me. Thanks for the help from Janina Potzel, Lydia Kison-Herzig and Nicole Fischer dealing with lots of my documents. Many thanks to Heinz Fischer and Stefan Übelhack for finding me different kinds of small useful tools and for providing very high-quality cubes as well as parts of cells. Thanks to Raphael Njul, Hubert Schulze and Alexander Rother who contributed to very nice sample polishing.

I would like to say thank you to Anna Dinius, very patient and helpful in dealing with lots of my German documents. Thanks to the humorous and friendly Detlef Krauß help a lot to deal with computer hardware, software, carbon coating and EPMA calibration. Thank for the EPMA calibration and fresh vegetables from Anke Potzel. Many thanks for the important contributions from Ulrike Trenz, every chemical and material related questions and requirements is answered and solve perfectly. Many thanks to Dorothea Wiesner, for every theoretical question and practical step about SEM. Thanks for the insightful talk with Sven Linhardt about the press and material properties, and to Gerald Bauer for reminding me about the online poster.

I am very grateful to Fabian Wagle who provided lots of discussions and important experience about simulations. Many thanks for the insightful academic advice from Catherine McCammon. Thanks to Marcel Thielmann, Philipp Eichheimer, Rebecka Matthäus and Stefan Keyssner who helped me to make calls in German. Many thanks to Zhaodong Liu, Luca Ziberna, Hongzhan Fei, Pierre Condamine and Katherine Armstrong who contributed to my work in MA experiment in different aspects. Thanks to Tiziana Boffa Ballaran, Nobuyoshi Miyajima, Giacomo Criniti, Sergey Ovsyannikov, Narangoo Purevjav and

Alexander Kurnsov for sharing ideas about crystal structure. Many thanks for the fruitful talks with Tony Withers, Longjian Xie, Adrien Néri, Slava Shcheka, Lianjie Man, Takayuki Ishii, Esther Posner, Florian Heidelbach, Liang Yuan and so on.

Finally, I thank my parents, friends in China and Australia who always provide me strong and significant support. Many thanks for the long term support from BGI, very happy to meet friends here who come from different parts of the world, and contribute to a fantastic and comfortable environment to perform research and enjoy life.

(Eidesstattliche) Versicherungen und Erklärungen

(§ 9 Satz 2 Nr. 3 PromO BayNAT)

Hiermit versichere ich eidesstattlich, dass ich die Arbeit selbstständig verfasst und keine anderen als die von mir angegebenen Quellen und Hilfsmittel benutzt habe (vgl. Art. 64 Abs. 1 Satz 6 BayHSchG).

(§ 9 Satz 2 Nr. 3 PromO BayNAT)

Hiermit erkläre ich, dass ich die Dissertation nicht bereits zur Erlangung eines akademischen Grades eingereicht habe und dass ich nicht bereits diese oder eine gleichartige Doktorprüfung endgültig nicht bestanden habe.

(§ 9 Satz 2 Nr. 4 PromO BayNAT)

Hiermit erkläre ich, dass ich Hilfe von gewerblichen Promotionsberatern bzw. -vermittlern oder ähnlichen Dienstleistern weder bisher in Anspruch genommen habe noch künftig in Anspruch nehmen werde.

(§ 9 Satz 2 Nr. 7 PromO BayNAT)

Hiermit erkläre ich mein Einverständnis, dass die elektronische Fassung meiner Dissertation unter Wahrung meiner Urheberrechte und des Datenschutzes einer gesonderten Überprüfung unterzogen werden kann.

(§ 9 Satz 2 Nr. 8 PromO BayNAT)

Hiermit erkläre ich mein Einverständnis, dass bei Verdacht wissenschaftlichen Fehlverhaltens Ermittlungen durch universitätsinterne Organe der wissenschaftlichen Selbstkontrolle stattfinden können.

Bayreuth

19/12/2021

.....
Ort, Datum, Unterschrift